Experimentelle Physik

Investigation of the tensor analysing power T_{20} in the $\vec{\mathrm{d}} + \mathrm{p} \rightarrow {}^{3}\mathrm{He} + \eta$ reaction with the COSY-ANKE experiment

Inaugural-Dissertation
zur Erlangung des Doktorgrades
der Naturwissenschaften im Fachbereich Physik
der Mathematisch-Naturwissenschaftlichen Fakultät
der Westfälischen Wilhelms-Universität Münster

vorgelegt von

Michael Paul Papenbrock

aus Thuine

-2016-

Dekan: Prof. Dr. Michael Klasen
Erster Gutachter: Prof. Dr. Alfons Khoukaz
Zweiter Gutachter: Prof. Dr. Johannes Wessels

Tag der mündlichen Prüfung:
Tag der Promotion:

Zusammenfassung

Die hier vorgestellte Arbeit ist ein Beitrag zur anhaltenden Suche nach quasigebundenen Zuständen zwischen Mesonen und Atomkernen. Frühe theoretische Vorhersagen legten nahe, dass sich solche Zustände, zum Beispiel zwischen einem η Meson und einem Kern mit Massenzahl $A \geq 12$, formen könnten. Diverse Messungen in diesem Feld haben Hinweise hervorgebracht, dass ein solcher Zustand womöglich tatächlich existiert. Interessanterweise wurden solche Hinweise auch für sehr viel kleinere Massenzahlen gefunden, zum Beispiel zwischen einem η Meson und einem $^3\mathrm{He}$ Kern. Von besonderem Interesse ist hier eine unpolarisierte Messung der $\mathrm{d} + \mathrm{p} \to {}^3\mathrm{He} + \eta$ Reaktion, welche mit einem immens hohem Detailgrad im Überschussenergiebereich $-5\,\mathrm{MeV} < Q < 11\,\mathrm{MeV}$ mit dem COSY-ANKE Experiment untersucht wurde. Hinweise für einen quasigebundenen $\eta\,^3\mathrm{He}$ Zustand wurden gefunden indem die totalen und differntiellen Wirkungsquerschnitte in Abhängigkeit von der Energie parametrisiert wurden. Dies erlaubte die Extraktion der Endzustandswechselwirkung zwischen den Ejektilen, welche sich als überraschend stark erwies. Jedoch war es nicht möglich mit unpolarsiertem Strahl und Target mögliche Beiträge des Anfangszustands zum Wirkungsquerschnitt zu untersuchen.

Der Endzustand in der $\mathrm{d} + \mathrm{p} \to {}^3\mathrm{He} + \eta$ Reaktion kann zwei unterschiedlichen Spin-Anfangszuständen mit $S = 1/2$ und $S = 3/2$ erzeugt werden. Sofern die Produktionsamplituden dieser beiden Zustände unterschiedlich ist, könnte sich dieser Umstand bei einer unpolarisierten Messung in der Form des totalen Wirkungsquerschnitt manifestieren, was wiederum Einfluss auf die Bestimmung der Endzustandswechselwirkung hätte. Eine neue Messung mit einem vektor- und tensorpolarisierten Deuteronstrahl der *dpolpheeta* Reaktion wurde mit COSY-ANKE in dem gleichen Überschussenergiebereich, $-5\,\mathrm{MeV} < Q < 11\,\mathrm{MeV}$, durchgeführt mit dem Ziel die Energieabhängigkeit der Tensoranalysierstärke T_{20} zu extrahieren. Die ermittelten Werde für T_{20} sind kompatibel mit einer Konstanten in diesem Energiebereich. Ein linearer Fit an diese Daten zeigte nur eine sehr kleine mögliche Energieabhängigkeit. Daher ist der mögliche Einfluss der Spin-Anfangszustände auf die Extraktion der Endzustandswechselwirkung von sehr geringer Signifikanz.

Die Ergebnisse dieser Arbeit lassen sich mit denen der unpolarisierten Messung kombinieren um so die quadrierten s-Wellenamplituden $|A|^2$ und $|B|^2$ zu bestimmen, welche beide in die quadrierte Produktionsamplitude der untersuchten Reaktion eingehen. Durch Bestimmung der Abhängkeit von T_{20} vom Kosinus des Polarwinkels $\cos\theta$ hat sich jedoch ergeben, dass die existierenden Modelle für $|A|^2$ und $|B|^2$ nicht gleichzeitig die polarisierten und unpolarisierten Daten beschreiben können und diese Modelle daher überarbeitet werden müssen.

Abstract

The work presented here is a contribution to the ongoing search for quasi-bound states between mesons and nuclei. Early theoretical predictions estimated that an η-meson may form a quasi-bound state with nuclei with a mass number of $A \geq 12$. Many measurements in this field have revealed evidence that such a state may indeed exist. More interestingly, it may already form at much lower mass numbers, *e.g.* between an η-meson and ^{3}He nucleus. Of special note is an unpolarised measurement of the $\mathrm{d} + \mathrm{p} \rightarrow {}^3\mathrm{He} + \eta$ reaction, which has been studied in unprecedented detail in the excess energy range $-5\,\mathrm{MeV} < Q < 11\,\mathrm{MeV}$ with the COSY-ANKE experiment. Evidence for a quasi-bound $\eta\,^3$He state was found by parametrising total and differential cross sections and extracting the final state interaction between the two ejectiles, which was found to be surprisingly strong. However, with both beam and target being unpolarised, possible contributions of the initial state to the cross section could not be investigated.

In the $\mathrm{d} + \mathrm{p} \rightarrow {}^3\mathrm{He} + \eta$ reaction the final state can be produced from two different initial spin states with $S = 1/2$ and $S = 3/2$. If the production amplitudes of these respective states inhibit a different energy dependence, it could manifest in the shape of the total cross section in an unpolarised measurement, thereby affecting the determination of the final state interaction. A new measurement with a vector and tensor polarised deuteron beam on the $\vec{\mathrm{d}} + \mathrm{p} \rightarrow {}^3\mathrm{He} + \eta$ reaction was performed with COSY-ANKE in the same excess energy range, *i.e.* $-5\,\mathrm{MeV} < Q < 11\,\mathrm{MeV}$, with the aim to extract the energy dependence of the tensor analysing power T_{20}. The extracted values of T_{20} are compatible with a constant across this energy range. A linear fit revealed only a rather small possible energy dependence. Hence, the possible impact of the initial spin states on the extraction of the final state interaction was found to be of very little significance.

Combining the results of this measurement with those of the unpolarised one allowed to extract values for the squared s-wave amplitudes $|A|^2$ and $|B|^2$, which both factor into the squared production amplitude of the investigated reaction. However, through extracting the dependence of T_{20} on the cosine of the polar angle $\cos\theta$ it was found that the existing models for $|A|^2$ and $|B|^2$ fail to describe both the unpolarised and polarised data at the same time and therefore will have to be revised.

Contents

Chapter 1

Introduction

One of the most challenging problems in contemporary physics is the understanding of the strong force that holds the elementary particles together. The strong force generates 98% of the visible mass in the universe. With the rise of particle accelerators in the twentieth century and their increasing energies, it has become possible to probe the strong interaction in ever increasing detail.

The theory of Quantum ChromoDynamics (QCD) [1, 2, 3, 4] is a relativistic quantum field theory of coloured quarks and gluons, interacting with non-abelian forces. The strong coupling constant α_s is small at short distances, short enough for perturbation theory to be applied. Perturbative QCD (pQCD) predictions have been rigorously and successfully tested [5]. At larger distances, α_s becomes too large for perturbative calculations. When the distance increases between two coloured objects, *e.g.* a quark q and an anti-quark $\bar{q}$, it will eventually cost more energy to pull them further apart than to create a new $q\bar{q}$ pair. This leads to the quark confinement, which explains qualitatively why no free quarks have been observed, but only composite, colourless hadrons: baryons (qqq) and mesons ($q\bar{q}$).

The strong interaction can be probed at several energy ranges or scales. By studying systems of light quarks, the long-range interaction is probed. The interactions are highly relativistic and non-perturbative. The processes can be described by effective field theories, *e.g.* Chiral Perturbation Theory (ChPT), where the relevant degrees of freedom are mesons and baryons. The scale of light meson production is in the order of a few hundred MeV/c^2, which is close to the QCD cut-off $\Lambda_{\mathrm{QCD}} \approx 200\,\mathrm{MeV}/c^2$ [6]. In this intermediate domain the relevant degrees of freedom, *i.e.* quarks and gluons, or hadrons, are unclear. Neither pQCD nor ChPT works well and instead, phenomenological models are used to describe the processes. However, these models need guidance from experiments. In terms of the meson-nucleon interaction, it was found that there could be an attractive potential between a nucleon and the η meson [7], possibly leading to a quasi-bound η-nucleus state [8]. The most striking evidence supporting this hypothesis was found in a measurement of the cross sections of the $\mathrm{d} + \mathrm{p} \to {}^3\mathrm{He} + \eta$ reaction close to the production threshold [9].

In this work, a new measurement on the $\vec{\mathrm{d}} + \mathrm{p} \to {}^3\mathrm{He} + \eta$ reaction was performed with a vector and tensor polarised deuteron beam. The s-wave $\eta\,{}^3\mathrm{He}$ system can be accessed via the spin of the initial deuteron-proton system which can be either $S = \frac{1}{2}$ or $S = \frac{3}{2}$. The conclusions drawn from the unpolarised data were based on a strong $\eta\,{}^3\mathrm{He}$ final state interaction derived from a fit to the total cross section data close to the production threshold. However, a possible dependence on the total spin of the initial state may contribute to the shape of the $\eta\,^3$He cross section. Therefore, by searching for such a dependence the final state interaction hypothesis can be verified, and the new data might help in the development of phenomenological models for the production and/or interaction in the $\mathrm{d} + \mathrm{p} \to {}^3\mathrm{He} + \eta$ reaction.

1.1 Hadrons

Hadrons are composite, colourless particles that are subject to the strong interaction. According to the standard model [10], they are comprised of quarks and gluons and can be grouped into categories based on the quark content: Three-quark systems (qqq) called baryons and quark-antiquark systems ($q\bar{q}$) called mesons. More complex systems are allowed by QCD and several heavier mesons are currently being investigated as possible tetraquark states [11]. Moreover, the possibility of the existence of pentaquarks is currently being revisited [12]. Also in recent years, a resonance-like structure was observed double-pionic fusion reactions that could be associated with a dibaryon [13] or even a hexaquark [14].

Table 1.1: The six quarks in the standard model. Also shown is the isospin I, its third component I_3, the electrical charge as a multiple of the elementary charge, and the mass [5].

quark	**isospin** I	I_3	**charge** $[e]$	**mass** [**MeV**$/c^2$]
up (u)	1/2	1/2	2/3	$2.3^{+0.7}_{-0.5}$
down (d)	1/2	-1/2	-1/3	$4.8^{+0.5}_{-0.3}$
strange (s)	0	0	-1/3	95 ± 5
charm (c)	0	0	2/3	1275 ± 25
bottom (b)	0	0	-1/3	$(4.18 \pm 0.03) \cdot 10^3$
top (t)	0	0	2/3	$(173.21 \pm 0.51 \pm 0.71) \cdot 10^3$

There are three families of quarks in the standard model containing two quarks each and they are listed in table 1.1. The two lightest quarks, up and down, constitute the matter we know: protons (uud) and neutrons (udd). The neutron is unstable and decays into the proton via $\mathrm{n} \to \mathrm{p} + e^- + \bar{\nu}_e$, where $\bar{\nu}_e$ is the electron anti-neutrino. However, protons and neutrons together can form stable composite particles, *i.e.* the nuclei. These have been a field of extensive research and today many isotopes are known. It is also possible to create baryons containing heavier quarks, so-called hyperons. All hyperons are unstable and the ground state hyperons decay through the weak interaction.

The other family of hadrons, the mesons, can be grouped based on their spin. Since these are $q\bar{q}$ systems, the spin of the meson has to be integer. They can be separated even further based on their orbital angular momentum l, which defines their parity:

$$P = (-1)^{l+1}. \tag{1.1.1}$$

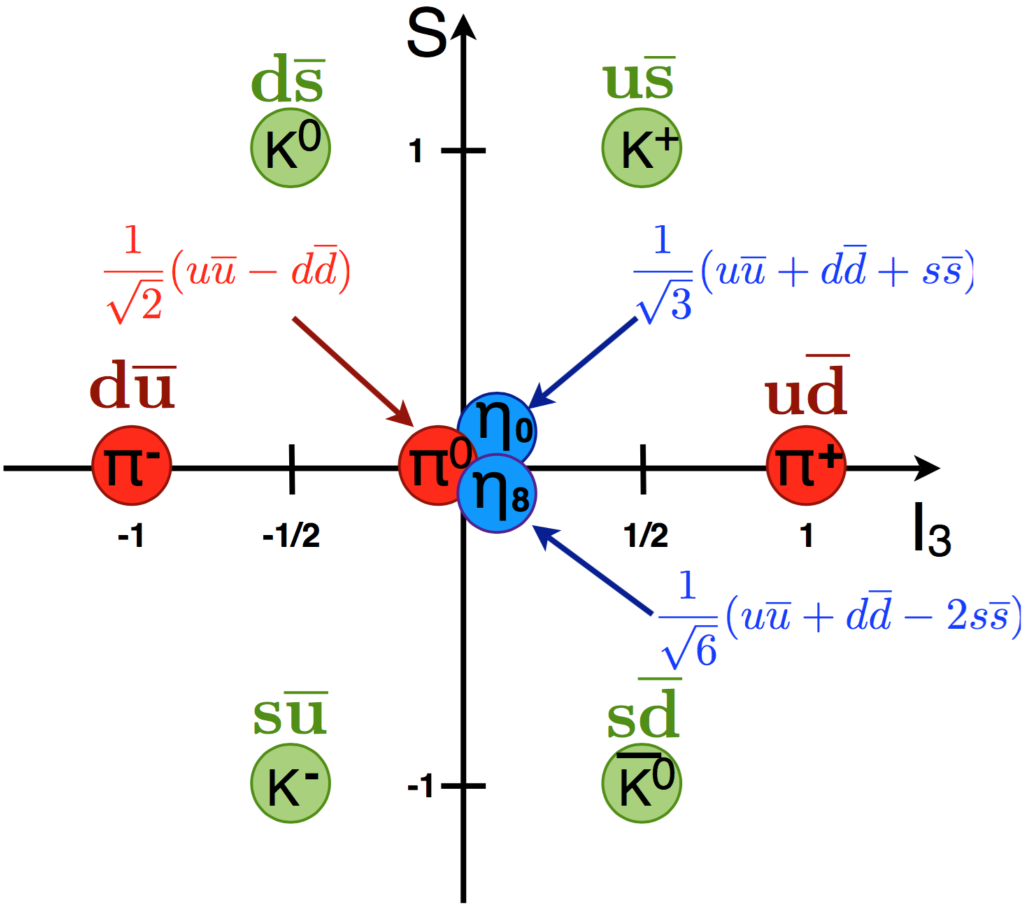

Figure 1.1: The nonet of pseudo-scalar mesons. Here, the strangeness S is plotted against the third component of the isospin I_3. The picture shows the names of the mesons as well as their respective quark content.

Mesons with $S = 0$ and $l = 0$ must have negative parity and are called pseudo-scalar. Their total angular momentum becomes zero:

$$J = |\vec{S} + \vec{L}| = 0. \tag{1.1.2}$$

Focusing only on the three lightest quarks u, d, and s as well their corresponding anti-quarks, nine different combinations are expected. These are shown in fig. 1.1. The low-mass pions π^-, π^0, and π^+ contain only u and d quarks. Mesons with strangeness $S = \pm 1$ are called kaons. The remaining states are the η_0 and η_8. The former was chosen as a symmetric singlet state with isospin $I = 0$. Orthogonal to the η_0 state, the η_8 also has isospin $I = 0$, but belongs to the antisymmetric octet. No measured particles could be directly associated with these states. Instead, the physical particles η and η' are interpreted as mixed states of the η_0 and η_8.

1.2 The η meson

In terms of its interaction with nucleons or nuclei, the η meson is appealing. Due to its charge neutrality, the Coulomb force does not contribute and it therefore serves as a clean probe for the strong interaction. In theory, studying the interaction through ηN scattering would be appealing. However, with a mass of $547.862 \pm 0.018\,\mathrm{MeV}/c^2$ [5] the η meson's decays include both electromagnetic and hadronic final states and it has a short lifetime of $\tau_\eta \approx 5 \cdot 10^{-19}\,\mathrm{s}$, making η beams or targets experimentally unfeasible. Instead, the ηN interaction is studied in γN, πN, and NN reactions with ηN or ηNN final states. In this work, the $\vec{\mathrm{d}} + \mathrm{p} \to {}^3\mathrm{He} + \eta$ reaction is studied with COSY-ANKE. The particular appeal of studying the interaction with the ^{3}He nucleus will be explained in more detail in chapter 2. The most dominant decay modes of the η are given in table 1.2. All of these final states contain one or more photons[1] which the COSY-ANKE experiment is not sensitive to. Therefore, in the $\mathrm{d} + \mathrm{p} \to {}^3\mathrm{He} + \eta$ reaction the η meson has to be reconstructed from missing kinematics by measurement of the ^{3}He nucleus.

Table 1.2: The most dominant decay modes of the η meson [5].

decay mode	**branching ratio**
$\eta \to 2\gamma$	$(39.41 \pm 0.20)\%$
$\eta \to 3\pi^0$	$(32.68 \pm 0.23)\%$
$\eta \to \pi^+\pi^-\pi^0$	$(22.92 \pm 0.28)\%$
$\eta \to \pi^+\pi^-\gamma$	$(4.22 \pm 0.08)\%$

While s-wave interaction between pions and nucleons is weak and probably repulsive, the η-nucleon interaction was found to be attractive at small momenta and very strong [7], introducing the possible existence of a new category of nuclei: the η-mesic nuclei [8].

---

[1] Note that the π^0 decays via $\pi^0 \to 2\gamma$ with a branching ratio of $\approx 99\%$.

Chapter 2

The search for η-mesic nuclei

Three decades ago, the development of new experimental facilities capable of producing significant amounts of η mesons led to theoretical investigations on the possibility of the formation of an η-mesic nucleus. Earlier, Bhalerao and Liu [7] had pointed out that the η-nucleon interaction, contrary to the small, repulsive potential of pionic atoms, is attractive and strong at small momenta. By assuming an attractive ηN interaction, which was determined from an isobar model[1] analysis of the cross sections of the $\pi N \to \eta N$ reaction, Haider and Liu found that nuclei with a mass number of $A \geq 12$ could form a bound state with an η meson [8].

2.1 What is a bound state?

The force between nucleons has been well studied over the years. Nuclear binding between two nucleons occurs when there is an attractive potential affecting them, *e.g.*

$$\begin{aligned} V(r) = &\ -V_0 \qquad \text{for} \quad r < R \\ V(r) = &\ \ \ \ 0 \qquad \text{for} \quad r > R \end{aligned} \tag{2.1.1}$$

with r being the distance between the nucleons and R the radius of the composite system [15]. If the NN system is in its lowest energy state, it has an orbital angular momentum $l = 0$. Defining the radial part of the wave function $\psi(\vec{r})$ as $u(r)/r$, the system can be described by the radial Schrödinger equation,

$$-\frac{\hbar^2}{2m}\frac{\mathrm{d}^2 u}{\mathrm{d}r^2} + V(r)u(r) = Eu(r), \tag{2.1.2}$$

where m is the mass of the system and E the energy. A state is considered to be bound, if the mass of the composite system is lower than the sum of the masses of its constituents. The difference between these masses is the binding energy. For a system to be bound, first the energy must be $E < 0$ [15]. Bound states are then found as the solutions of eq. (2.1.2). These are

$$u(r) = A \sin k_1 r + B \cos k_1 r \tag{2.1.3}$$

---

[1] In the isobar model reactions proceed via the formation of N^* or Δ resonances, *i.e.* isobars [7].

with $k_1 = \sqrt{2m(E+V_0)/\hbar^2}$ for $r < R$, and

$$u(r) = Ce^{-k_2 r} + De^{+k_2 r} \tag{2.1.4}$$

with $k_2 = \sqrt{-2mE/\hbar^2}$ for $r > R$ [15]. In terms of the nucleon-nucleon interaction, many bound states are known, *i.e.* the nuclei. However, these systems do not provide information about the interactions of nucleons with more exotic particles, *e.g.* mesons. Such systems decay rather quickly and are difficult to study. A suitable approach to learn about these systems can be found in scattering experiments. These are usually characterised by their differential cross section, *i.e.* the probability $\mathrm{d}\sigma$ that an incident particle is scattered into the solid angle $\mathrm{d}\Omega$ [15]:

$$\frac{\mathrm{d}\sigma}{\mathrm{d}\Omega} = \frac{\sin^2\delta_0}{k^2}. \tag{2.1.5}$$

Here, δ_0 is the phase shift of the wave function for $l = 0$. Integrating over the full range of solid angles, the total cross section becomes:

$$\sigma = \int \frac{\mathrm{d}\sigma}{\mathrm{d}\Omega}\mathrm{d}\Omega = 4\pi\frac{\mathrm{d}\sigma}{\mathrm{d}\Omega} = \frac{4\pi\sin^2\delta_0}{k^2}. \tag{2.1.6}$$

Representing the strength of the scattering, the scattering length a is introduced as the low-energy limit of the total cross section:

$$\lim_{k\to 0}\sigma = 4\pi a^2. \tag{2.1.7}$$

This leads to

$$a = \pm\lim_{k\to 0}\frac{\sin\delta_0}{k}. \tag{2.1.8}$$

From eqs. (2.1.7) and (2.1.8) it is clear that the sign of the scattering length cannot be determined from measurement of the energy dependence of the cross section. Although arbitrary, it is convention to choose the negative sign. This approximation requires the low-energy range of eV or keV. Larger energies of several MeV are treated in the effective range approximation with the effective range r_0,

$$k\cot\delta_0 = \frac{1}{a} + \frac{1}{2}r_0 k^2 + \ldots, \tag{2.1.9}$$

where terms with higher powers of k have been neglected [15].
The considerations above have to be refined when regarding elastic scattering in the presence of absorptive effects, *e.g.* fusion of the scattering partners. A simple model to account for this is the so-called optical model in which the scattering is represented in terms of a complex potential [15]:

$$U(r) = V(r) + iW(r) \tag{2.1.10}$$

Here, the real part $V(r)$ is responsible for elastic scattering whereas the imaginary part $W(r)$ describes the absorption. Similar to section 2.1, the potential can be described in square-well form, *i.e.*

$$\begin{aligned} U(r) = &\quad -V_0 - iW_0 && \text{for} \quad r < R \\ U(r) = &\quad 0 && \text{for} \quad r > R. \end{aligned} \tag{2.1.11}$$

Solving the Schrödinger equation again, taking the form of e^{ikr}/r for the outgoing scattered wave with $k = \sqrt{2m(E + V_0 + iW_0)/\hbar^2}$, it follows that the wavenumber k is complex. Assuming that the absorption is relatively small, *i.e.* W_0 is small compared to $E + V_0$, k can be expanded using the binomial theorem:

$$k \cong \sqrt{\frac{2m(E+V_0)}{\hbar^2}} + \frac{iW_0}{2}\sqrt{\frac{2m}{\hbar^2}\frac{1}{E+V_0}}. \tag{2.1.12}$$

Since the wavenumber k is complex, the same must be true for the scattering length a and the effective range r_0 (see eq. (2.1.9)) [15].

To have binding, there has to be a real attractive potential, which leads to:

$$\Re(a) < 0. \tag{2.1.13}$$

Regarding the meson-nucleon interaction, in $\eta\,N$ systems, the reaction channel

$$\eta N \to \pi N \tag{2.1.14}$$

is always possible due to the lower mass of the final state. As a consequence, the corresponding scattering length $a_{\eta^3\mathrm{He}}$ for an $\eta\,^3$He system has to be complex.

The cross section in scattering experiments is usually described in terms of the measured centre of mass momenta in the initial state p_i and final state p_f rather than the wavenumber k. Henceforth, using the relation $p = \hbar k$ and the convention $\hbar = c = 1$, the momentum p shall be used instead.

Bound states are solutions of the eq. (2.1.2), which lie on the imaginary axis of the momentum plane with $\Im(p) > 0$ and $\Re(p) = 0$ [16]. If the state is unstable and an interaction as in eq. (2.1.14) is possible, the $\Re(p)$ becomes negative and the state is considered quasi-bound. Unphysical solutions have $\Im(p) < 0$ and the states are denoted as virtual and quasi-virtual, depending on $\Re(p)$ [16]. These definitions are compiled in table 2.1.

Table 2.1: Requirements for bound or virtual states in terms of their solutions on the complex momentum plane.

state	$\Re(p)$	$\Im(p)$
bound	$= 0$	> 0
quasi-bound	< 0	> 0
virtual	$= 0$	< 0
quasi-virtual	< 0	< 0

Bhalerao and Liu showed that the ηN interaction is strong at low momenta and attractive [7]. This led to calculations using an optical potential done by Haider and Liu on possible, quasi-bound states between an η-meson and a nucleus, concluding that these would be possible for mass numbers of $A \geq 12$ [8]. Over the years, many values for the ηN s-wave scattering lengths have been presented, derived from different models or experimental data. While the range of possible values for the imaginary part is rather narrow, the real part is more ambiguous [17, 16]. The calculations by Haider and Liu that led to the prediction of possible η-mesic nuclei with a ^{12}C or heavier were based on a relatively small real part of the $\eta\,N$ scattering length.

2.2 The $\eta\,^3$He system

Contrary to the predictions from Haider and Liu [8], evidence for a bound state between the η meson and a nucleus has been found already for much lower mass numbers. In recent years, a wealth of experimental data has been presented for multiple reaction channels producing an $\eta\,^3$He system and has led to further theoretical considerations. In particular, the final state interaction between the η meson and the ^{3}He nucleus was of high interest.

2.2.1 Production experiments in hadronic scattering

The differential cross section of the $\mathrm{d} + \mathrm{p} \rightarrow {}^3\mathrm{He} + \eta$ reaction is characterised by the two centre of mass momenta in the initial state p_i and final state p_f. Figure 2.1 shows a sketch illustrating these kinematic observables. Taking the differential cross section in its simplest form,

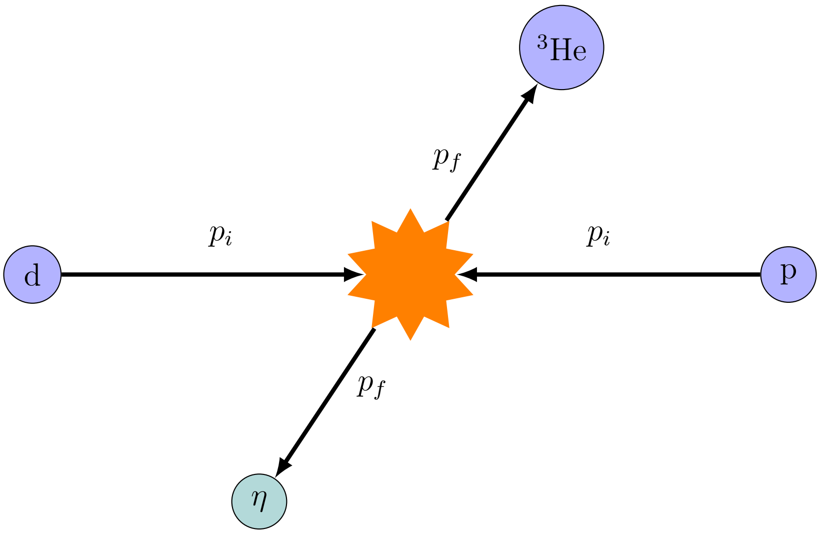

Figure 2.1: Sketch of the $\mathrm{d} + \mathrm{p} \rightarrow {}^3\mathrm{He} + \eta$ reaction in the centre of mass frame. The projectiles have the initial state momentum p_i, the ejectiles the final state momentum p_f.

$$\frac{p_i}{p_f}\frac{\mathrm{d}\sigma}{\mathrm{d}\Omega} = |f|^2, \tag{2.2.1}$$

an interaction between the final state particles can be introduced as part of the squared scattering amplitude $|f|^2$, which is then separated into a nearly constant production amplitude f_B and a final state interaction term FSI:

$$|f_s|^2 = |f_B \cdot FSI|^2 = |f_B|^2 \cdot |FSI|^2. \tag{2.2.2}$$

In accordance with the effective range theory [18], a common ansatz describes the final state interaction in terms of the scattering length a and the effective range r_0:

$$FSI(p_f) = \frac{1}{1 + iap_\eta + \frac{1}{2}ar_0p_\eta^2}. \tag{2.2.3}$$

An alternative form can be derived by substituting the scattering length and effective range with

$$\begin{aligned} a &= -i\frac{p_1 + p_2}{p_1 \cdot p_2}, \\ r_0 &= \frac{2i}{p_1 + p_2}, \end{aligned} \tag{2.2.4}$$

yielding two poles for the scattering amplitude in the η momentum plane:

$$f_s = \frac{f_B}{\left(1 - \frac{p_\eta}{p_1}\right) \cdot \left(1 - \frac{p_\eta}{p_2}\right)} . \tag{2.2.5}$$

The experiment providing the most details on the $\mathrm{d} + \mathrm{p} \to {}^3\mathrm{He} + \eta$ reaction in the excess energy region very close to the $\eta{}^3\mathrm{He}$ production threshold was performed with COSY-ANKE [9]. A rapid rise was observed in the total cross section within the first 1 MeV of the excess energy Q up to its plateau. Earlier measurements on both the $\mathrm{d} + \mathrm{p} \to {}^3\mathrm{He} + \eta$ or $\mathrm{p} + \mathrm{d} \to {}^3\mathrm{He} + \eta$ reactions [19, 20] had already indicated a similar behaviour. By describing the total cross section with eq. (2.2.5), it was found that

$$\begin{aligned} f_B &= (50 \pm 8)\,(\mathrm{nb/sr})^{1/2}\,, \\ p_1 &= \left[(-5 \pm 7^{+2}_{-1}) \pm i(19 \pm 2 \pm 1)\right]\ \mathrm{MeV}/c\,, \\ p_2 &= \left[(106 \pm 5) \pm i(76 \pm 13^{+1}_{-2})\right]\ \mathrm{MeV}/c\,, \end{aligned} \tag{2.2.6}$$

with the first uncertainty being statistical and the second systematic where given. Figure 2.2

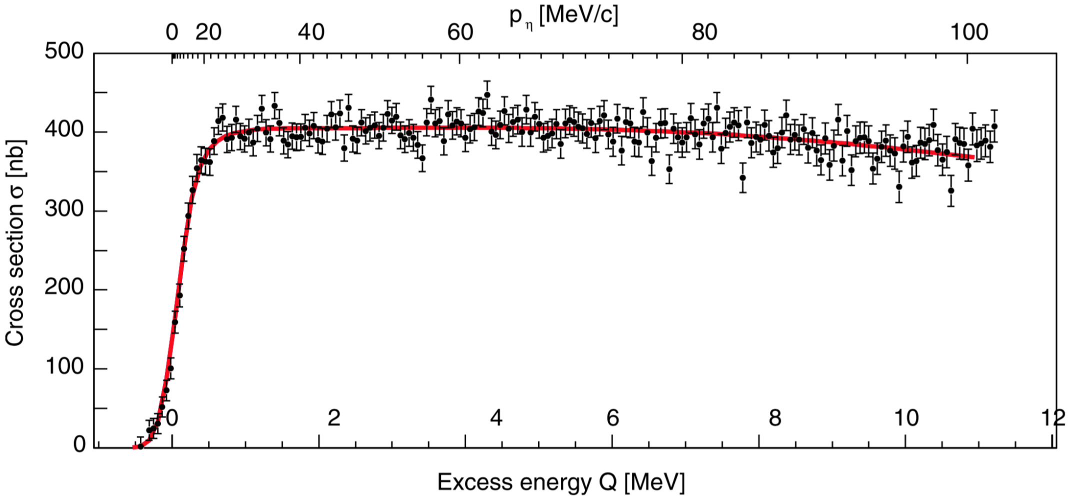

Figure 2.2: Total cross section of the $\mathrm{d} + \mathrm{p} \to {}^3\mathrm{He} + \eta$ reaction measured by the COSY-ANKE experiment. The data are plotted against the excess energy / final state momentum. The fit to the data (red line) includes parameters for beam smearing and the final state interaction. Results are given in the text. Picture taken from [21].

shows the total cross section data of the COSY-ANKE measurement together with the aforementioned parametrisation. The findings were consistent with a measurement performed with COSY-11 that was published earlier [22]. However, the COSY-11 experiment did not, in contrast to COSY-ANKE, correct the scattering length and the effective range for the beam momentum smearing. This led to significantly different values. The first pole p_1 in the COSY-ANKE results might indeed be consistent with a quasi-bound state. The second pole p_2 on the other hand was introduced to describe residual energy dependence possibly arising from the final state interaction as well as the reaction mechanism itself [23]. In section 2.1 it was shown that the sign of the real part of the scattering length a, which separates bound and virtual states, cannot be extracted from a measurement of the cross section. By extension, this is true as well for the sign of the imaginary part of the momentum poles.

The ansatz in eq. (2.2.5) is only valid if the $\eta\,^3$He system is in relative s-wave. As a matter of fact, a $\cos\theta$ asymmetry of the differential cross section is rising with the excess energy Q already for $Q \approx 4\,\mathrm{MeV}$. Here, θ is the polar angle of the η in the centre of mass system. This behaviour points at contributions to the cross section arising from the p-wave already at low energies. Therefore, the ansatz describing the data was later revised [23] to take these effects into account.

As mentioned above, very close to the production threshold the $\eta\,^3$He system is expected to be in its ground state with $L = 0$ where only the s-wave is relevant. The η has spin $S = 0$ and negative parity $P = -1$, whereas the ^{3}He has spin $S = \frac{1}{2}$ but positive parity $P = +1$. Using $P = (-1)^{l+1}$, where l is the orbital momentum of the η relative to the ^{3}He, this leads to ground state of the $\eta\,^3$He system with total orbital momentum $J^P = (L + S)^P = \frac{1}{2}^-$. However, there are multiple spin configurations of the initial state which can lead to this final state. These are compiled in table 2.2 up to $L_{\mathrm{dp}} = 4$. The spin $S = 1$ of the beam deuteron and the spin $S = \frac{1}{2}$ of the target proton can combine to two different spin configurations of the dp system with $S = \frac{1}{2}, \frac{3}{2}$. A negative parity is given for odd orbital momentum numbers, but a final configuration with $J = \frac{1}{2}$ can only be achieved with $L_{\mathrm{dp}} = 1$. These spin and orbital momentum numbers can couple to the total angular momentum via $J = L + S$ and $J = |L - S|$ to different states with $J = \frac{1}{2}, \frac{3}{2}, \frac{5}{2}$. For higher orbital momenta in the initial state there is there is no combination matching the final state. However, it is also possible to produce the $\eta\,^3$He system with a higher total orbital momentum, *e.g.* in relative p-wave with $J = \frac{1}{2}^+, \frac{3}{2}^+$. Due to parity conservation, the orbital momentum of the initial state then has to be even, leaving only $L_{\mathrm{dp}} = 0, 2$ with spin combinations matching the final state.

Equation (2.2.5) implicitly takes two independent s-wave amplitudes, A and B, into account [24, 25]. There are five p-wave amplitudes[2] [23], but for a phenomenological description of the data only the two with a pure $\cos\theta$ dependence in the differential cross section, C and D, are retained [23]. The production operator then takes the following form:

$$\hat{f} = A\vec{\epsilon}\cdot\hat{p}_p + iB(\vec{\epsilon}\times\vec{\sigma})\cdot\hat{p}_p + C\vec{\epsilon}\cdot\vec{p_\eta} + iD(\vec{\epsilon}\times\vec{\sigma})\cdot\vec{p_\eta}, \tag{2.2.7}$$

with $\vec{\epsilon}$ being the polarisation vector of the deuteron, $\hat{p}_p$ the direction of the incident proton beam in the centre of mass frame, $\vec{p_\eta}$ the final state η momentum in the centre of mass frame, and $\vec{\sigma}$ the Pauli matrices. Note that the amplitudes here are not related to the ones found in the solutions of the Schrödinger equation in eqs. (2.1.3) and (2.1.4). For the scattering amplitude, this operator has to be put between the spinors of the ^{3}He

---

[2] A partial wave decomposition for a similar process, *i.e.* pion photoproduction on nucleons, can be found for example in Ref. [26].

Table 2.2: Possible numbers of the total orbital momentum J obtained by different combinations of the spin S_{dp} and the orbital momentum L_{dp} of the deuteron and proton.

$S_{\mathbf{dp}}$	$L_{\mathbf{dp}}$	J
1/2	0	1/2, 1/2
3/2	0	3/2, 3/2
1/2	1	1/2, 3/2
3/2	1	1/2, 5/2
1/2	2	3/2, 5/2
3/2	2	1/2, 7/2
1/2	3	5/2, 7/2
3/2	3	3/2, 9/2
1/2	4	7/2, 9/2
3/2	4	5/2, 11/2

and the proton:

$$f = \bar{u}_{^3\mathrm{He}} \hat{f} u_p. \tag{2.2.8}$$

The unpolarised cross section can then be expressed by the spin-averaged, squared scattering amplitude with

$$\frac{\mathrm{d}\sigma}{\mathrm{d}\Omega} = \frac{p_\eta}{p_p}\overline{|f|^2} = \frac{p_\eta}{3p_p} I. \tag{2.2.9}$$

Including the amplitudes in the production operator in eq. (2.2.7), I can be written as

$$I = |A|^2 + 2|B|^2 + p_\eta^2|C|^2 + 2p_\eta^2|D|^2 + 2p_\eta \Re(A^* C + 2B^* D)\cos\theta_\eta. \tag{2.2.10}$$

This introduces the linear $\cos\theta_\eta$ dependence going with p_η in the $s-p$-wave interference term in order to describe this feature of the data. Describing the asymmetry by a parameter defined as

$$\alpha = \frac{\mathrm{d}}{\mathrm{d}(\cos\theta_\eta)} \ln\left(\frac{\mathrm{d}\sigma}{\mathrm{d}\Omega}\right)\Bigg|_{\cos\theta_\eta=0}, \tag{2.2.11}$$

which leads to

$$\alpha = 2p_\eta \frac{\Re(A^*C + 2B^*D)}{|A|^2 + 2|B|^2 + p_\eta^2|C|^2 + 2p_\eta^2|D|^2}, \tag{2.2.12}$$

Wilkin *et al* extended the description of the cross section by a p-wave component under the assumption that the final state interaction was still taking place purely in the s-wave. Taking

$$A = B = f_s \tag{2.2.13}$$

and

$$C = D \tag{2.2.14}$$

as a complex constant, the total cross section can be expressed as

$$\sigma = \frac{4\pi p_\eta}{p_p}\left[|f_s|^2 + p_\eta^2|C|^2\right]. \tag{2.2.15}$$

Similarly, the asymmetry parameter turns to

$$\alpha = 2p_\eta \frac{\Re(f_s^* C)}{|f_s|^2 + p_\eta^2 |C|^2}. \tag{2.2.16}$$

Fitting the same data again with the new description yielded

$$\begin{aligned} f_B &= (50 \pm 8)(\mathrm{nb/sr})^{1/2}, \\ C/f_B &= \left[(-0.47 \pm 0.08 \pm 0.20) + i(0.33 \pm 0.02 \pm 0.12)(\,\mathrm{GeV}/c)^{-1}\right], \\ p_1 &= \left[(-4 \pm 7^{+2}_{-1}) \pm i(19 \pm 2 \pm 1)\right]\ \mathrm{MeV}/c, \\ p_2 &= \left[(103 \pm 4) \pm i(74 \pm 12^{+1}_{-2})\right]\ \mathrm{MeV}/c. \end{aligned} \tag{2.2.17}$$

The inclusion of the p-wave in the fit had an insignificant effect on the poles, changing their values only slightly, and thus confirmed the validity of the earlier pure s-wave description within this energy range.

In summary, measurements at both COSY-ANKE and COSY-11 found an extremely strong enhancement of the total cross section within $Q < 1\,\mathrm{MeV}$. A fit to the COSY-ANKE data revealed a pole in the scattering amplitude very close to the production threshold. This indicates a strong final state interaction of the $\eta\,{}^3\mathrm{He}$ system. However, a pole would also induce a change in the phase of the s-wave [23]. The angular dependence of the differential cross section revealed the rise of contributions from the p-wave already at surprisingly low energies of $Q \approx 4\,\mathrm{MeV}$. The energy dependence of the differential cross section asymmetry could be well described with a very rapid change in the phase of the s-wave amplitude [23]. All of the above is consistent with the presence of quasi-bound or virtual state of the $\eta\,{}^3\mathrm{He}$ system.

2.2.2 Photoproduction experiments

If the reasoning in section 2.2.1 is accurate and the shape of the differential cross section of the $\mathrm{d} + \mathrm{p} \to {}^3\mathrm{He} + \eta$ reaction is in fact caused by a strong interaction in the final state, this behaviour should also be found in other production channels in a similar way. An experiment with the $\gamma + {}^3\mathrm{He} \to {}^3\mathrm{He} + \eta$ reaction was performed at the Mainz accelerator facility MAMI with the TAPS detector [27] and later repeated with the combined Crystal Ball - TAPS set-up [28]. The earlier cross sections inhibited a different shape than the later findings and it was argued that this may have been an artefact arising from the background conditions [28]. Furthermore, the later measurement improved significantly on the statistical significance. Therefore, the focus here shall be on the newer results. Using a detection system with a large angular coverage and the capability to detect neutral tracks from γs, the reaction was studied in terms of the two dominant neutral decay modes of the η meson:

$$\begin{aligned} \eta &\to 2\gamma \quad \text{and} \\ \eta &\to 3\pi^0 \to 6\gamma. \end{aligned} \tag{2.2.18}$$

In fact, the total cross section of the $\gamma + {}^3\mathrm{He} \to {}^3\mathrm{He} + \eta$ reaction showed a similarly steep rise in the near threshold region. However, with a binning of the data of $4\,\mathrm{MeV}$ in terms of the beam energy E_γ for the $\eta \to 2\gamma$ channel[3], only three data points coincided with the energy range studied in the dp production. Resolution and statistics did not allow for a determination of the pole position with high precision.

The differential cross section displayed a behaviour that was not consistent with the model description of the data [28]. The steep rise of the total cross section similar to hadronic production, however, suggested that this behaviour is largely independent on the initial state. Therefore, the differential cross sections may have been significantly affected by a strong final state interaction [28].

The experimental set-up opens up the possibility of searching for the bound $\eta\,^3$He system below the η production threshold by attempting to observe its decay through $\pi^0 - \mathrm{p}$ back-to-back emission. If the η meson is produced within the nucleus, it could be captured by a nucleon which is then excited to the $S_{11}(1535)$ resonance [28]. It would then decay into πp in two-body kinematics. Due to the width of the resonance, it can already be produced at the production threshold of the $\eta\,^3$He system. The aforementioned structure observed in the earlier experiment [27] was first associated with such a decay. However, in the later experiment [28] it was found that this might have been caused by unfavourable background conditions.

2.3 Other η-nucleus systems

The ^{3}He is not the only nucleus that has been studied in terms of a possible interaction with the η meson. In fact, comparing the pole positions of η-nucleus systems for different mass numbers of the nucleus may provide further evidence for a bound η-nucleus state. If such states exist, the binding should become stronger when more nucleons become available for the η to interact with.

2.3.1 The $\eta\,^4$He system

Several experiments on the $\mathrm{d} + \mathrm{d} \to {}^4\mathrm{He} + \eta$ reaction were performed and studied the $\eta\,^4$He final state [29, 30, 31, 32]. Here, the cross section is substantially lower than in the case of the $\mathrm{d} + \mathrm{p} \to {}^3\mathrm{He} + \eta$ reaction, making the system experimentally more difficult to study.

The unpolarised data from the ANKE measurement revealed an anisotropy in $\cos\theta$ at their higher excess energy point at $Q = (7.7 \pm 0.8)\,\mathrm{MeV}$ [31]. However, from unpolarised data it is not clear whether this arises from the square of the p-wave amplitude or the $s-d$-wave interference [21]. The measurement with a tensor polarised beam revealed that the p-wave amplitude is likely to be rather small [32].

Using this information, a description taking into account the data from all the above experiments is possible with a fit to the scattering amplitude retaining only one pole:

$$f_0 = \frac{f_B}{1 - \frac{p_\eta}{p_1}}. \tag{2.3.1}$$

---

[3] For reference, the bin width in the $\eta \to 3\pi^0 \to 6\gamma$ channel was 8 MeV.

This yields the parameters [21]

$$\begin{aligned} |f_B|^2 &= (34 \pm 1)\mathrm{nb/sr}, \\ \Im(p_1) &= \pm(64 \pm 10)\,\mathrm{MeV}/c, \end{aligned} \tag{2.3.2}$$

which corresponds to a pole at an excess energy $|Q_0| = 4.3 \pm 1.3\,\mathrm{MeV}$ [21, 32]. The best fits to the experimental data available produced a positive value for the real part of the pole, which is forbidden by unitarity [21, 9]. It was therefore set to zero [21]. As already stated in section 2.2.1, the sign of imaginary part cannot be extracted this way.

Due to the additional nucleon and the smaller radius of the ^{4}He nucleus compared to the ^{3}He, it was argued that the η would be stronger bound here than in case of the ^{3}He [30]. This would in fact be consistent with the pole being further away from the respective production threshold, an implication that the $\eta\,^4$He system is in fact quasi-bound [21]. However, this line of reasoning has been put into question [33], suggesting that the $\eta\,^4$He binding might in fact be weaker than estimated. This was based on the fact that calculations for a bound $\eta\,^4$He system [33] would require a much larger real part of the scattering length $\Re(a_{\eta N})$ than the one derived from an earlier measurement with a simple optical model [30].

Recently, a more direct attempt to search for $\eta\,^4$He bound states was started with the WASA-at-COSY experiment [34]. The reactions $\mathrm{d} + \mathrm{d} \rightarrow {}^3\mathrm{He} + \mathrm{n} + \pi^0$ and $\mathrm{d} + \mathrm{d} \rightarrow {}^3\mathrm{He} + \mathrm{p} + \pi^-$ were investigated with a large data set. Both final states could be produced via the decay of the intermediate $\eta\,^4$He bound state. However, no narrow structure could be which could be associated with such a bound state was observed in the preliminary results. However, preliminary upper limits for the total cross sections for such a process were provided and range from 21 nb to 36 nb for the $\mathrm{d} + \mathrm{d} \rightarrow {}^3\mathrm{He} + \mathrm{n} + \pi^0$ and 5 nb to 9 nb for the $\mathrm{d} + \mathrm{d} \rightarrow {}^3\mathrm{He} + \mathrm{p} + \pi^-$ reaction [34].

2.3.2 The $\eta\,$d system

By the same logic as in section 2.3.1, the interaction between an η and a deuteron should be weaker than in case of the $\eta\,^3$He system. This state has been measured via both the $\mathrm{p} + \mathrm{d} \rightarrow \mathrm{p} + \mathrm{d} + \eta$ reaction [35, 36] and the quasi-free $\mathrm{p} + \mathrm{n} \rightarrow \mathrm{d} + \eta$ reaction [37, 38]. Both reactions show signs of an enhancement with respect to phase space for low invariant masses of the $\eta\,$d system.

Over time a wide range of possible $\eta\,N$ scattering lengths have been suggested by different authors[4]. Some of these were obtained through measurements, *e.g.* via the $\pi^- p \rightarrow \eta N$ reaction, others through different model calculations. Calculating the ηA scattering lengths from the $\eta\,N$ values is a difficult task that becomes more challenging with the increasing complexity of the system, *i.e.* the number of nucleons involved. In case of the $\eta\,$d system this has been done for a broad selection of $\eta\,N$ input values [39]. Taking just three examples with a small, an intermediate, and a large real part, the values of the $\eta\,N$

---

[4] A compilation of different $\eta\,N$ scattering lengths and the methods with which they were obtained can be found in Ref. [16].

scattering lengths of

$$\begin{aligned} a_{\eta N} &= (0.25 + i0.16)\mathrm{fm}, \\ a_{\eta N} &= (0.55 + i0.30)\mathrm{fm}, \\ a_{\eta N} &= (0.98 + i0.37)\mathrm{fm}, \end{aligned} \tag{2.3.3}$$

resulted in the scattering lengths of the $\eta\,\mathrm{d}$ system of

$$\begin{aligned} a_{\eta d} &= (0.73 + i0.56)\mathrm{fm}, \\ a_{\eta d} &= (1.64 + i2.99)\mathrm{fm}, \\ a_{\eta d} &= (-4.69 + i1.59)\mathrm{fm}, \end{aligned} \tag{2.3.4}$$

respectively. A qualitative discussion of these values can be found in Ref. [21]. The first one is close to the result found by Haider and Liu [17] and does not lead to the strong enhancement of the total cross section as it was seen in the experimental data. The other two describe the data reasonably well. However, one represents a quasi-bound $\eta\,\mathrm{d}$ system ($\Re(a_{\eta d}) < 0$) and the other a quasi-virtual, or quasi-anti-bound, one ($\Re(a_{\eta d}) > 0$). Hence, a description of the experimental cross section data with these values does not provide insight into whether the $\eta\,\mathrm{d}$ system is quasi-bound or quasi-virtual.

Another experiment on the quasi-free $\mathrm{p} + \mathrm{n} \to \mathrm{d} + \eta$ reaction has been proposed and performed with the ANKE experiment [40]. The analysis is currently in progress and aims to extract the scattering length from total cross sections in the near-threshold region. Furthermore, differential cross sections will be investigated in order to observe the rise of possible partial wave contributions higher than the s-wave.

Should there be a pole found in the scattering amplitude of similar size as in the case of the $\mathrm{d} + \mathrm{d} \to {}^4\mathrm{He} + \eta$ reaction, it would stand to reason that one is bound and the other one is unbound. Taking into account the reasoning in section 2.3.1, this would suggest that the $\eta\,{}^4\mathrm{He}$ system is quasi-bound whereas the $\eta\,\mathrm{d}$ system would be virtual. The situation for the $\eta\,{}^3\mathrm{He}$ system, with its pole being much closer to the production threshold, would remain unclear, though.

2.3.3 Higher mass η-nucleus systems

For nuclei with higher mass numbers, there have been measurements with the reactions $\gamma + {}^7\mathrm{Li} \to {}^7\mathrm{Li} + \eta$ [41] and $\mathrm{p} + {}^6\mathrm{Li} \to {}^7\mathrm{Be} + \eta$ [42, 43]. These systems become experimentally much more challenging since the nuclear levels in the final state play a role and are difficult to separate. The present data are difficult to analyse in terms of possible cross section enhancements very close to threshold and no clear statement on a possible final state interaction can be made here.

In an effort to find more direct evidence for an η-mesic nucleus, *i.e.* through the decay of such a state, several experiments pursued the detection of back-to-back πN pairs, similar to the method described in section 2.2.2. Measurements were performed on the reactions $\gamma + {}^{12}\mathrm{C} \to \pi^+ + n + N + X$ [44] and $\mathrm{p} + {}^{27}\mathrm{Al} \to {}^3\mathrm{He} + p + \pi^- + X$ [45]. In the former case, the resolution did not suffice to identify a signal. The latter suggested to have seen evidence for an $\eta^{25}\,\mathrm{Mg}$ state, but statistics were rather low and this result should be regarded with care.

Chapter 3

Motivation for this measurement

It was shown in chapter 2 that several reactions were investigated in terms of a strong final state interaction of the respective η-nucleus system. The strongest indications for quasi-bound or quasi-virtual state were found in the data from the $\mathrm{d} + \mathrm{p} \rightarrow {}^3\mathrm{He} + \eta$ reaction. The relatively large cross section and the full geometrical acceptance of the ANKE detector for the reaction in the near threshold region allowed the excitation function to be extracted in unprecedented detail [9]. The data could be described well with a strong s-wave final state interaction of the $\eta\,{}^3\mathrm{He}$ system. However, in deuteron-proton scattering, the s-wave $\eta\,{}^3\mathrm{He}$ system can be accessed from two different total spin states of the deuteron-proton system, *i.e.* $S = \frac{1}{2}$ and $S = \frac{3}{2}$. From only unpolarised data, these cannot be separated and one cannot determine whether the low-energy enhancement of the cross section arises from a pure final state interaction or if it might be affected by differences between the initial spin states as well. On the other hand, a measurement of the deuteron tensor analysing power T_{20} would be influenced by the initial spin states. An earlier measurement at Saclay provided four data points for this observable in the near threshold region. In order to discuss the influence of the initial spin states on T_{20}, however, the energy dependence of this observable has to be studied and therefore more data points across a wider energy range are needed. A new measurement of the $\vec{\mathrm{d}} + \mathrm{p} \rightarrow {}^3\mathrm{He} + \eta$ reaction is therefore desired in order to verify the final state interaction interpretation presented in section 2.2.

3.1 Formalism for polarised measurements

Before going into further details about how conclusions for the final state interaction can be drawn from a polarised measurement, some additional formalism has to be introduced. In general, there are two additional quantities that have to be included in the differential cross section: the polarisation and the analysing power. The polarisation is the degree to which the spin of an ensemble of particles, *e.g.* the beam or the target, is aligned is aligned with a certain direction. The analysing power, on the other hand, describes how sensitive the differential cross section of a reaction is to the polarisation and therefore depends on the scattering angle. If a process has an analysing power different from zero, it is sensitive to the spins in the initial state. With a known polarisation the analysing power can the be measured, and vice versa. In the following these observables will be explained in more detail, including their possible range of values and how they can be determined using the differential cross section.

The differential cross section of spin-1 particles in a polarised measurement can be written in terms of the unpolarised differential cross section, the three vector and six[1] tensor polarisations, and their corresponding analysing powers [46].

$$\left(\frac{d\sigma}{d\Omega}\right)_{pol} = \left(\frac{d\sigma}{d\Omega}\right)_0 \left(1 + \frac{3}{2}\sum_{i=1}^{3} p_i A_i + \frac{1}{3}\sum_{i,j=1}^{3} p_{ij} A_{ij}\right) \tag{3.1.1}$$

In eq. (3.1.1), the vector and tensor polarisations are denoted as p_i and p_{ij}, respectively, whereas the analysing powers are given in cartesian coordinates as A_i and A_{ij}. The analysing powers are functions of the scattering angle θ and parity constraints apply. Furthermore, they are subject to the relation:

$$p_{xx} + p_{yy} + p_{zz} = A_{xx} + A_{yy} + A_{zz} = 0. \tag{3.1.2}$$

The coordinates x, y, z typically refer to the Cartesian scattering frame (see fig. 3.2) where z is chosen as the direction of the incident particle $\mathbf{k}_{\text{in}}$. The y-axis is normal to scattering plane spanned by the incoming ($\mathbf{k}_{\text{in}}$) and the outgoing particle ($\mathbf{k}_{\text{out}}$), so that y is in the direction $\mathbf{k}_{\text{in}} \times \mathbf{k}_{\text{out}}$. The x-axis is chosen so that it completes the right handed coordinate system. It transforms into the laboratory system x', y', z' by rotation around the z-axis by the azimuthal angle ϕ given by the direction of the outgoing particle. The components of a three-vector $\mathbf{p}$ would then transform via [46]:

$$\begin{pmatrix} p_x \\ p_y \\ p_z \end{pmatrix} = \begin{pmatrix} \cos\phi & -\sin\phi & 0 \\ \sin\phi & \cos\phi & 0 \\ 0 & 0 & 1 \end{pmatrix} \begin{pmatrix} p_{x'} \\ p_{y'} \\ p_{z'} \end{pmatrix} \tag{3.1.3}$$

While it is entirely possible to have all three vector polarisation components in the incident beam, due to parity conservation the reaction is only sensitive to those components which are normal to the scattering plane. Also due to parity, the reaction is only sensitive to the polarisations given in eq. (3.1.4) [46].

$$\left(\frac{d\sigma}{d\Omega}\right)_{pol} = \left(\frac{d\sigma}{d\Omega}\right)_0 \left(1 + \frac{3}{2} p_y A_y + \frac{2}{3} p_{xz} A_{xz} + \frac{1}{6} p_{xx-yy} A_{xx-yy} + \frac{1}{2} p_{zz} A_{zz}\right) \tag{3.1.4}$$

In the x', y', z' frame, it becomes [46]

$$\begin{aligned} \left(\frac{d\sigma}{d\Omega}\right)_{pol} = \left(\frac{d\sigma}{d\Omega}\right)_0 \Bigg(1 &+ \frac{3}{2}(p_{x'}\sin\phi + p_{y'}\cos\phi)A_y + \frac{2}{3}(p_{x'z'}\cos\phi - p_{y'z'}\sin\phi)A_{xz} \\ &+ \frac{1}{6}(p_{x'x'-y'y'}\cos 2\phi - 2p_{x'y'}\sin 2\phi)A_{xx-yy} \\ &+ \frac{1}{2}p_{z'z'}A_{zz}\Bigg). \end{aligned} \tag{3.1.5}$$

---

[1] While eq. (3.1.1) might give the impression that there are nine tensor polarisation, note that there is no difference between *e.g.* A_{12} and A_{21}.

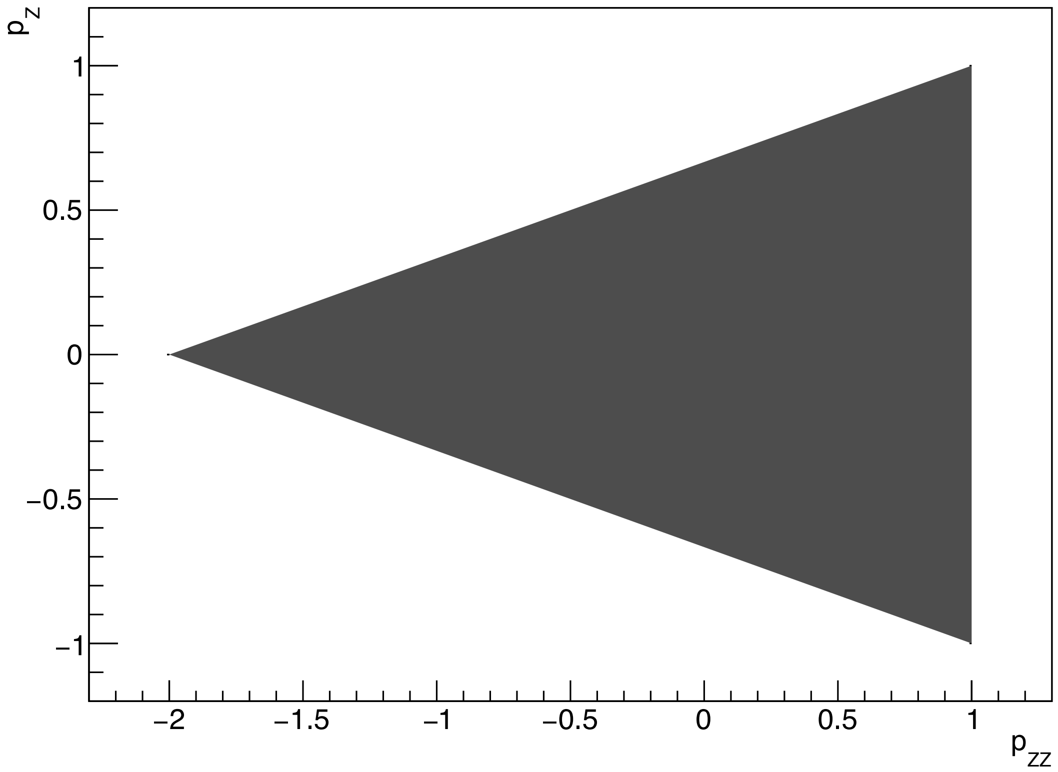

Figure 3.1: Correlation of the vector polarisation p_Z and the tensor polarisation p_{ZZ}. The shaded area shows all possible combinations of p_Z and p_{ZZ}.

The spin quantisation axis $\vec{S}$ in fig. 3.2 is used to characterise a polarised ensemble of particles. For spin-$\frac{1}{2}$ there are only two projections of the spin available, which correspond to the two magnetic states. In case the ensemble is a polarised beam produced by an ion source, usually another system X, Y, Z is introduced relative to the frame of the source. The quantisation axis is taken along the direction of the source's magnetic field. Then, Z is chosen along the quantisation axis while X and Y are arbitrary [46]. If we denote the fraction of particles in either of the two of the magnetic substates as $N^{\uparrow}$ and $N^{\downarrow}$, the vector polarisation of the ensemble can be written as:

$$p_Z = N^{\uparrow} - N^{\downarrow}. \tag{3.1.6}$$

For spin-1 particles, however, and additional magnetic state with the projection 0, with its population fraction denoted as N^0, comes into play, so that the tensor polarisation has to be written as:

$$p_{ZZ} = N^{\uparrow} + N^{\downarrow} - 2N^0. \tag{3.1.7}$$

These values may vary within different ranges. The vector quantities p_i and A_i can assume values between -1 and +1. For the tensor quantities, whereas p_{ii} and A_{ii} assume values between -2 and +1. Finally, the the tensor quantities p_{ij} and A_{ij} may vary between $-\frac{3}{2}$ and $+\frac{3}{2}$. By comparing eqs. (3.1.6) and (3.1.7), it becomes clear that p_Z and p_{ZZ} are correlated through $N^{\uparrow}$ and $N^{\downarrow}$. Hence, the range of possible combinations of p_Z and p_{ZZ}

is governed by that correlation. Figure 3.1 shows all the allowed combinations of p_Z and p_{ZZ}.

The polarisations of the ion source have to be related to the system in which the reaction is studied, *i.e.* the laboratory system. Defining β as the angle between the quantisation axis and the direction of the beam, the values of the vector polarisation can be transformed via [46]

$$\begin{aligned} p_{x'} &= 0 \\ p_{y'} &= p_Z \sin\beta \\ p_{z'} &= p_Z \cos\beta, \end{aligned} \tag{3.1.8}$$

whereas the tensor polarisations in the laboratory system are [46]

$$\begin{aligned} p_{x'x'} &= -\frac{1}{2} p_{ZZ} \\ p_{y'y'} &= \frac{1}{2}(3\sin^2\beta - 1) p_{ZZ} \\ p_{z'z'} &= \frac{1}{2}(3\cos^2\beta - 1) p_{ZZ} \\ p_{x'y'} &= 0 \\ p_{x'z'} &= 0 \\ p_{y'z'} &= \frac{3}{2}\sin\beta\cos\beta p_{ZZ} \\ p_{x'x'} - p_{y'y'} &= -\frac{3}{2}\sin^2\beta p_{ZZ}. \end{aligned} \tag{3.1.9}$$

In the experiment, the polarisation axis was vertically aligned with respect to the direction of the deuteron beam, *i.e.* $\beta = 90°$. Therefore, using the relations in eqs. (3.1.8) and (3.1.9) the differential cross section can be simplified even further [46]:

$$\begin{aligned} \left(\frac{d\sigma}{d\Omega}(\theta,\varphi)\right)_{pol} = \left(\frac{d\sigma}{d\Omega}(\theta)\right)_0 \Bigg(1 &+ \frac{3}{2} p_Z A_y(\theta) \cos\varphi \\ &+ \frac{1}{4} p_{ZZ} \left[A_{yy}(\theta)(1+\cos 2\varphi) + A_{xx}(\theta)(1-\cos 2\varphi)\right]\Bigg). \end{aligned} \tag{3.1.10}$$

The analysing powers depend both on the beam energy and the scattering angle θ between the incoming beam and the outgoing particles. In order to determine the polarisation, a reaction with known analysing powers has to be analysed in terms of its differential cross sections and then comparing these for polarised and unpolarised data.

Alternatively, the analysing powers can be written down in spherical coordinates. The spherical vector and tensor analysing powers T_{ij} relate to the ones in Cartesian coordinates

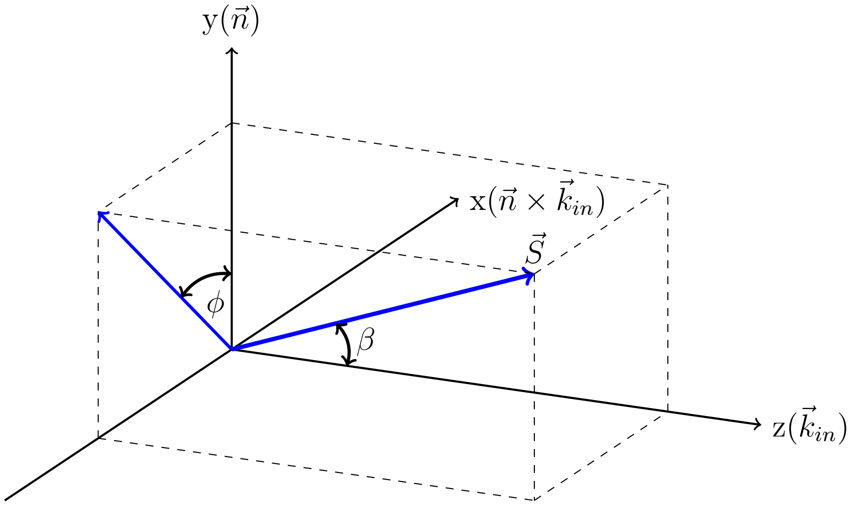

Figure 3.2: The helicity frame of the projectile according to the Madison convention [46]. The incident deuteron beam traverses in the direction $\vec{k}_{in}$ along the z-axis. The y-axis is defined as normal to the scattering plane spanned by the incoming particle with $\vec{k}_{in}$ and the outgoing particle with $\vec{k}_{out}$, *i.e.* $\vec{n} = \vec{k}_{in} \times \vec{k}_{out}$. The x-axis is chosen to complete the Cartesian coordinate system along the direction of $\vec{n} \times \vec{k}_{in}$. The blue arrows show the spin quantisation axis $\vec{S}$ and its projection on the xy-plane.

by [46]

$$iT_{11} = \frac{\sqrt{3}}{2} A_y \tag{3.1.11}$$

$$T_{20} = \frac{1}{\sqrt{2}} A_{zz} \tag{3.1.12}$$

$$T_{21} = -\frac{1}{\sqrt{3}} A_{xz} \tag{3.1.13}$$

$$T_{22} = \frac{1}{2\sqrt{3}} (A_{xx} - A_{yy}). \tag{3.1.14}$$

Accordingly, the differential cross sections can then be written as

$$\left(\frac{\mathrm{d}\sigma}{\mathrm{d}\Omega}\right)_{pol} = \left(\frac{\mathrm{d}\sigma}{\mathrm{d}\Omega}\right)_0 \left(1 + \sqrt{3} p_Z iT_{11}(\theta) \cos\phi - \frac{1}{2\sqrt{2}} p_{ZZ} T_{20}(\theta) - \frac{\sqrt{3}}{2} p_{ZZ} T_{22}(\theta) \cos 2\phi \right), \tag{3.1.15}$$

which is equivalent to eq. (3.1.10).

3.2 Spin dependence in the final state interaction

In a pure s-wave interpretation of the final state interaction, the scattering amplitude can be written in terms of just the two $\eta\,{}^3$He s-wave amplitudes A and B,

$$f = \bar{u}_{^3\mathrm{He}} \hat{p}_\mathrm{p} \cdot \left(A \vec{\varepsilon}_\mathrm{d} + iB \vec{\varepsilon}_\mathrm{d} \times \vec{\sigma}\right) u_\mathrm{p}, \tag{3.2.1}$$

where $\bar{u}_{^3\mathrm{He}}$ and u_p are the spinors of the ^{3}He and proton, respectively, $\hat{p}_\mathrm{p}$ the direction of the incoming proton in the centre of mass system, $\vec{\epsilon}_\mathrm{d}$ the polarisation vector of the deuteron, and $\vec{\sigma}$ the Pauli matrix [24]. This yields for the differential cross section:

$$\frac{d\sigma}{d\Omega} = \frac{1}{3}\frac{p_f}{p_i}\left[|A|^2 + 2\cdot|B|^2\right]. \tag{3.2.2}$$

In eq. (3.1.15) it can be seen that the differential cross section is affected by the vector analysing power iT_{11} and the two tensor analysing powers T_{20} and T_{22}. While the analysing powers themselves all depend on the polar angle θ, the iT_{11} and T_{22} terms go also with the azimuthal angle via $\cos\phi$ and $\cos 2\phi$, respectively. It is clear that these two terms vanish when the differential cross sections are averaged over the whole range of the azimuthal angle ϕ, therefore leading to a simpler relation for T_{20}:

$$T_{20}(\theta) = \frac{2\sqrt{2}}{p_{ZZ}}\cdot\left(\frac{\left(\frac{d\sigma}{dt}(\theta)\right)_0 - \left(\frac{d\sigma}{dt}(\theta)\right)_{pol}}{\left(\frac{d\sigma}{dt}(\theta)\right)_0}\right) \tag{3.2.3}$$

It follows from eq. (3.2.2) that the tensor analysing power can be expressed in terms of the energy dependent amplitudes A and B:

$$T_{20} = \sqrt{2}\frac{|B|^2 - |A|^2}{|A|^2 + 2|B|^2}. \tag{3.2.4}$$

If there is in fact no spin dependence in the scattering amplitude, then the squared amplitudes $|A|^2$ and $|B|^2$ should have the same energy dependence. More precisely, they can be expressed by a constant factor A_0 and B_0, while their energy dependence is introduced by the final state interaction term $\mathrm{FSI}(p_f)$:

$$\begin{aligned} |A|^2 &= |A_0|^2\cdot\mathrm{FSI}(p_f) \\ |B|^2 &= |B_0|^2\cdot\mathrm{FSI}(p_f). \end{aligned} \tag{3.2.5}$$

Consequently, using these amplitudes as input for eq. (3.2.4), it immediately becomes clear that any energy dependence in T_{20} cancels out in such a case:

$$T_{20}(p_f) = \sqrt{2}\cdot\frac{|B_0|^2 - |A_0|^2}{|A_0|^2 + 2|B_0|^2}\cdot\frac{\mathrm{FSI}(p_f)}{\mathrm{FSI}(p_f)} = const. \tag{3.2.6}$$

A measurement of the $\vec{\mathrm{d}} + \mathrm{p} \to {}^3\mathrm{He} + \eta$ reaction with a tensor polarised beam and a similar set-up to the one used for the earlier unpolarised measurement at COSY-ANKE [9] would open up the possibility of studying the spin dependence of the scattering amplitude and thereby verify whether or not $|A|^2$ and $|B|^2$ show the same energy dependence.

3.3 Goals for this experiment

The central goal of the measurement presented in this thesis is to study the energy dependence of the tensor analysing power T_{20}. An earlier experiment at Saclay measured this observable at four energies up to an excess energy $Q \approx 5\,\mathrm{MeV}$ [19]. While these

values were consistent being constant, the results were not compelling and did not allow to draw any solid conclusions. It was estimated that a measurement with the COSY-ANKE experiment would provide the necessary detail to quantify a possible spin dependence in the final state interaction of the $\vec{\mathrm{d}} + \mathrm{p} \to {}^3\mathrm{He} + \eta$ reaction [47].
It has been shown that the vector analysing power iT_{11} can be written in terms of the four amplitudes A, B, C, and D as [23]

$$IiT_{11} = \sqrt{3}\Im(A^*C - BD^*)p_\eta \sin\theta_\eta. \tag{3.3.1}$$

For a pure s-wave interpretation the p-wave amplitudes become $C = D = 0$, hence iT_{11} should clearly vanish and thereby becomes a useful observable to verify the validity of this interpretation. Using a deuteron beam that is also vector polarised, any contribution from iT_{11} would manifest as an asymmetry in the azimuthal angle ϕ due to its $\cos\phi$ dependence in eq. (3.1.15). Even though the unpolarised data could be well described by the pure s-wave interpretation, they also showed contributions from p-waves in the observed energy range. Therefore, the energy dependence of the vector polarisation asymmetries has to be studied to ensure the validity of the T_{20} results.
As will be shown in section 7.7, combining the T_{20} results with the information on $|f|^2$ obtained in the unpolarised measurement, it is possible to extract the squared amplitudes $|A|^2$ and $|B|^2$. These would be affected by any possible energy dependence in T_{20} and the impact of such an energy dependence can be judged against the overall variation of the scattering amplitude by the determination of $|A|^2$ and $|B|^2$.

Chapter 4

Experimental setup

4.1 COSY

The **CO**oler **SY**nchrotron COSY [48] as depicted in fig. 4.1 is a storage ring operating at intermediate energies and is located within the research centre in Jülich. It features two methods for cooling the particle beam (hence the name). At low momenta up to 0.65 GeV/c , a cold electron beam can be lead along the way of the accelerator beam particles. The two beams align with each other through the Coulomb interaction, resulting in a reduced entropy of the COSY beam. At higher momenta above 1.5 GeV/c per nucleon a stochastic cooling becomes possible. Two pick up electrodes register the transversal momentum profile of the beam. This information is passed to a kicker electrode on the opposite side of the ring which then compensates the transversal motion of the particle bunch.

The storage ring has a racetrack shape with a circumference of 184 m. The two 52 m long turns are connected by two 40 m long straights. 24 dipole magnets keep the particle beam on track in the turns, whereas 56 quadrupole magnets focus the beam on the straights. A set of sextupole magnets is only used to compensate chromatic errors when the beam is extracted for an external experiment.

COSY has a possible momentum range from 0.3 GeV/c up to 3.7 GeV/c with a momentum resolution of $\Delta p/p \approx 5 \cdot 10^{-4}$, which can be improved to $\Delta p/p \approx 1 \cdot 10^{-4}$ with the aforementioned cooling mechanisms. The absolute value of the momentum, calculated from the beam's orbit length measured with beam position monitors, is known with a precision of one permille. However, this can be improved by an order magnitude using a spin resonance method. This was first tested at the end of the beam time presented here and later used during a high precision measurement of mass of the η meson. It has been described in detail in [49, 50, 51].

4.1.1 Polarised source

In order to operate COSY with polarised protons or deuterons, a polarised ion source is used to inject negatively charged H^- and D^- ions into the cyclotron. Figure 4.2 shows a sketch of its setup.

On the right hand side of the fig. 4.2 neutral, unpolarised hydrogen and deuterium gas molecules are dissociated by an RF discharge. In order to suppress recombination on

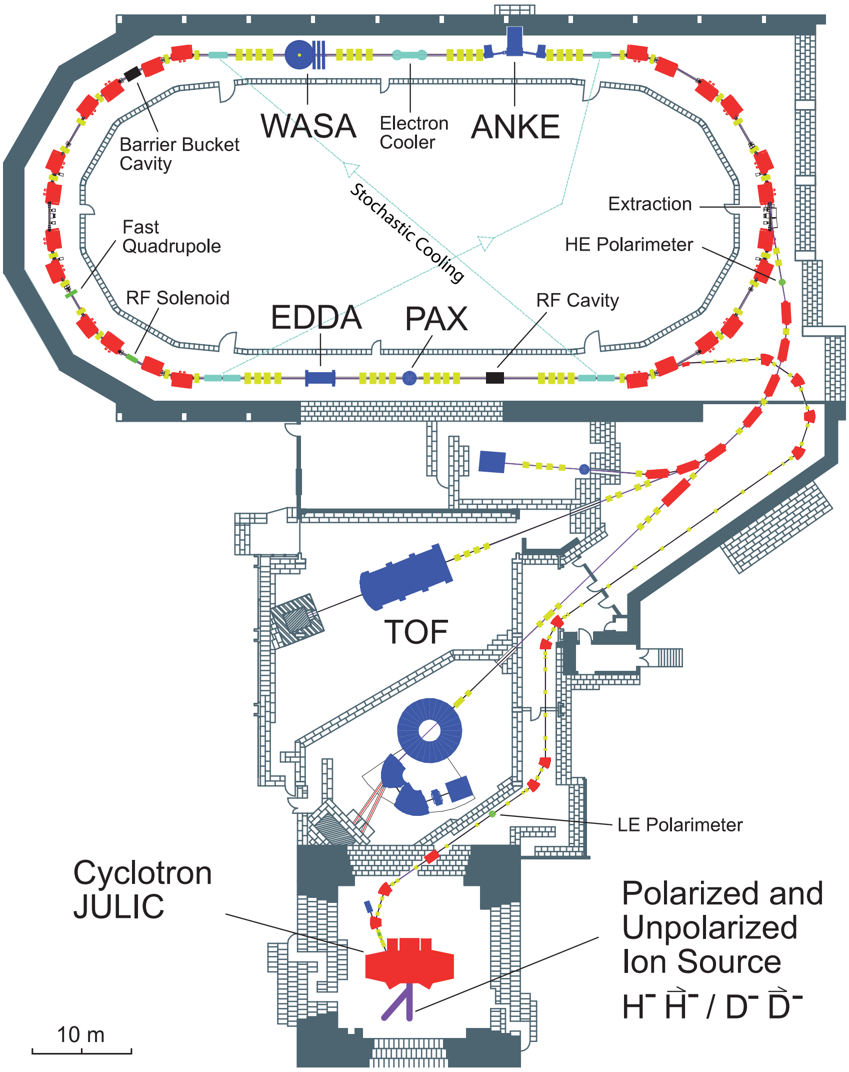

Figure 4.1: Schematic overview of the storage ring COSY at the time of the measurement presented here in 2007. Picture taken from Ref. [49].

the surface and in the volume, small amounts of nitrogen and oxygen are added [53]. A system of sextupole magnets separates the remaining molecules from the atomic beam. The first one defocuses atoms with an electron spin state $m_j = -1/2$, leaving only atoms with $m_j = +1/2$ in the beam [54]. The second one focuses the remaining beam into the ionising region. Two radio transition units shift the population of the hyperfine substates of the hydrogen atoms. For D^- beams different combinations of vector and tensor polarisation can be realised by using more RF transition units and sextupoles in order to manipulate the population numbers of the different hyperfine states in the deuteron [53].

In the charge-exchange region the beam collides with neutral Caesium atoms, gaining an electron due to the higher electro-negativity of the hydrogen, thus creating a negatively charged ion beam.

The acceptance of the first sextupole magnet is inversely proportional to the atomic beam temperature. An increased dwell time in the charge-exchange region increases

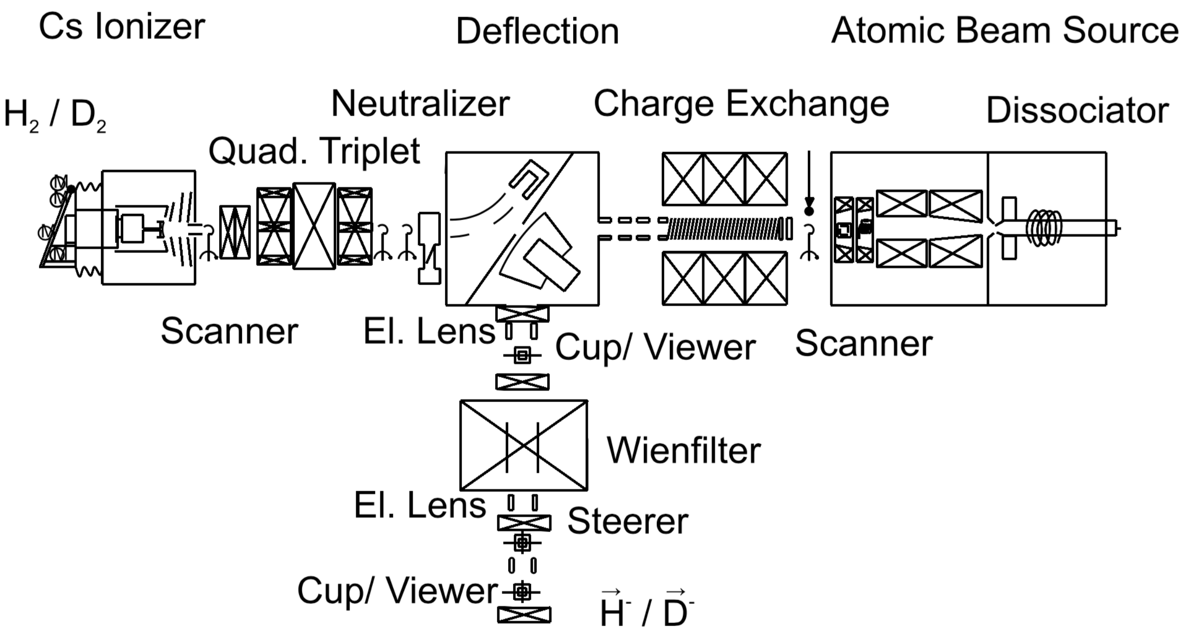

Figure 4.2: The polarised ion source used at COSY. Picture taken from Ref. [52].

the efficiency of the charge-exchange process, making a lower beam velocity even more desirable. Therefore, the atomic beam is cooled to approximately 30K while it passes through an aluminum nozzle. However, the advantages of cooling the beam are somewhat mitigated by scattering in the vicinity of the nozzle.
Finally, the ionised H^-/D^- beam is deflected by 90° into the injection beam line of the cyclotron. A Wien filter separates the negatively charged ions from electrons and background. In can be rotated in order to be able to provide any orientation of the polarisation axis. However, in reality the spin quantisation axis is aligned with the magnetic field of the cyclotron and no polarisation is lost during acceleration.

4.2 ANKE

The **A**pparatus for Studies of **N**ucleon and **K**aon **E**jectiles [55], short ANKE, is an internal experiment on one of the straight sections of COSY. Several different targets, both polarised and unpolarised, can be installed, a set of three dipole magnets serves as a magnetic spectrometer and multiple detections systems are in place in order to detect charged particles in a wide angular range. A sketch of the system can be found in fig. 4.3. Where other experiments often strive for an angular coverage as close as possible to 4π in the laboratory system, *i.e.* covering all angles around the interaction point, ANKE takes advantage of being a fixed target experiment and the associated strong forward boost of the ejectiles by focusing on high precision momentum reconstruction. This plays out particularly well for measurements as the one presented here. A two-body reaction like $\vec{\mathrm{d}} + \mathrm{p} \to {}^3\mathrm{He} + \eta$ investigated close to its production threshold will have a small momentum spread for its ejectiles, therefore leading to full angular acceptance for the ^{3}He particles in the forward detection system. The D2 dipole magnet then has a crucial role as it separates the reaction products from the remaining beam particles which

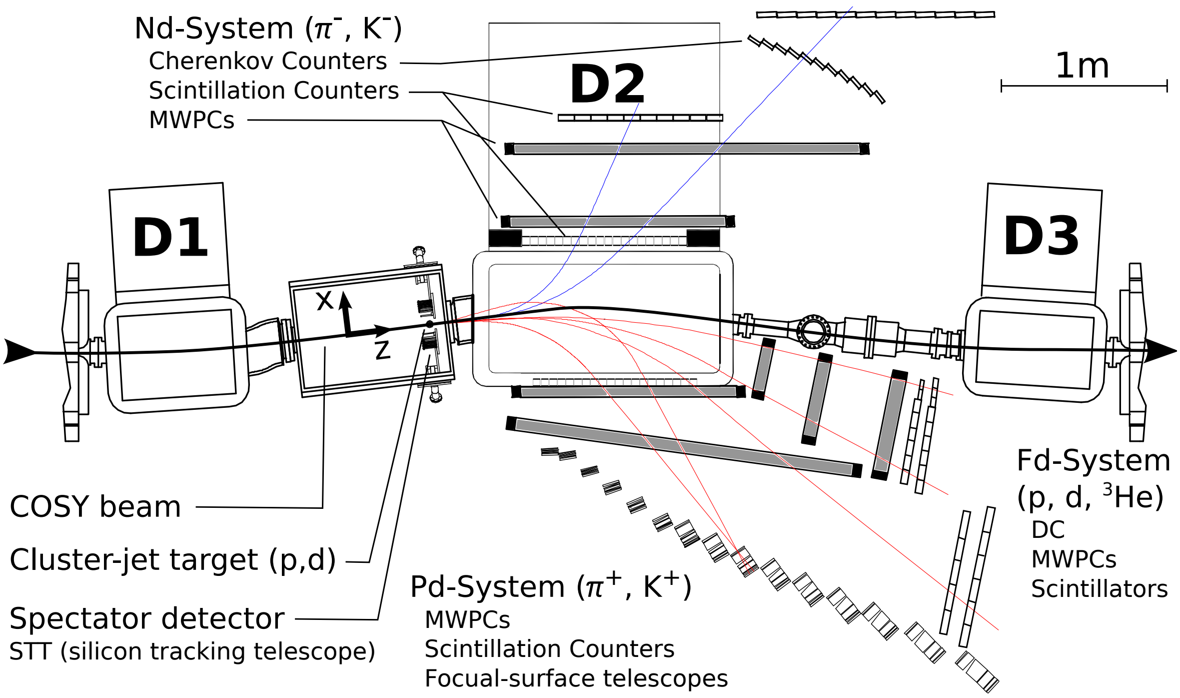

Figure 4.3: Sketch of the standard ANKE detector set-up. For the measurement presented here one of the hodoscope layers of the positive detection system was moved to act as a third hodoscope layer in the forward detection system. Picture taken from Ref. [49].

haven't interacted with the target. Depending on their charge and momentum, they are then deflected towards different detection systems. At the same time, the other two dipole magnets D1 and D3 fulfill their role of first deflecting the beam from its original orbit and guiding it back to it afterwards, respectively. In order to tune the geometrical setup to the respective measurement, the D2 magnet is mounted on a movable platform so that the deflection angle α can be changed from 0° up to 10.6°. Accordingly, the magnetic field B of the D2 dipole can be ramped up to 1.57 T.

A variety of different targets can be installed in order to study different processes. Using a solid strip target, interactions of the beam particles with heavier nuclei can be studied. The polarised gas target, comprised of an atomic beam source and a storage cell, enables the study of spin observables in single or double polarised scenarios. This measurement, however, was conceived as a single polarised experiment in which both the vector and tensor polarisation are provided by the deuteron beam which scatters on an unpolarised proton target. The cluster-jet target, explained in section 4.2.1, provides the ideal conditions for such a measurement.

4.2.1 Cluster-jet target

Measurements at an internal experiment introduce special challenges for the target that is used. For example, the vertex region has to be sufficiently well known and confined in order to achieve a good resolution of the four momentum vectors during track reconstruction. Furthermore, the density needs to be tuned to the experimental conditions. If the

density is too high, therefore heating up the accelerator beam, the cooling mechanisms might not be able to compensate anymore. Also, the number of interactions might exceed the capabilities of the detector or the data acquisition system. On the other hand, a density too low might not lead to any meaningful amount of data.
Since the accelerator beam requires an ultra high vacuum in order to avoid beam losses or deterioration of the beam's momentum resolution, a pressure of 10^{-6} mbar or better at the intersection of the target and the beam line, *i.e.* the scattering chamber, has to be maintained.

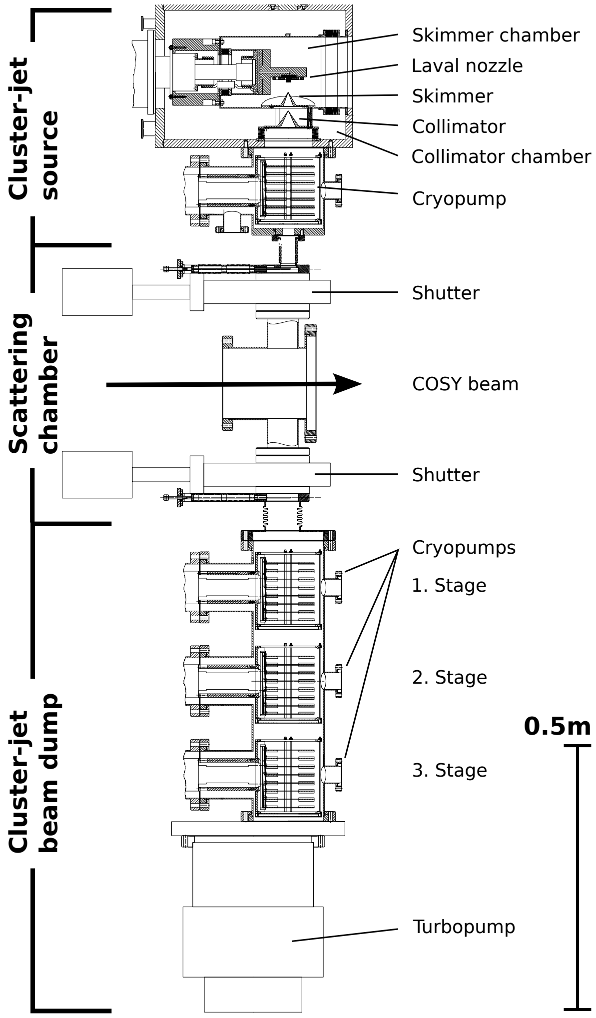

Figure 4.4: The cluster-jet target. Picture taken from [49].

The cluster-jet target [56, 57] easily masters these challenges. A sketch is shown in fig. 4.4. Its two sections, the cluster-jet source and the beam dump, are separated by the scattering chamber.
As the name suggests, the cluster-jet is produced in the source. The injected gas, which can be either hydrogen or deuterium, is cooled by a cold head below the vapour pressure curve to 20 to 30 K. At the laval nozzle, which has an orifice with a diameter of approximately 20 μm, a pressure of 15 to 20 bar is maintained. To prevent the gas from

freezing out at this point, a high purity of the hydrogen gas is essential. Therefore, a gas purifier using a heated palladium membrane is used to keep the pollution at a level below 0.5 ppm [58]. This becomes particularly important when working with deuterium, since this gas is usually not available with the same degree of purity as hydrogen. The clusters are generated in the laval nozzle. Through adiabatic expansion the temperature of the pre-cooled gas is lowered even further. This leads to the gas being in an oversaturated state within the nozzle and micro droplet, the so-called clusters, form [59]. These clusters are comprised of several thousand atoms [60, 61].

The cluster jet is separated from most of the residual gas by the skimmer. Its shape is given by the collimator. In the next stage the jet is headed towards the scattering chamber crossing the path of the accelerator beam. Finally, it enters the beam dump stage to be extracted by a system of cryo pumps and a turbo molecular pump which ensure that a high quality vacuum is maintained at all times.

For many years cluster-jet targets have been operated at the experiments ANKE and COSY-11, where they proven their reliability, stable working conditions and a high level of operating efficiency. As a consequence, further development on the target is being done and it will be operated at the future PANDA experiment at FAIR in Darmstadt [62, 63, 61]. As members of the ANKE collaboration, it was the responsibility of the corresponding member of the Münster group, including this author, to perform maintenance on the target and its peripheral systems[1] and ensure stable working conditions during the respective measurements.

4.2.2 Forward detection system

In the reaction $\vec{\mathrm{d}} + \mathrm{p} \to {}^3\mathrm{He} + \eta$ the only detectable ejectile at ANKE is the ^{3}He. Since it is getting a strong forward boost from the deuteron, its trajectory will be reasonably close to the beam pipe where the forward detection system is located. In fact, the setup for the beam time presented here was used and proven successful at an earlier measurement [9]. Figure 4.5 illustrates that the acceptance of the forward detection system for the ^{3}He ejectiles is nearly 100% even at an excess energy $Q = 20\,\mathrm{MeV}$.

The system itself is comprised of one multi-wire drift chamber (MWDC), two multi-wire proportional chambers (MWPC) and a two-layer scintillation hodoscope. A third hodoscope layer can be repurposed from the positive detection system in order to enhance particle identification, and can be seen as well in fig. 4.5.

The MWDC is positioned the closest to the D2 magnet where residual magnetics fields can still occur. Therefore, it has to satisfy the highest demands in terms of its spatial resolution. It contains three planes with vertically aligned, alternating cathode and anode wires, and four more planes in which the wires are inclined by 30°. The focus here lies clearly on the horizontal track reconstruction as the charged tracks are deflected in this plane by the D2 magnetic field. The typical resolution of this type of MWDC is approximately $200\,\mu$m. On the other hand, the MWPCs are placed a little further down the beam line, well outside the D2 magnetic field. They contain two sets comprised of on strip plane and two wire planes. One has the wires aligned vertically, the other horizontally with the strip plane being inclined by 18°. The wire spacing in each plane is 2 mm and the two planes are shifted with respect to each other, resulting in an effective

---

[1] For example, its gas system.

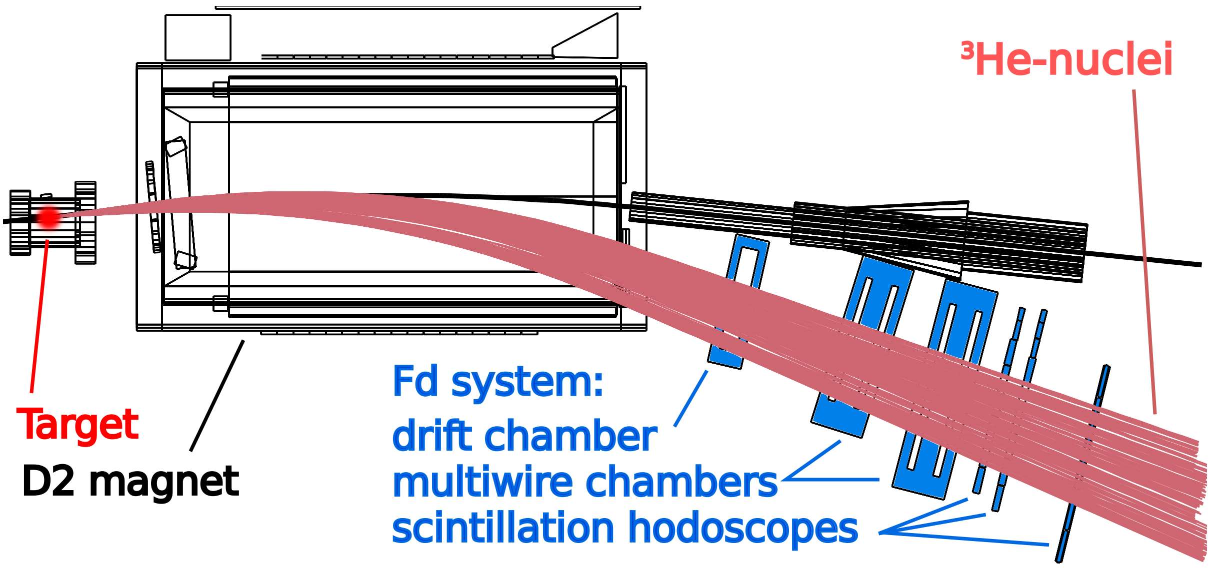

Figure 4.5: Top view of the ANKE forward detection system. The trajectories of the ^{3}He ejectiles (red) were simulated at an excess energy $Q = 20\,\mathrm{MeV}$. The simulation framework used for this picture still displays an older version of the scattering chamber. However, this does not affect the results.

distance of 1 mm between the wires of the combined planes. In total, a momentum reconstruction of approximately 1% can be achieved with this setup.

The two layers of the the forward hodoscope consist of eight and nine verticle scintillators, respectively. Six in each layer have a width of mm and a thickness of 20 mm. These are placed on the low momentum side away from the beam pipe (see also figs. 4.3 and 4.5). In the high momentum region, *i.e.* close to the beam pipe, the count rate increases, which could result in an increase in dead time of these scintillators. In order to compensate for that, the counters closer to the beam pipe have smaller sizes. All have a thickness of 15 mm, a varying width of 40 and 60 mm in the first plane, and 40, 50, and 60 mm in the second plane. All scintillation counters have a length of 360 mm. The third layer, taken from the positive detection system, consists of six modules with a width of 100 mm, a thickness of 10 mm, and a length of 1000 mm. The modules of all three layers are made of polystyrene and are read out at the top and the bottom using lucite light guides connecting them to phototubes [55]. The hodoscope can be used for triggering the data acquisition system. The triggers can be set up in a way that they only activate if a certain pulse height is reached and if a specified combination of layers is being hit (see also section 4.3.2). The scintillators are also used for particle identification in the offline analysis, where different kinds of particles can be separated based on the energy deposited in the modules (see section 7.1).

4.2.3 Other detection systems

For investigating the reactions $\vec{\mathrm{d}} + \mathrm{p} \to {}^3\mathrm{He} + \eta$ and $\mathrm{d} + \mathrm{p} \to \{\mathrm{pp}\}_s + \mathrm{n}$ only the forward detection system is required. Therefore, the other detections systems shall be mentioned here only briefly. While both the positive and negative detection systems, which can

be seen in fig. 4.3, were switched on during the measurement, no analysis based on the data collected during this measurment making use of them has been performed so far[2]. Similar to the forward detection system, they are comprised of a series of wire chambers and scintillation hodoscopes. In principle, the setup used for this measurement is well suited for investigations involving the production of multiple charged pions, and this has in fact been performed with a later measurement done in 2008 [64].
Figure 4.3 also shows the spectator detector. This consists of several silicon tracking telescopes designed for detecting charged low momentum particles, *e.g.* spectator protons that are produced when deuterium is used as an effective neutron target. A measurement making use of this can be found in [40].

4.3 Detector setup during the measurement

The general setup of the detector was based on the investigations carried out for an earlier measurement on the $\mathrm{d} + \mathrm{p} \to {}^3\mathrm{He} + \eta$ reaction [65]. In the proposal for this measurement [47], two weeks of beam time, including machine development[3], were requested. The goal was to obtain the excitation function in the excess energy range with $-5\,\mathrm{MeV} < Q < 11\mathrm{MeV}$ and group the data into bins of the excess energy with a width $\Delta Q = 1\,\mathrm{MeV}$, angular bins of $\Delta\cos\theta = 0.2$ and achieve a statistical uncertainty of 6% for the extracted differential cross sections [47]. Thereby, it would be possible the angular distributions with a similar quality as in the case of the unpolarised measurement [9]. A consideration was made whether to perform this measurement with several discrete beam cycles at different momenta, or rather with one continuously ramped cycle covering the whole desired energy range. The latter worked well for the unpolarised measurement [9] and has the advantage that systematic effects between the cycles, *e.g.* uncertainty of the beam momentum, could be largely avoided. In addition, it provided a larger flexibility in case it would become desirable to choose a different energy binning in the offline analysis. Therefore, a setting with continuously ramped beam was chosen (see also section 4.3.1). Furthermore, the data would be divided among one unpolarised and three polarised modes of the polarised ion source. The modes, which are given in table 4.1, were chosen to study the tensor analysing power T_{20} at different values of the polarisation, thus having some control over systematical effects. A non-zero vector polarisation for some modes would allow to study effects on the vector analysing power T_{11} as well.
A scheme for the deuteron beam setup was conceived in which the beam would first be accelerated to a fixed momentum $p_\mathrm{d} = 2.435\,\mathrm{GeV}/c$. Data taken at this momentum were dedicated for polarimetry, since a solid data base of analysing powers was already available for the quasi-free $\vec{\mathrm{n}} + \mathrm{p} \to \mathrm{d} + \pi^0$, and $\vec{\mathrm{d}} + \mathrm{p} \to \{\mathrm{pp}\}_s + \mathrm{n}$ reactions [66]. After an amount of time sufficient for data collection the beam would be accelerated again to a continous ramp starting at $p_\mathrm{d} = 3.118\,\mathrm{GeV}/c$ and linearly going up to $p_\mathrm{d} = 3.185\,\mathrm{GeV}/c$, which corresponds to an excess energy from $Q = -5\,\mathrm{MeV}$ up to $Q = 11\,\mathrm{MeV}$ with respect to the threshold of the $\vec{\mathrm{d}} + \mathrm{p} \to {}^3\mathrm{He} + \eta$ reaction. At the end of the ramp the beam

---

[2] Of course, as mentioned in section 4.2.2, one of the hodoscope layers of the positive detection system was used in conjunction with the forward detection system.

[3] The machine development is typically scheduled for one working week in the beginning of the beam time during which the requested beam settings are developed and the detector is set up.

Table 4.1: Modes of the polarised ion source. The ideal values for both the vector (p_Z) and tensor (p_{ZZ}) polarisations are given, whereas I_0 denotes the expected relative intensity of each mode, normalised to the unpolarised one.

Mode	p_Z	p_{ZZ}	**Intensity** I_0
0	0	0	1
5	0	-2	2/3
6	-1	+1	2/3
7	+1	+1	2/3

would be decelerated again to a fixed mometum of $p_\mathrm{d} = 2.435\,\mathrm{GeV}/c$ in order to ensure that the polarisation was maintained throughout the cycle. Since there were polarisation studies performed in the momentum range of the continuous ramp at the time of the proposal, it was desired to verify in this way that there were systematic effects causing a depolarisation. However, due to reasons detailed in section 4.3.3, this setup could not quite be realised in this way.

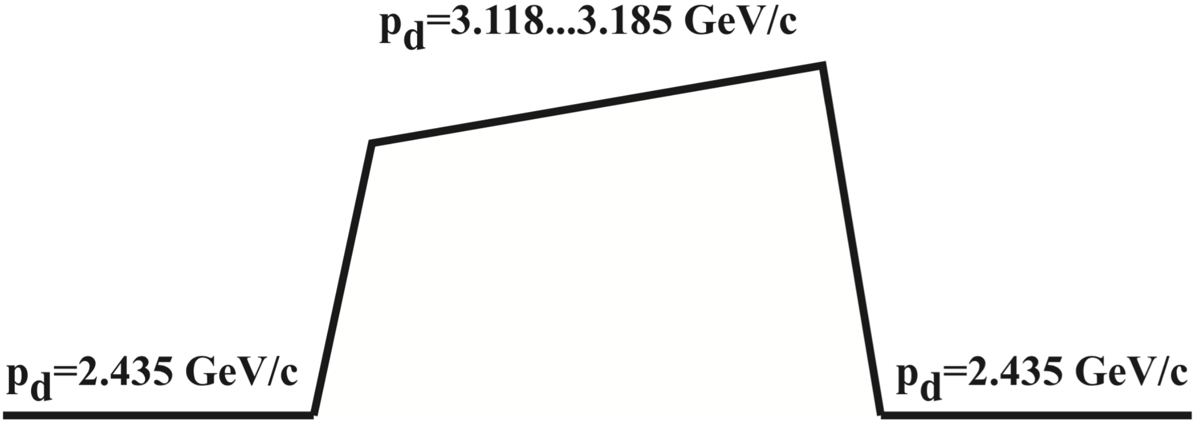

Figure 4.6: Planned setup for the COSY deuteron beam. The deuteron beam starts at a plateau, then jumps to a continuous ramp and finally decelerates back to the plateau again. Picture taken from Ref. [47].

4.3.1 COSY settings

In part due to unforeseen complications detailed in section 4.3.3 the actual beam settings had to be revised during the beam time. Based on the performance of the polarised ion source, a different set of three polarised modes was chosen. The nominal values are given in table 4.2. In addition the source also operated in an unpolarised mode. Having opposite tensor polarisation for modes 1 versus 2 and 3 would still allow to study systematic effects, whereas the non-zero vector polarisation would bring the aforementioned benefits.

A larger compromise had to be made in terms of the cycle setup. The scheme presented in fig. 4.6 could not be realised. Instead, a setting as shown in fig. 4.7 was chosen. The plateau and the continuous ramp were divided into individual cycles with 120 s dedicated

Table 4.2: Nominal values of the vector and tensor polarisations provided by the ion source.

Mode	p_Z	p_{ZZ}
0	0	0
1	+1/3	-1
2	-1	+1
3	+1	+1

to the plateau cycle and 310 s to the ramp cycle. The polarisation bit was alternated after each cycle. In order to avoid that the low momentum cycle would only be associated with odd and the ramp cycle with even polarisation numbers (or vice versa), a third, 10 s cycle was introduced.

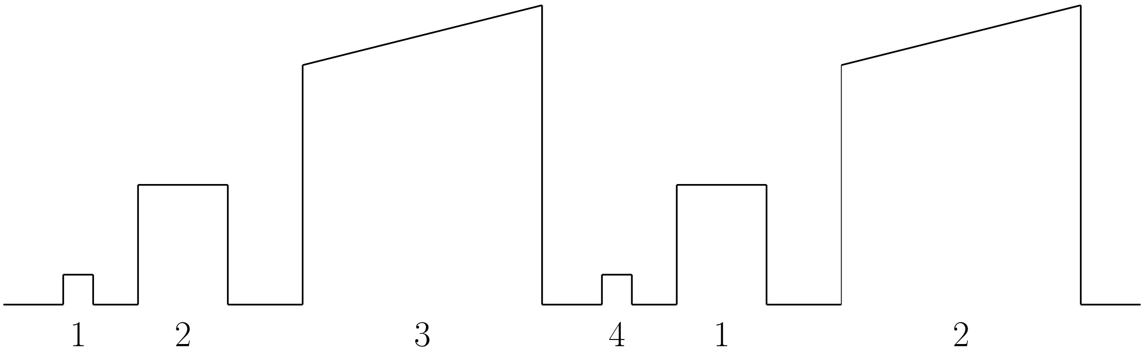

Figure 4.7: Final setup for the COSY deuteron beam used throughout the experiment. Three different cycles were combined into one supercycle. A very short with low momentum was only created for the purpose of having an odd number of cycles. A fixed momentum cycle at $p_d = 2.435\,\mathrm{GeV}/c$ was set up for the polarisation measurement and a continuous ramp from $p_d = 3.118\,\mathrm{GeV}/c$ to $p_d = 3.185\,\mathrm{GeV}/c$ for measurement of the $\vec{\mathrm{d}} + \mathrm{p} \to {}^3\mathrm{He} + \eta$ reaction. The numbers below the cycles indicate the rotation of the polarisation states of the ion source.

4.3.2 ANKE settings

The detector was set up in a similar way as for the earlier, successful measurement on the $\mathrm{d} + \mathrm{p} \to {}^3\mathrm{He} + \eta$ reaction [65]. The ANKE platform was moved to obtain a nominal deflection angle $\alpha = 5.9°$. One of the hodoscope layers of the positive detection system was moved to act as a third layer of the forward detection system, as it is illustrated in fig. 4.5. In order to maximise the geometrical acceptance, the individual modules of the third hodoscope layer were inclined by a few degrees and shifted to create some overlap between each two modules. This way, the usual 4 mm gaps, that had been observed during the earlier measurement, could be avoided. These could have caused problems when measuring very close to the production threshold of the $\mathrm{d} + \mathrm{p} \to {}^3\mathrm{He} + \eta$ reaction where the momentum sphere and therefore the geometrical spread of the ${}^3\mathrm{He}$ nuclei is very small, hence losing many events in one of the gaps. This idea was also reflected in the trigger scheme.

The purpose of the main trigger T1 was to specifically select events with ^{3}He ejectiles passing through the forward detection system. Events were selected based on one hit with a high energy loss in either of the first two layers and one in the third layer. This way, gaps in the acquired data caused by the 1 mm spacing between the modules of the first two layers were avoided as well, resulting in a 100% geometrical acceptance for the $\mathrm{d} + \mathrm{p} \to {}^3\mathrm{He} + \eta$ reaction throughout the whole investigated energy range. The high voltage signal produced in the readout of the counters is proportional to the deposited energy. When setting up the trigger, certain threshold values could be given that had to be surpassed in order for the signal to be registered. The thresholds of each counter were adjusted during the machine development period of the beam time using live energy loss spectra generated by an OnlineSorter[4] which had been prepared in advance.

A non-discriminatory trigger T2 was also used to collect events without any bias. Whenever signals were coincidently created in the first two layers of the forward hodoscope, event data would be collected. The third layer was ignored for this trigger. The high voltage thresholds of the hodoscope modules were set to only cut away pedestal signals. This trigger was mainly used for calibration purposes as well as polarimetry using the $\vec{\mathrm{d}} + \mathrm{p} \to \{\mathrm{pp}\}_s + \mathrm{n}$ reaction. However, since this trigger would create much more events than the data acquisition system would be able to cope with, it was pre-scaled by a factor of 1024.

Finally, a scaler trigger was running at a rate of 10 Hz, storing events with information on the experimental conditions, *e.g.* the beam current signal and individual trigger rates, necessary for example to determine the dead time later on during the analysis.

4.3.3 Experimental conditions

This beam time was affected by a chain of technical difficulties, which significantly reduced the amount of time for data taking as well as having an impact on the analysis procedure.

Delayed machine development

In the beginning of the COSY machine development, no stable beam conditions could be found with the deuteron beam consistently being lost shortly after injection. It was found after a few days that the reason was a defect power supply for one of the dipole magnets, which was quickly replaced. This left little time for beam development, hence making it necessary to revert to a simplified cycle setup as described in section 4.3.1. Furthermore, the setup processes of the ANKE detector, which depended on the availability of the deuteron beam, was delayed. Instead of starting the measurement already on Friday night of the first week of the two week beam time, final settings were only achieved on Tuesday of the following week, leaving approximately six days for the actual measurement. While this would still have been a substantial amount of time, further complications arose.

---

[4] The OnlineSorter is a control program used during the measurement. See also section 5.2.

Defect pressure gauge

Some time through the beam time, the shutters connecting the cluster-jet target and the scattering chamber (see also fig. 4.4) started to seemingly randomly close. This was quickly found to be correlated with the fast ramping of the D2 magnet in the beginning of a cycle. A COSY Penning tube used for measuring the pressure just above the scattering chamber was suspected to be defect or at least negatively affected by the magnetic field. However, neither a hastily assembled magnetic shielding nor a later replacement of the Penning tube itself alleviated this problem. Later on, a Pirani pressure gauge connected upstream of the Penning tube was found to be defect and being affected by the ramping of the D2 magnet, turning off the Penning tube whenever a new cycle began. It was estimated that nearly 12 hours of measurement were lost this way.

Deuteron beam and polarised ion source

Complications also occurred with the COSY accelerator and the polarised ion source, manifesting in complete losses of the deuteron beam or in very low beam intensities. Figure 4.8 shows the cycle-average of the beam current signal for the data used in the final analysis. It is plotted against number of the cycle, showing only the times when

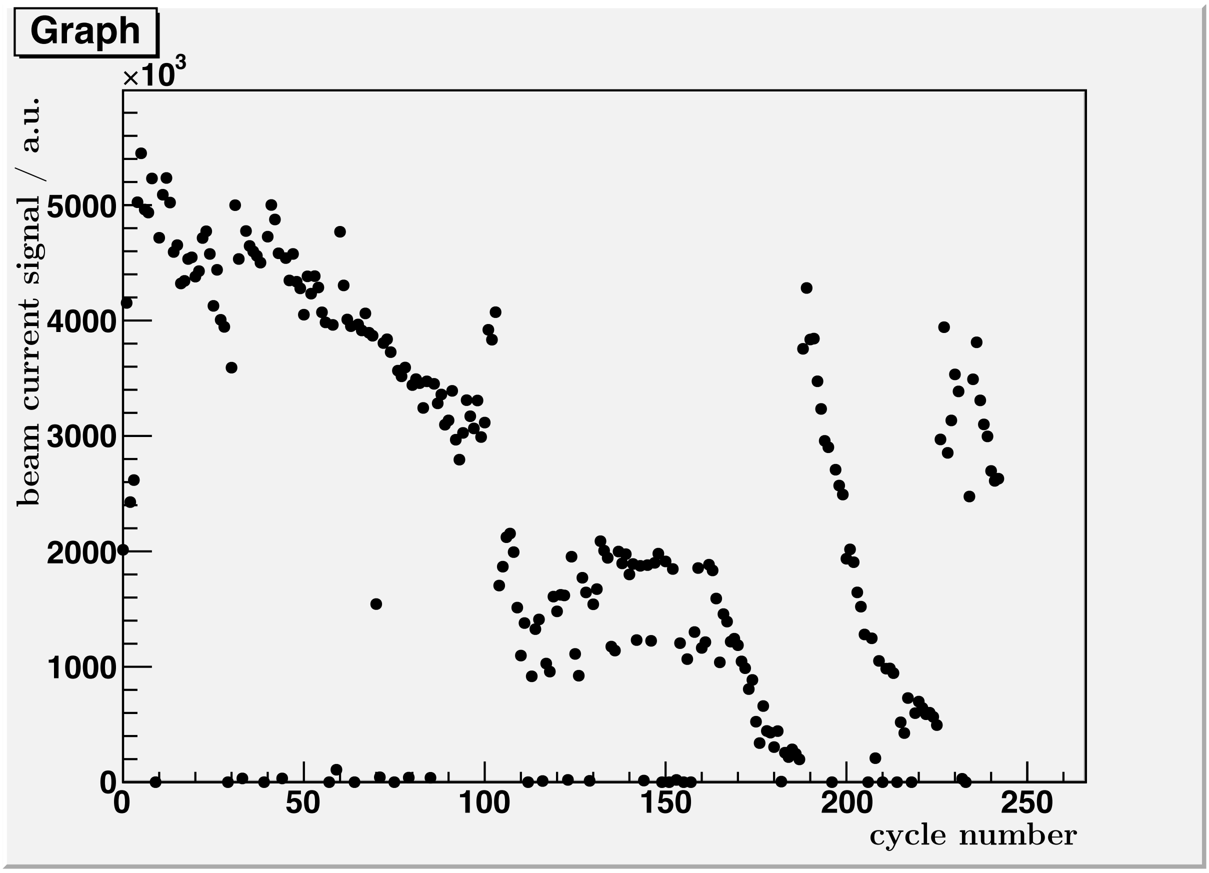

Figure 4.8: The beam current signal averaged for each cycle and plotted against the cycle number ranging from the beginning to end of the data used for the final analysis. The data presented were taken with unpolarised mode of the ion source.

the data acquition system was running. Peak intensities correspond to approximately $4 - 6 \cdot 10^9$ deuterons stored in COSY, which is a very solid number when working with the polarised ion source. As can be clearly seen in fig. 4.8, these intensities could not be maintained throughout the beam time, at times dropping by an order of magnitude. While fig. 4.8 only shows cycles with an unpolarised beam, the other polarisation modes followed the same general behaviour. The beam losses, polarised source maintenance and intensities below $1 \cdot 10^9$ deuterons in the ring amounted to approximately 31 hours.

Data acquisition system

Some complications arose from the experiment with the data acquisition system having had two significant outages caused by a software bug. For an estimated total of 12 hours, the system was offline.

Total downtime

In total, these issues led to an unforeseen downtime of approximately 55 hours, which have to be considered on top of the initial delay of the measurement caused by the aforementioned defect power supply. The downtime estimations are compiled in table 4.3.

Table 4.3: Approximate downtime caused by unforeseen technical difficulties. These values consider only the difficulties occurring after the start of the measurement.

Cause	**Downtime**
Pressure gauge	12 hours
Beam/source	31 hours
Data acquisition	12 hours
Total	55 hours

While the aforementioned issues account for the time during the measurement when no meaningful data could be acquired, further complications were only discovered during the later offline analysis.

Defect hodoscope module

One of the hodoscope modules most likely had an issue with the high voltage or the corresponding threshold. The affected module was the fourth from the beam pipe in the third layer. In turn, for this module basically all of the events of the $\vec{\mathrm{d}} + \mathrm{p} \rightarrow {}^3\mathrm{He} + \eta$

reaction were rejected. Since the idea of the measurement was based on having a full geometrical acceptance in conjunction with a flat efficiency distribution, the analysis had to be revised. The method leading to the final result is detailed in section 7.2. The trigger T2 and any part of the analysis based on this, *e.g.* the polarisation measurement described in chapter 6, was unaffected.

Low polarisation mode

As will be shown in section 6.2.3, polarisation mode 3 was found to have a very low tensor polarisation. The low polarisation causes the uncertainties for this mode to grow very large, leaving very little information to be extracted. On the other hand, clearly something did not work as intended and in order to avoid possible systematic effects for the final results, this mode was discarded.

Chapter 5

Software

While the experimental setup provides the physical tools necessary to acquire the data of the measurement, a dedicated software is essential to convert this raw information into meaningful physical quantities. A schematic overview of a few of the central frameworks is shown in fig. 5.1, which in large part have been established in this field of research for many years. These, together with a couple of essential, additional tools, will be described in more detail in this chapter.

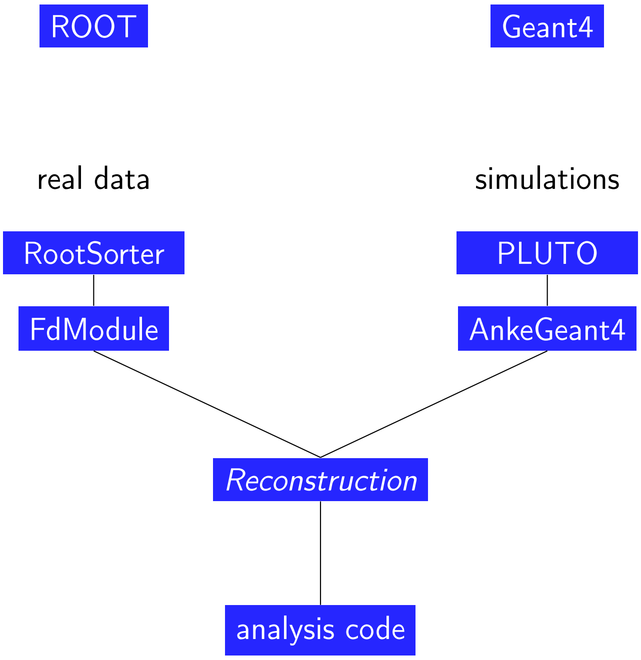

Figure 5.1: Schematic overview of the central software packages used for simulations and data analysis. Both ROOT and Geant4 are regarded as base requirements for many of the other packages here, and the connections to them have been left out for better visibility.

A special emphasis will be put on the *Reconstruction*, a framework conceived and in large part developed by this author. The goal was to bridge the gap between the entry-level programming skills of a student who is just starting out and the often difficult and unique requirements of an experiment's software framework. This was achieved by putting a renewed focus on basic and modern-day[1] programming concepts, such as a very modular approach and clear language conventions. A detailed description of the *Reconstruction* framework is given in 5.7.

5.1 ROOT

The ROOT Data Analysis Framework [67] has been developed at CERN and was specifically designed with high-energy physics experiments in mind. It provides an extensive set of tools related to analysis and simulations in this field of research which has led to it being used by a wide range of scientists all over the world. The framework is written in the C++ [68] programming language, but also integrates well with other languages like Python, R or even Mathematica. Some of the following software packages are based on ROOT and it is also used in a direct manner in order to e.g. represent particles by their corresponding four-momentum vectors and present physics data in the form of histograms.

5.2 RootSorter

Built on the foundation laid down by ROOT, the RootSorter [69] processes and visualises the raw data acquired with ANKE. Data from all the detector groups, *e.g.* energy losses in the scintillators or signals from the wire chambers, are collected and access is provided to the user. Different track reconstruction algorithms are available for all detector groups, but it should be noted that only the forward detection system was used for this work. For that particular system, an additional software package (see section 5.2.1) could be obtained and "plugged into" the RootSorter. Since it can take a significant amount of time to process a complete data set obtained during a given beam time[2], a pre-selection and pre-analysis based on the RootSorter including a full track reconstruction was usually performed in order to store data in an intermediate format as "branches" of a ROOT `TTree`. The results could be handled further in a much faster manner.

Executables, commonly referred to as "OnlineSorter", were derived from the RootSorter and acted as an online analysis in order to display user specified control spectra already during the data taking. It is essential to have these prepared before the beginning of the measurement in order to immediately identify any part of the experiment that might not be working as intended and ensure that the data taking is living up to the expectations.

5.2.1 FdModule

A software package dedicated for track reconstruction in the forward detection system, called the FdModule, could be obtained separately and integrated into the existing RootSorter [70]. Several algorithms are in place to fulfil its main purpose of reconstructing

---

[1] Since the project was started in 2008, the latest standard of the used programming language was C++03.

[2] Using all available CPU cores (including hyper-threading) on an Intel Core i7-2670QM a pre-selection of the data would take approximately 8 hours. Note that the hardware available at the time of data taking was less performant by roughly an order of magnitude.

a particles track, including a boxfield and polynomial approximation method [71]. However, this work solely relied on the Runge-Kutta method, which takes a more realistic approach. First, hits in the wire chambers are used to represent the particle's trajectory by a straight line outside the magnetic field of the D2 dipole. The trajectory is then propagated backwards through the previously measured field to the primary vertex, *i.e.* the interaction point. If it is impossible to trace the vertical component of the particles trajectory back to the beam target overlap region, the track will be discarded as "unrealistic". Included in the FdModule is also an analysis class which can serve as a place for the user to implement for example pre-selection cuts on the energy loss and store additional data in the output file.

5.3 PLUTO

PLUTO [72] is a ROOT-based event generator for Monte Carlo simulations which produces events of hadronic reactions with isotropic phase space distributions. The experimental conditions, *i.e.* the projectiles with their respective momenta as well as the resulting ejectiles have to be defined as input. This can include subsequent decays of the ejectiles based on their life time. The output of PLUTO is then the input for AnkeGeant4.

5.4 Geant4

Geant4 [73] was used as the base simulation toolkit. Particles of previously generated events (see section 5.3) can be propagated through matter, *i.e.* the detector. Transport models and simulation physics processes caused by the interaction of the moving particle with its surrounding matter are part of the package. This includes for example small angle scattering, generation of secondary particles, and the break-up of nuclei by scattering on the material. The degree of detail to which the simulations are performed can be adjusted with a wealth of different options. Due to constraints put on by AnkeGeant4 (see section 5.5) the version that was used was restricted to 7.1.p01.

5.5 AnkeGeant4

AnkeGeant4 [74] serves as the implementation of the ANKE detector setup in the Geant4 framework. All the detector material and supporting structures are defined in its setup based on measurements performed after their installation. Therefore, geometric acceptance studies can be easily performed by writing an event selection which mimics the triggering scheme and the minimum requirements of the track finding algorithm. The output is a `TTree` containing the geometrically accepted particles' original Monte Carlo momenta generated by PLUTO. Naturally, its format is very different from that of the raw data and therefore can not be processed with the RootSorter/FdModule. Instead, the output must be processed by separate algorithms (see also section 5.7).

5.6 Additional tools

Of course there are many more tools and programs involved in writing the analyses and simulations than the aforementioned ones. These rarely get mentioned and it is next to impossible to cover them all. However, a few of them should be mentioned here as they heavily affected the code generation workflow and were essential to the creation of a team-based, beginner-friendly development framework.

5.6.1 Eclipse

As an integrated development environment (IDE), Eclipse [75] easily had the most immediate impact on the development process. Its slightly higher entry barrier when compared to simple editors as gedit or emacs is quickly outweighed by the power of its many features intended to make the life of the programmer easier. Therefore, IDEs are commonly found as one of the standard tools in many commercial environments. While being originally designed for Java development[3], the combination of a flexible plugin architecture with its own, rich marketplace allows for heavy customisation and tailoring the platform to many different needs the user might have, including support for C/C++, various version control systems and even LaTeX. The built-in indexer enables code completion for any specified code files (*e.g.* ROOT's source code), significantly reducing the developer's reliance on external code references. Refactoring tools help to put the code into a clearer structure after prototyping and templates ranging from loop to class generation remove much of the programming overhead, putting the focus back on the development of actual features. While this author strongly encourages the use of IDEs where it is appropriate, Eclipse is hardly the only option. Alternatives may be found in CodeBlocks, Apple's Xcode and more, many of which are suitable based on personal needs and preferences.

5.6.2 Mercurial

When developing a software project as a team and potentially shipping it out to other users, a source control management system should be considered among the bare minimum of tools being used to support the development process. Subversion and Git are among the very popular options, but both follow very different paradigms. Subversion, quite similar to CVS, has a centralised client-server architecture. As a consequence, all changes made to the code are communicated directly to the server, which is also the only place holding the revision history of the project. Unfortunately, this kind of setup is rendered useless when the connection between the client and the server becomes unavailable. Distributed version control systems like Git on the other hand create a full copy of the repository on the client system. The user has access to all features locally and synchronise any changes with the server at a later time. However, in order to avoid major conflicts, it is up to the user to ensure that the local version and the version on the server are reasonably up to date with respect to each other.

Mercurial is a distributed version control system [76]. It is very scalable and has an easy to learn syntax for which it is often preferred over Git. In our group it was connected to a lightweight nginx webserver by a FastCGI process. Access to the repository was granted

---

[3] As a matter of fact, Eclipse is written in Java.

through the secure hypertext transfer protocol (HTTPS). Included in the software package is also a web interface for browsing the revision history and viewing the source code.

5.6.3 Mantis

Issue trackers are powerful and fairly standard tools in order to provide an efficient and streamlined point of communication for team-based software projects. Issues can range from bug reports to feature requests. The mantis bug tracker [77] is a lightweight PHP-based system, which integrates well with an nginx webserver by FastCGI (see also section 5.6.2). Issues can be submitted and discussed through a web interface and assigned to specific developers. Beyond that, milestones can be defined as a set of certain issues which need to be fulfilled. A project history as well as a roadmap are automatically generated.

5.6.4 CMake

Among the tools mentioned here a Makefile generator might seem somewhat insignificant at first. However, it quickly gains importance when it comes to using good programming practices and teaching these to development newcomers. ROOT provides the option to create so-called macros, which can be either interpreted in a similar way as a shell script or converted into binary form by ROOT's own compiler. These are very convenient for quick prototyping. However, experience has shown that they also encourage some bad programming practices often leading to the code losing structure. Any somewhat larger project should therefore be semantically broken down into classes handling particular tasks. The compilation the potentially many different source code files and linking of the resulting object files is commonly steered by a Makefile. These, however, are rarely written by hand as this can become a very tedious process. As a Makefile generator, CMake [78] stands out for its human-readable syntax and scalability and in turn has gained in popularity in recent years. Some of the projects well known within the particle physics community having adopted CMake are KDE and ROOT. Making things even more convenient, plugins for Eclipse enabling syntax highlighting and code completion are available.

5.7 Reconstruction

The central idea driving the creation of the *Reconstruction* framework was to enhance the accessibility of the analysis for beginner level students.
As a rough benchmark, the software was supposed to be so easy to use that complex analysis tasks could be performed within the short time given for a bachelor thesis. In order to achieve that goal, it was essential to significantly cut down the average development time for analysis code. A comprehensive, but most probably not complete list of ways to move towards this goal includes:

1. Provide a clean and human-readable interface to reconstructed quantities, *e.g.* the momentum vectors of particle tracks.

2. Separate parts of code common to (almost) all analyses from parts that are specific to the task at hand. Common code parts are often related to basic necessities, *e.g.* executing the event loop and providing access to the data interface. These parts should be implemented in a centralised way and never be copied!

3. Provide a clean and clear structure for the analysis specific code to be implemented in.

4. Unify access to simulated Monte Carlo data and reconstructed experimental data.

5. Document everything.

Developing such a project is of course ambitious and its shape is constantly in motion. Therefore, the final product may vary substantially from the way it was originally conceived. In the early stages the *Reconstruction* was designed for use with ANKE's forward detection system. This scope was eventually extended to the full experimental setup. The following explanations refer to the state of the *Reconstruction* after its redesign which introduced data access to the positive and negative detection systems [64]. In a similar way, many of the simulation related components were added over the course of the analysis on the η-meson mass, which heavily relied on understanding the involved kinematics [49]. The spectator detector was only implemented much later when the Münster group performed a beam time involving this detector [40].
While it seems that item 1 can be addressed in a fairly straightforward way, readability is often omitted in favour of rather compressed naming conventions. This creates a significant entry barrier for newcomers to the analysis, which is even further enhanced by the lack of inline comments and documentation of analysis code. One of the pillars of the *Reconstruction* is an overlay for the data accessors which is easy to read and can be understood in an intuitive way. Consider the following example:

```
objectPointer->p();
```

Listing 5.1: Example for a bad naming convention.

In this case, the object referenced by `objectPointer` is assumed to be basically any kind of container for an event, a track or a detector group. The called method `p()`, however, is quite ambivalent. Looking up its type (*e.g.* a `Double_t` or `TLorentzVector`) might give the user a clue about its purpose, but it still leaves a lot of room for interpretation. Does `p()` refer to a general particle, a proton or maybe a momentum? Is it a getter or a setter? None of these possibilities are uncommon and figuring out the meaning behind unclear naming schemes amounts to a lot of wasted time on the side of the user. This a serious problem with a rather simple solution.

```
objectPointer->getProton();
objectPointer->setProton(proton);
```

Listing 5.2: Example for a clear naming convention.

The methods called in listing 5.2 are much clearer in their purpose. The name suggests that the accessed data object represents a proton. The preceding `get` and `set` distinguish between retrieval and modification of the data, respectively. Since they are of the type `TLorentzVector` it is obvious that they handle access to the four-momentum vector of the proton. A rather simple solution to this issue presents itself by introducing and enforcing common coding conventions every contributor needs to adhere to. For the *Reconstruction* and most analyses based on it the *Google C++ Style Guide* [79] served as a basis with a few additions and exceptions agreed upon by all the contributors during the early stages of development. An example for such an exception is to forgo the 80 character line limit, which basically became obsolete with the cheap availability of widescreen monitors, and little tweaks to various naming conventions. However, the central idea behind all conventions was to enhance the readability of the written code and ideally have it understandable with even very basic programming skills.

5.7.1 General structure

The contents of the *Reconstruction* can be grouped into three different parts based on their specific purpose. A system of several event classes serves as an interface to the data from the various detector groups which have been stored during the pre-analysis phase. The interface to the user is provided by the analysis modules, which serve as a place to implement most analysis routines which go beyond just reading in the data. It is up to the developer to semantically structure their code, *e.g.* by individual reactions. The event loop and communication between the different classes is handled by the "MainAnalysis", making heavy use of the possibilities provided by class inheritance.

Event classes

The pre-analysis based on the RootSorter provides data stored in ROOT's `TTree` format. It is the job of the event classes to provide access to these data and perform some basic procedures like boosting momentum vectors into the center of mass frame. A few examples of the accessible data include energy losses in the hodoscopes, hit positions in the wire chambers and `TLorentzVector`s reconstructed from the momenta determined by the FdModule. In the latter case, the masses for the respective particles are assumed based on the subject of the analysis. It should be noted that no particle identification procedures are implemented here and it is left to the user to use the proper particle accessors.

Figure 5.2 shows the inheritance diagram of the event classes. The abstract class "BaseEvent" is found at the top and is essential to enable communication between any given event class and analysis module and also from one event class to another. A certain structure is already provided here which is common to most detector groups, *e.g.* accessors for different `TLorentzVector`s and a method to discard an event. Furthermore, several methods for determining different kinds of data are declared as purely virtual and must be implemented in the derived classes (see listing 5.3).

```
virtual void determineLorentzVectors() = 0;
```

Listing 5.3: Example for a purely virtual method.

On the next level of hierarchy events specific to the detector groups described in section 4.2 are derived from the "BaseEvent" class, with the following types of events being implemented:

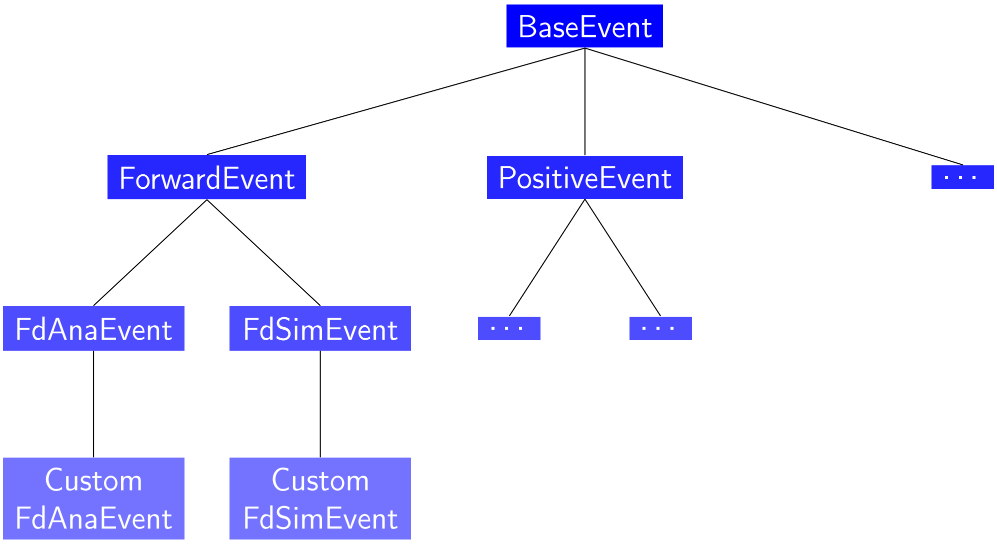

Figure 5.2: Inheritance diagram of the *Reconstruction*'s event classes. At the top the abstract base class "BaseEvent" can be found, which all event classes have to be subsequently derived from. On the second level the events are defined respective to their detector counterparts, then specialised for either real or simulated data and finally the user can derive their own specialised class if desired.

- ForwardEvent - provides access to data from the forward detection system.
- PositiveEvent - provides access to data from the positive detection system.
- NegativeEvent - provides access to data from the negative detection system.
- SpectatorEvent - provides access to data from the silicon tracking telescopes.
- CosyEvent - provides access to data passed on from the COSY accelerator.
- MunsterEvent - contains information beyond the standard data stored by the RootSorter.

As much of the events functionality as possible is supposed to be implemented at this stage. Unfortunately, the structure and types of data stored by AnkeGeant4 and the RootSorter are very different. Therefore, another level of hierarchy had to be introduced in order to specialise the events for either analysis or simulations, *e.g.* FdAnaEvent and FdSimEvent. The final inheritance level in fig. 5.2, the so-called custom events, is entirely optional. It illustrates the possibility for the user to derive their own event classes and adapt them even further to the special needs determined by the respective measurement. In the case of this work, several custom events have been implemented to provide access to COSY cycle timing, polarisation bits and specialised methods to discard an event or track based on different cut conditions.

Analysis modules

The analysis modules are the place for the user to implement their analysis routines. Similar to event classes, the abstract class "BaseAnalysisModule" can be found here.

However, there is no complex inheritance structure as the user derives their own modules directly from the "BaseAnalysisModule". The base class defines a basic structure by declaring a few purely virtual methods (see listing 5.4) which all derived modules have to follow. These methods are called by the MainAnalysis and serve the following respective

```
virtual void startProcessing() = 0;
virtual void processCut() = 0;
virtual void processEvent() = 0;
virtual void endProcessing() = 0;
```

Listing 5.4: Purely virtual methods declared in the BaseAnalysisModule

purposes:

- `startProcessing` - called before the event loop and suitable for initialising member variables such as histograms and establishing communication to event objects and other modules.
- `processCut` - called for each event and suitable for implementing cut conditions for discarding individual tracks or the whole event and store the cut decision in the event objects.
- `processEvent` - called for each event and used to perform analysis routines and fill histograms.
- `endProcessing` - called after the event loop and suitable for performing fits and storing histograms to file.

As mentioned earlier, how to structure the analysis across one or many modules is up to the user. Suitable options are to create a module for each reaction. On the other hand, more general modules *e.g.* for time of flight studies are well suited to perform cuts on these observables. As a matter of fact, the analysis for this work contained a module for the $\vec{\mathrm{d}} + \mathrm{p} \rightarrow {}^3\mathrm{He} + \eta$ reaction and another one for the $\mathrm{d} + \mathrm{p} \rightarrow \{\mathrm{pp}\}_s + \mathrm{n}$ reaction as well as several of the aforementioned more general modules.

MainAnalysis

The "MainAnalysis" could be considered the beating heart of the *Reconstruction*. First, the pointers to all event objects and analysis modules have to be passed to the "MainAnalysis". Since all events are derived from a base class which is part of the *Reconstruction*, their pointers can be passed to all other objects as the type of their respective base class without the need of being a part of the software package. Therefore, the *Reconstruction* only needs to be compiled once and not every time a change is made to the analysis. Since these pointers retain their initial identity, they can be re-cast to their original form within the custom event classes or analysis modules as illustrated by the method in listing 5.5. The program loops over the complete list of event pointer that have been passed on, performing a `dynamic_cast` on each one. If the object is of the wrong type, the

```
void PolRampFdAnaEvent::castEvent() {
  for (int iEvent = 0; iEvent < eventList.size(); ++iEvent) {
    if (!polRampCosyAnaEvent) polRampCosyAnaEvent =
         dynamic_cast<PolRampCosyAnaEvent*>(eventList.at(iEvent));
    }
}
```

Listing 5.5: Example for casting a BaseEvent pointer back to its original form.

`dynamic_cast` fails and returns a pointer to `NULL`. This feature is used in this example as a security check.
The “MainAnalysis” then proceeds to call the methods of the analysis modules as specified above. After the event loop, the output file containing the histograms is written to disk.

The *Reconstruction* comes with examples for both analysis and simulation. These are designed in a way that they highlight its main features and can serve as template for a new user. A comprehensive documentation, including a software diary, was maintained by the developers as a collaborative document and made available to all users.

5.8 Summary of software related efforts

In the process of developing the analysis tools needed for this work, the *Reconstruction* was first conceived as framework simplifying access to the data both from the experiment and simulations, and as a basis for writing highly maintainable analysis code. Its potential for the whole ANKE analysis group in Münster was quickly discovered. A first milestone was met by this author, when the forward detection system was fully integrated. At that point, additional developers, namely Malte Mielke and Paul Goslawski, were introduced to the project in order to continue the development on additional detector groups and simulations based on the structure that had already been established. Later, components for the spectator detector were added by Daniel Schröer. To enhance the development process turn the *Reconstruction* into an actual team-based project, additional tools (see section 5.6) were introduced. These were adopted quickly and have become a standard within the group. As a result, the scope of analyses that could be done within a limited time frame was significantly expanded while the time overhead associated with the supervision of newly beginning students was reduced. At the time of this writing, all of the analyses that were started in parallel to this work or afterwards were based on the *Reconstruction* framework [49, 64, 80, 40, 81, 82, 83, 84], with several more currently in progress.

Chapter 6

Polarisation measurement

To be able to measure the analysing powers of the reaction of interest, first the polarisation of the deuteron beam has to be determined. The idea is simple: one or more reactions with known analysing powers, either vector or tensor, are taken as a reference and investigated within the same data set. A previous measurement with the ANKE detector and a polarised deuteron beam successfully made use of this method before [52], taking the reactions $\vec{\mathrm{d}} + \mathrm{p} \rightarrow {}^3\mathrm{He} + \pi^0$, quasi-free $\mathrm{n} + \mathrm{p} \rightarrow \mathrm{d} + \pi^0$, and deuteron-proton elastic scattering as references. As already indicated in section 4.3, a beam cycle with the fixed momentum $p_\mathrm{d} = 2.435\,\mathrm{GeV}/c$ was set up for the very same purpose. However, it was also mentioned that a setup with a joint cycle for the fixed momentum and the continuous ramp intended for measurement of the $\vec{\mathrm{d}} + \mathrm{p} \rightarrow {}^3\mathrm{He} + \eta$ reaction could not be realised, thus creating separate data sets for polarimetry and the measurement of the analysing powers. During a later stage of the analysis, new measurements on the two deuteron tensor analysing powers A_{xx} and A_{yy} on the $\vec{\mathrm{d}} + \mathrm{p} \rightarrow \{\mathrm{pp}\}_s + \mathrm{n}$ reaction were determined at higher beam energies [85]. These made predictions of the analysing powers based on the impulse approximation model [86] possible at the energies investigated within the continuous ramp [87]. In the original proposal for this measurement it was suggested to measure the polarisation at a low momentum before and after the ramp, but within the same cycle (see fig. 4.6) [47]. Thereby, systematic effects on the beam polarisation, *e.g.* and unexpected loss of polarisation during acceleration to the higher momenta, could be studied. However, as described in section 4.3.1 this setting could not be realised. Measuring the polarisation directly in the continuous ramp, on the other hand, presented an even more advantageous opportunity. This way, these possible systematic effects could be avoided altogether, yet still leaving the separate low momentum data to check for consistency of the results.

6.1 Polarisations by LEP

As a control mechanism to verify the quality of operation of the polarised ion source, a Low Energy Polarimeter (LEP) was employed, which is installed in the injection beam line to COSY [88]. It consists of an ultra high vacuum chamber with eight flanges covered by thin stainless steel foils. A movable target frame equipped with viewers allows for adjustment to the beam position, and a carbon target is used for the polarimetry measurements. The elastic deuteron-carbon scattering is sensitive to the vector polarisation, resulting in a

left-right asymmetry of the ejectiles with respect to the spin quantisation axis. Detectors can be placed at the azimuthal angles $\phi = 0°, 90°, 180°$, and $270°$ in the polar angle ranges of $25° - 70°$ and $110° - 155°$. The detection and identification of the ejectiles is done via NaI scintillators connected to photomultipliers.
The LEP is operated at injection energy for COSY, *i.e.* $T_\mathrm{d} = 75.6\,\mathrm{MeV}$ (or $p_\mathrm{d} = 0.539\,\mathrm{GeV}/c$). The values for the vector polarisation were determined and provided by the ion source operator once in the beginning of the beam time an can be found in table 6.1.

Table 6.1: Nominal values of the vector polarisations of the deuterons provided by the ion source. Also shown are the values obtained with the LEP and there statistical errors, which were obtained at the injection energy of 75.6 MeV for a sample of deuterons.

Mode	$p_Z^{\mathbf{ideal}}$	$p_Z^{\mathbf{LEP}}$
1	$+1/3$	$+0.244 \pm 0.032$
2	-1	-0.707 ± 0.026
3	$+1$	$+0.601 \pm 0.027$

The obtained values for modes 1 and 2 both lie within 70% of the nominal values, which is a solid efficiency of the ion source under beam time conditions. It was acknowledged at the time of the measurement that the efficiency of mode 3 was a little lower at approximately 60% of its nominal value. However, it was still reasonably close to the performance of the ion source at an earlier measurement [89]. It was estimated that the goals of the beam time could be achieved with these efficiencies and in conjunction with the time constraints illustrated in section 4.3.3, a further development of the ion source was not warranted.

6.2 Polarisations by the reaction $\vec{\mathrm{d}} + \mathrm{p} \to \{\mathrm{pp}\}_s + \mathrm{n}$

As mentioned in the introduction to this chapter, recent measurements of the two tensor analysing powers A_{xx} and A_{yy} for the charge-exchange reaction $\vec{\mathrm{d}} + \mathrm{p} \to \{\mathrm{pp}\}_s + \mathrm{n}$ [85] opened up the possibility of determining the tensor polarisation of the deuteron beam within the continuous ramp, *i.e.* the very same data used for the investigations on the $\vec{\mathrm{d}} + \mathrm{p} \to {}^3\mathrm{He} + \eta$ reaction. Since at this point the low momentum data at $p_\mathrm{d} = 2.435\,\mathrm{GeV}/c$ had already been investigated, they were used to verify the consistency of the polarisation results. However, for the final results, only the polarisation values extracted from the continuous ramp were retained in order avoid systematic effects as much as possible. Furthermore, since the change of the beam energy within the continuous ramp is very small when compared to its absolute value, all data from the ramp could be combined for the polarisation studies. This was done for all of the pictures presented in this section.

6.2.1 Event identification

Events for the $\vec{\mathrm{d}} + \mathrm{p} \to \{\mathrm{pp}\}_s + \mathrm{n}$ reaction were collected with the T2 trigger, which was unaffected by the problems with the hodoscope module mentioned in section 4.3.3. In this reaction, the neutron located in the incident deuteron exchanges its charge with the target proton. The momentum transfer is very small and the charged ejectiles' momenta are still very close to the beam momentum per nucleon. To still be classified as a diproton, the two protons ejectiles have to be in relative s-wave with a very low relative energy of $E_{\mathrm{pp}} < 3\,\mathrm{MeV}$. Therefore, the particle trajectories are very close to each other in the laboratory frame and the most efficient way of detecting these events is by selecting events with two tracks in the forward detection system. A picture of the missing mass of the $\mathrm{d} + \mathrm{p} \to \{\mathrm{pp}\}_s + \mathrm{X}$ reaction is shown in fig. 6.1. A peak at the neutron mass is clearly visible. However, it rests on a substantial background. On the right hand side of the picture some contributions are visible which likely involve the production of a π^0.

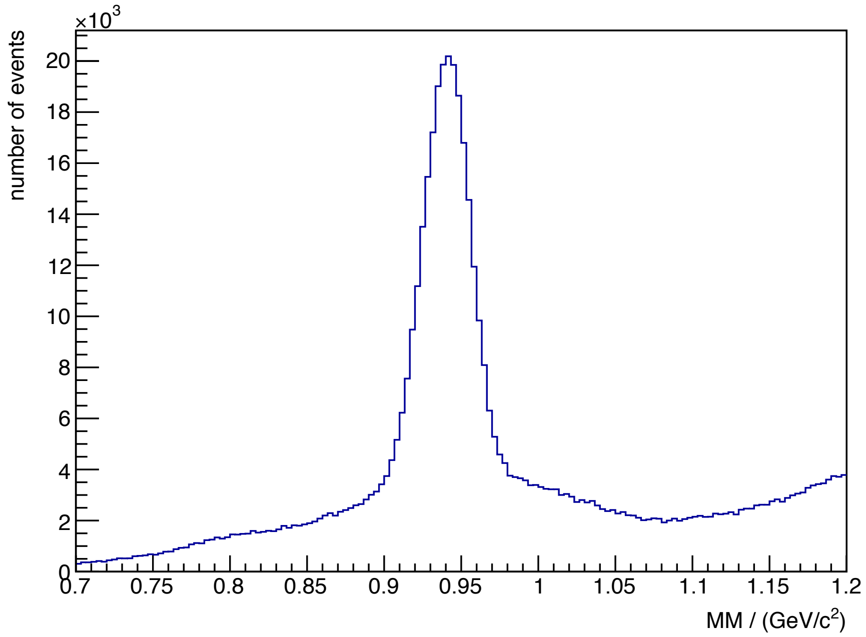

Figure 6.1: The missing mass distribution for events with two tracks detected in the forward detection system. No further cuts have been applied. The data shown were combined for all polarisation states.

When trimming the background, the relative time of flight between the two ejectiles provides some leverage. Figure 6.2 shows the difference of the time of flight between the two ejectiles, measured versus calculated. The measured values were obtained by extracting the averaged time stamps of the two tracks from the first two layers of the scintillation hodoscope and calculating the difference. The calculated time difference was derived from the particles' momenta, taking into account the path length from the vertex point to the hodoscope. All events with two protons in the final state end up on the diagonal. However, further structures present themselves above an below the diagonal. These arise from the reaction $\mathrm{d} + \mathrm{p} \to \mathrm{d} + \mathrm{p} + \pi^0$, when either both charged ejectiles have been identified correctly or misidentified for each other, respectively[1]. The split into

---

[1] Note that the events above and below the diagonal are essentially mirrored. The only difference is whether the particle to arrive first or second in the hodoscope was the misidentified deuteron, thus resulting in a different sign for the measured time of flight.

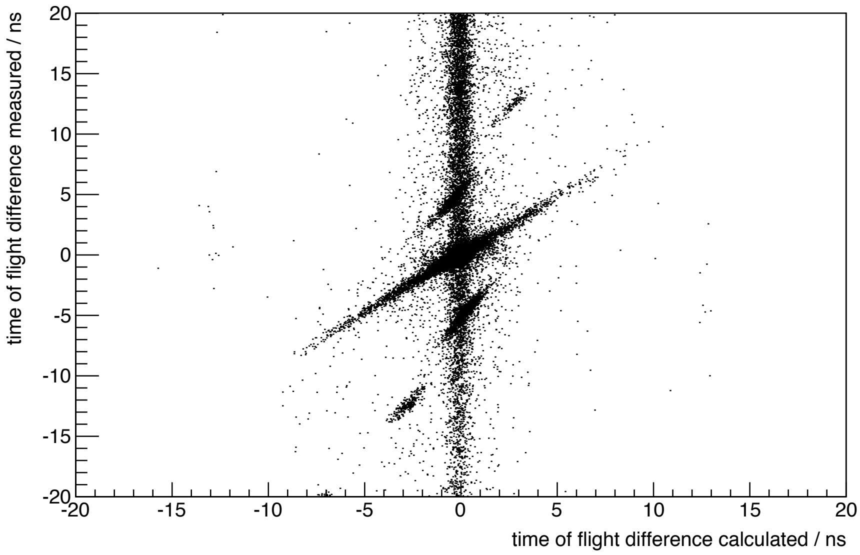

Figure 6.2: The time of flight difference of the two ejectiles. The values measured with the first two layers of the scintillation hodoscopes are plotted against the values calculated from the track momenta. Events with two protons in the final state are located on the diagonal, whereas the four structures above and below the diagonal arise from the $\mathrm{d} + \mathrm{p} \to \mathrm{d} + \mathrm{p} + \pi^0$ reaction with either a fast or a slow deuteron, respectively.

two branches, however, results from not having a full geometrical acceptance for that reaction in the forward detection system and detecting either a slow or a fast deuteron. A selection criterion designed to cut away these unwanted reactions like

$$|(\Delta t)_{\text{measured}} - (\Delta t)_{\text{calculated}}| < 0.8\,\text{ns} \tag{6.2.1}$$

would already drastically reduce the background. The result of this cut can be seen in fig. 6.3. The background below the neutron peak is already negligible. It is noteworthy that also the signal peak is reduced substantially, indicating that the vertical structure in fig. 6.2 contains many events from the deuteron breakup reaction. However, this is by no means an exclusive selection of the $\vec{\mathrm{d}} + \mathrm{p} \to \{\mathrm{pp}\}_s + \mathrm{n}$ reaction. A better result can be achieved by replacing the cut on the time of flight with the aforementioned cut on the relative energy of the protons,

$$E_{\text{pp}} < 3\,\text{MeV}, \tag{6.2.2}$$

leading to the result shown in fig. 6.4. Here, only the cut on the relative energy has been applied. This is needed as a base requirement for identifying the $\vec{\mathrm{d}} + \mathrm{p} \to \{\mathrm{pp}\}_s + \mathrm{n}$ reaction and imposes a very strict kinematic constraints. Selecting such a narrow energy window also restricts the range of the momentum difference between the two final state protons. This directly constrains the time of flight difference as well, making the previous time of flight cut obsolete and it expectedly reduces the events shown in fig. 6.2 to the ones located very close to the centre.

For the sake of extracting the number of events, a Gaussian was fitted to the neutron peak and all events outside a 3σ environment were cut away. The fit was only calculated once for for all polarisation modes combined and then applied to the individual polarisation

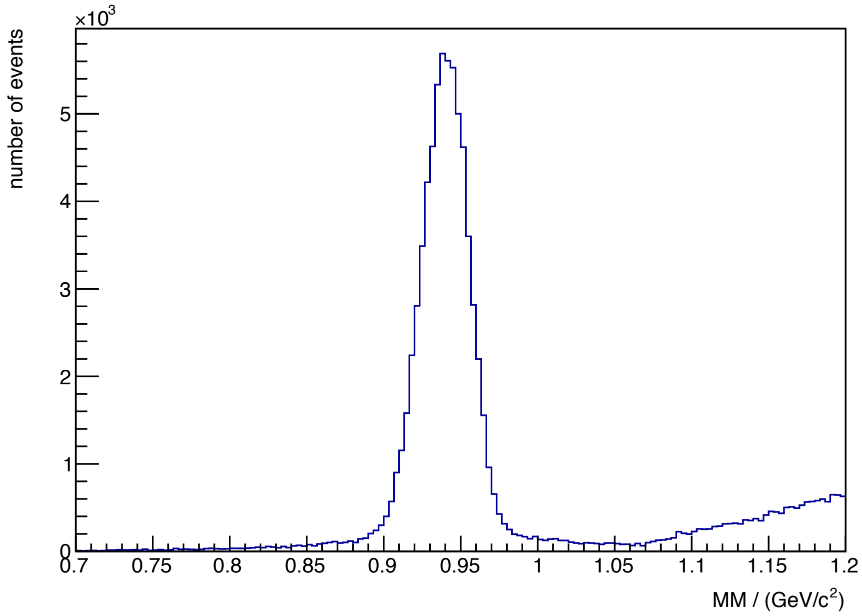

Figure 6.3: The missing mass distribution for events with two tracks detected in the forward detection system. An additional cut on the time of flight difference as given in eq. (6.2.1) was applied. The data shown were combined for all polarisation states.

states. This method cancels out systematic effects, *e.g.* arising from having individual selection criteria for each polarisation state, when calculating the polarisation values (see section 6.2.3).

6.2.2 Data normalisation

While many systematic effects cancel out when calculating the polarisation through comparison of polarised and unpolarised cross sections, conditions affecting each individual events in a different way were implemented as an event weight.
A momentum calibration was performed using the positions and angles of the wire chambers relative to the COSY coordinate system as free parameters within their respective uncertainties. For this purpose, the missing mass spectra of several reactions were used to optimise the settings: the elastic scattering of deuteron and proton with either one or two tracks hitting the forward detection system, the break-up reaction $\mathrm{d}+\mathrm{p} \rightarrow \mathrm{p}+\mathrm{p}+\mathrm{n}$, and the $\mathrm{d}+\mathrm{p} \rightarrow \mathrm{d}+\mathrm{p}+\pi^0$ reaction with both the deuteron and proton ejectiles registered in the forward detection system [90]. It was found that the proton missing mass of the elastic scattering with only the fast deuteron in the forward detection system was shifting by approximately $4\,\mathrm{MeV}/c^2$ over the course of the continuous ramp cycle. A shift of the x-coordinate of the vertex by $0.33\,\mathrm{mm}$ explained this effect well. This indicates a change in the orbit of the deuteron beam, which, however, is still very well within the boundaries of the cluster-jet target. For the calibration, this effect was taken into account.
The efficiencies of the MWPCs were calculated by checking whether or not for a given track all wire planes had produced a hit. Even if the hit information from one of the wires is missing, the track can still be reconstructed, since only information sufficient to form a

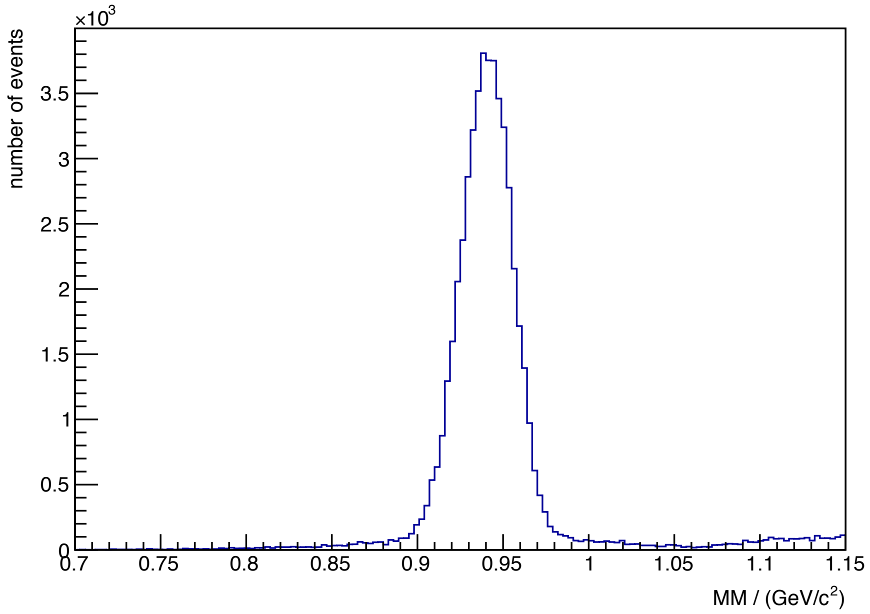

Figure 6.4: The missing mass distribution for events with two tracks detected in the forward detection system. An additional cut on the relative energy of the two tracks with $E_{\text{pp}} < 3\,\text{MeV}$ was applied. The data shown were combined for all polarisation states.

straight line is required. The wire planes were divided into $20 \cdot 20$ squares and efficiency maps are generated within the FdModule (see section 5.2.1). The efficiency maps were found to be flat with values usually above 97% per square. The track reconstruction efficiency was estimated to even be over 99%.
The dead time factor τ of the data acquisition system could be estimated by information collected in the scaler events (see section 4.3.2). These contained the number of events per second[2] activating the individual triggers N_{in} and events per trigger actually written to disk N_{out}. The dead time factor was calculated as

$$\tau = 1 - \frac{N_{out}}{N_{in}}. \tag{6.2.3}$$

In addition to these event weights, the relative luminosity between the polarisation modes had to be estimated. While this could be achieved by using the beam current signal, the most precise measurement is done by counting the numbers of spectator protons from the $\text{d} + \text{p} \to \text{p}_{\text{spec}} + \text{X}$ reaction. Since these spectator protons originate from the beam, they have a strong forward boost and would be outside the acceptance of the spectator detector, had it been installed (see also 4.2.3). Instead, they are registered in the forward detection system, thereby not adding to the complexity of the experimental set-up nor introducing any additional systematic effects. For this analysis, a cut on the Fermi momentum $p_{\text{spec}} \leq 60\,\text{MeV}/c$ was employed. A plot of these events against the Fermi momentum is shown in fig. 6.5. This procedure was investigated for previous polarised measurements at ANKE [85, 91] and found to be unaffected by the polarisation of the

---

[2] Note that these numbers were updated with the frequency of the scaler trigger, *i.e.* 10 Hz. However, the numbers stored were a floating average over 1 s.

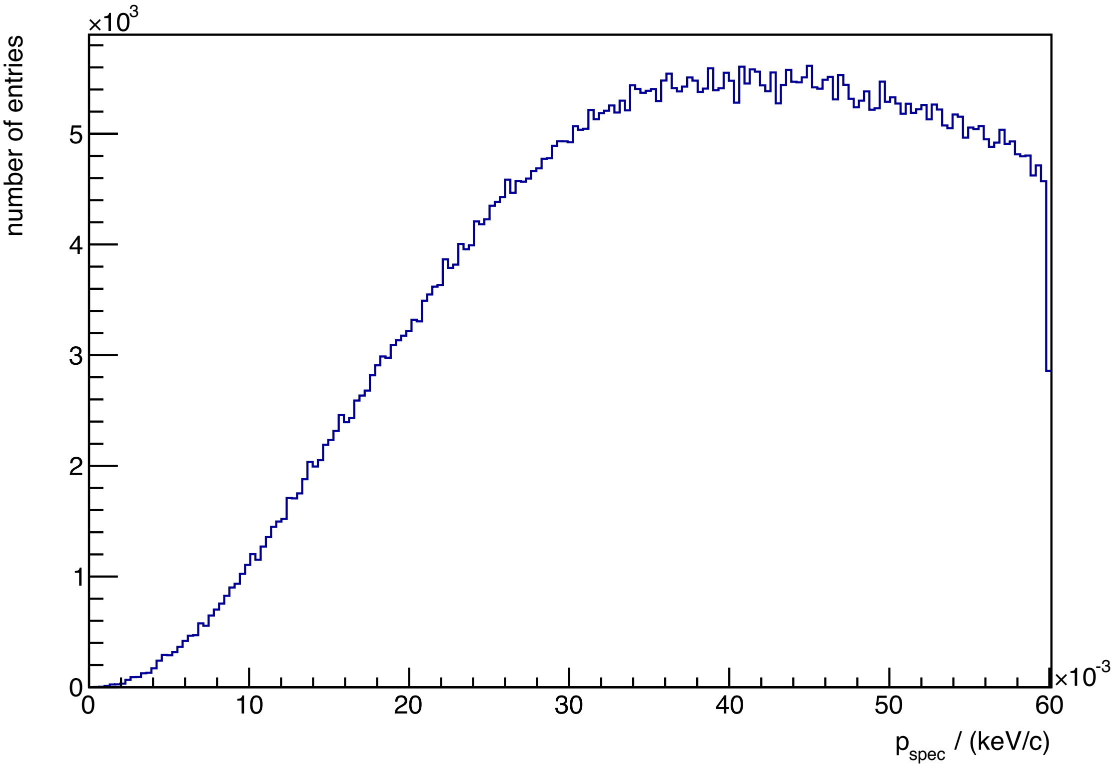

Figure 6.5: Events of the $\mathrm{d} + \mathrm{p} \rightarrow \mathrm{p}_{\mathrm{spec}} + \mathrm{X}$ reaction plotted against the momentum of the spectator proton p_{spec}. For the purpose of the analysis, the distribution has been cut off at $p_{\mathrm{spec}} \leq 60\,\mathrm{MeV}/c$. More details are given in the text.

deuteron beam [92]. As a verification, this cut was reduced to $p_{\mathrm{spec}} \leq 40\,\mathrm{MeV}/c$. No notable change in the values of the relative luminosities could be observed.

6.2.3 Extracting the tensor polarisation

Utilising the fact that the $\mathrm{d} + \mathrm{p} \rightarrow \{\mathrm{pp}\}_s + \mathrm{n}$ reaction is insensitive to the beam's vector polarisation for small E_{pp} [86], the tensor polarisation can be written in terms of the differential cross sections and the two tensor analysing powers by rearranging eq. (3.1.10). It becomes clear, however, that contributions to the differential cross section such as an absolute normalisation cancel out if the relative normalisation between the numbers of polarised and unpolarised events is known. By not having to take into account an absolute normalisation, which usually depends on the cross section knowledge of yet another reaction, the precision of the extracted polarisation values can be greatly improved. In compliance with the methodology used in [85], the numbers of diprotons from polarised ($N^{\uparrow}(q, \phi)$) and unpolarised data ($N^{0}(q, \phi)$) were grouped into bins of the momentum transfer q of the incident deuteron on the final state diproton and the azimuthal angle ϕ

to be fitted by

$$\begin{aligned}\frac{N^{\uparrow}(q,\phi)}{N^{0}(q,\phi)} = C_n\{1 &+ \frac{1}{4}p_{ZZ}[A_{xx}(q)(1-\cos 2\phi)] \\ &+ A_{yy}(q)(1+\cos 2\phi)]\}. \end{aligned} \tag{6.2.4}$$

The relative normalisation factor C_n was determined as it was described in section 6.2.2 and assumes values of $C_n \approx 0.7$. Approximately 10000 to 13000 $\mathrm{d}+\mathrm{p} \to \{\mathrm{pp}\}_s + \mathrm{n}$ events were collected per polarisation mode.

Table 6.2: Nominal values of the tensor polarisations of the deuterons provided by the ion source. Also shown are the values obtained by studying the $\vec{\mathrm{d}} + \mathrm{p} \to \{\mathrm{pp}\}_s + \mathrm{n}$ reaction with ANKE.

Mode	$p_{ZZ}^{\mathbf{ideal}}$	$p_{ZZ}^{\mathbf{ANKE}}$
1	-1	-0.62 ± 0.05
2	+1	$+0.67 \pm 0.05$
3	+1	$+0.22 \pm 0.05$

The polarisation values derived by this method are given in table 6.2. For modes 1 and 2, the extracted tensor polarisations are $\gtrsim 60\%$ of the nominal values. This is consistent with previous measurements at COSY with the same polarised ion source [66], albeit at a lower beam momentum of 1.042 GeV/c. However, no depolarisation during the further acceleration is expected as the first depolarising resonances for deuterons at COSY in the possible beam momentum range [51]. Mode 3, however, has a lower polarisation by a factor of three when compared to the other modes. Apparently, for this mode the ion source was not working as intended. The consequences of this result will be discussed further in section 6.3.

6.3 Summarising the results

Values for the vector and tensor polarisations have been determined by means of the low energy polarimeter and by studying the $\vec{\mathrm{d}} + \mathrm{p} \to \{\mathrm{pp}\}_s + \mathrm{n}$ reaction, respectively. The results are presented again in table 6.3. The former were measured at the injection energy 75.6 MeV. In a previous experiment the vector polarisations were determined both with the low energy polarimeter and after acceleration to 1.042 GeV/c with only minor differences between the measured values [66]. Although the deuterons do not tend to lose any polarisation through the acceleration process in COSY, no guarantee for complete stability of the ion source throughout the whole experiment can be given.

Unfortunately, the analysis revealed the tensor polarisation of mode 3 being only a third of the polarisation of mode 2. Since the analysing powers are linearly related to the polarisation, the factor of three would also be reflected in the propagated uncertainties of the analysing powers. For the sake of comparison, this would be the equivalent of the amount of statistics being reduced by approximately one order of magnitude. After careful consideration, it was concluded that these data would not be beneficial to the investigations on the $\vec{\mathrm{d}} + \mathrm{p} \to {}^3\mathrm{He} + \eta$ reaction, but rather might introduce unknown

Table 6.3: Nominal values of the tensor polarisations of the deuterons provided by the ion source. Also shown are the values obtained by studying the $\vec{\mathrm{d}} + \mathrm{p} \to \{\mathrm{pp}\}_s + \mathrm{n}$ reaction with ANKE.

Mode	$p_Z^{\mathbf{ideal}}$	$p_Z^{\mathbf{LEP}}$	$p_{ZZ}^{\mathbf{ideal}}$	$p_{ZZ}^{\mathbf{ANKE}}$
1	$+1/3$	$+0.244 \pm 0.032$	-1	-0.62 ± 0.05
2	-1	-0.707 ± 0.026	$+1$	$+0.67 \pm 0.05$
3	$+1$	$+0.601 \pm 0.027$	$+1$	$+0.22 \pm 0.05$

systematic effects which could not be estimated. Clearly, one or more of the hyperfine transitions were not working as intended. For these reasons, mode 3 was discarded for the following analysis steps.

Chapter 7

Analysis of $\vec{\mathrm{d}} + \mathrm{p} \to {}^3\mathrm{He} + \eta$

Extracting the tensor analysing power T_{20} from the data for the $\vec{\mathrm{d}} + \mathrm{p} \to {}^3\mathrm{He} + \eta$ reaction follows very much the same scheme that was already used in section 6.2. However, this time the previously determined polarisations are used in order to calculate the analysing powers, not the other way around. Before that can happen, the events have to be identified and normalised first, so that the ratios of the polarised and unpolarised number of events can be determined.

In contrast to the $\vec{\mathrm{d}} + \mathrm{p} \to \{\mathrm{pp}\}_s + \mathrm{n}$ reaction, the background for $\vec{\mathrm{d}} + \mathrm{p} \to {}^3\mathrm{He} + \eta$ cannot be reduced completely by cuts on the data and has to be considered differently. A method using data taken below the reaction's production threshold, that had already been successfully used for an earlier investigation on unpolarised data [65] in a very similar way, was slightly for this measurement and will be described in more detail in section 7.3. Using the relations between the analysing powers in Cartesian and spherical coordinates which have been defined according to the Madison convention [46],

$$iT_{11} = \frac{\sqrt{3}}{2} A_y \tag{7.0.1}$$

$$T_{20} = \frac{1}{\sqrt{2}} A_{zz} \tag{7.0.2}$$

$$T_{22} = \frac{1}{2\sqrt{3}} (A_{xx} - A_{yy}), \tag{7.0.3}$$

eq. (3.1.4) can be written in terms of these spherical analysing powers:

$$\frac{N^{\uparrow}(\theta,\phi)}{N^{0}(\theta,\phi)} = C_n \left(1 + \sqrt{3} p_Z iT_{11}(\theta)\cos\phi - \frac{1}{2} p_{ZZ}\left[\frac{1}{\sqrt{2}} T_{20}(\theta) + \sqrt{3} T_{22}(\theta)\cos 2\phi\right]\right). \tag{7.0.4}$$

Note that here the ratio of the differential cross sections was already replaced by the ratio of the number of events in conjunction with the relative normalisation factor C_n (see also section 6.2.3). The experimental setup was chosen in a way that it would provide a full angular acceptance in both θ and ϕ throughout the whole continuous ramp. When integrating over the full phase space, the terms for iT_{11} and T_{22} in eq. (7.0.4) become zero, reducing it to:

$$\frac{N^{\uparrow}(\theta)}{N^{0}(\theta)} = C_n \left(1 - p_{ZZ} \frac{1}{2\sqrt{2}} T_{20}(\theta)\right). \tag{7.0.5}$$

Equation (7.0.5) illustrates how desirable a full acceptance for the measurement is as it completely negates the effects from all analysing powers except the one of interest. However, due to the issues with one of the hodoscope modules mentioned in section 4.3.3 the original concept for this measurement could not be realised. A full acceptance was not given for all energies, and since the analysing powers iT_{11} and T_{22} were neither known nor could they be measured independently[1], the feasibility of this analysis had to be re-evaluated. The analysis scheme had to be carefully revised in order to optimise the physics output from these data.

7.1 Event identification

Events of the $\vec{\mathrm{d}} + \mathrm{p} \rightarrow {}^3\mathrm{He} + \eta$ reaction were collection with the main trigger T1. Following the trigger scheme explained in section 4.3.2, this trigger would activate whenever a ^{3}He track would create a hit signature with a sufficiently high energy loss in the forward detections system's hodoscope layers. By this hardware selection alone, the background contributions from fast protons and deuterons was already reduced substantially. The basic idea can be taken further by combining the information on the deposited energy with the momenta obtained from the reconstructed tracks during the pre-analysis phase [2].

The population of a singular module's ADC channels, which are proportional to the energy deposited by the charged particle while passing through the scintillator, are plotted against the reconstructed track's momentum in the laboratory system in fig. 7.1.

Several features of fig. 7.1 need to be explained. First, events from $\vec{\mathrm{d}} + \mathrm{p} \rightarrow {}^3\mathrm{He} + \eta$ are concentrated at a laboratory momentum around $p \approx 2.7\,\mathrm{GeV}/c$. They are part of band created by ^{3}He ejectiles produced in the $\mathrm{d} + \mathrm{p} \rightarrow {}^3\mathrm{He} + \pi^0$ and $\mathrm{d} + \mathrm{p} \rightarrow {}^3\mathrm{He} + (\pi + \pi)^0$ reactions. The background towards higher momenta, however, is dominated by protons mainly coming from the breakup reaction $\mathrm{d} + \mathrm{p} \rightarrow \mathrm{p} + \mathrm{p} + \mathrm{n}$. Despite the implemented hardware trigger, events from this reaction might still be registered with a high energy loss due to the long slope of the Landau distribution which the deposited energy follows. While the chance of this happening might be rather small, the sheer amount of events from this reaction still leads to a considerable background.

Two selection criteria were applied in the creation of fig. 7.1. A hard selection was made on the ADC channels between 330 and 500. In this context, "hard" means that the track was passing through several hodoscope layers and had to fulfil a similar requirement in each one. While the values for this selection were derived from fig. 7.1 in order to make sure not to cut into the main reaction, for the repeated pre-analysis it was later implemented before the actual event reconstruction. This reduced the average runtime of the pre-analysis by a factor of $5 - 10$, trimming it down to approximately two weeks for the whole data set during the early phase of this work. Afterwards, a soft selection

---

[1] In case of iT_{11}, the vector polarisation provided by the low energy polarimeter could be used to determine the analysing powers simultaneously and that will in fact be shown later. However, for the determination of T_{20} this would introduce another unknown, which was not desired.

[2] Actually, the same RootSorter-based software was used for online analysis and later offline pre-analysis. Several adjustments were made depending on the requirements, *e.g.* a simplified, faster track reconstruction for online use. Nonetheless, the general information presented here was used both during online and offline use.

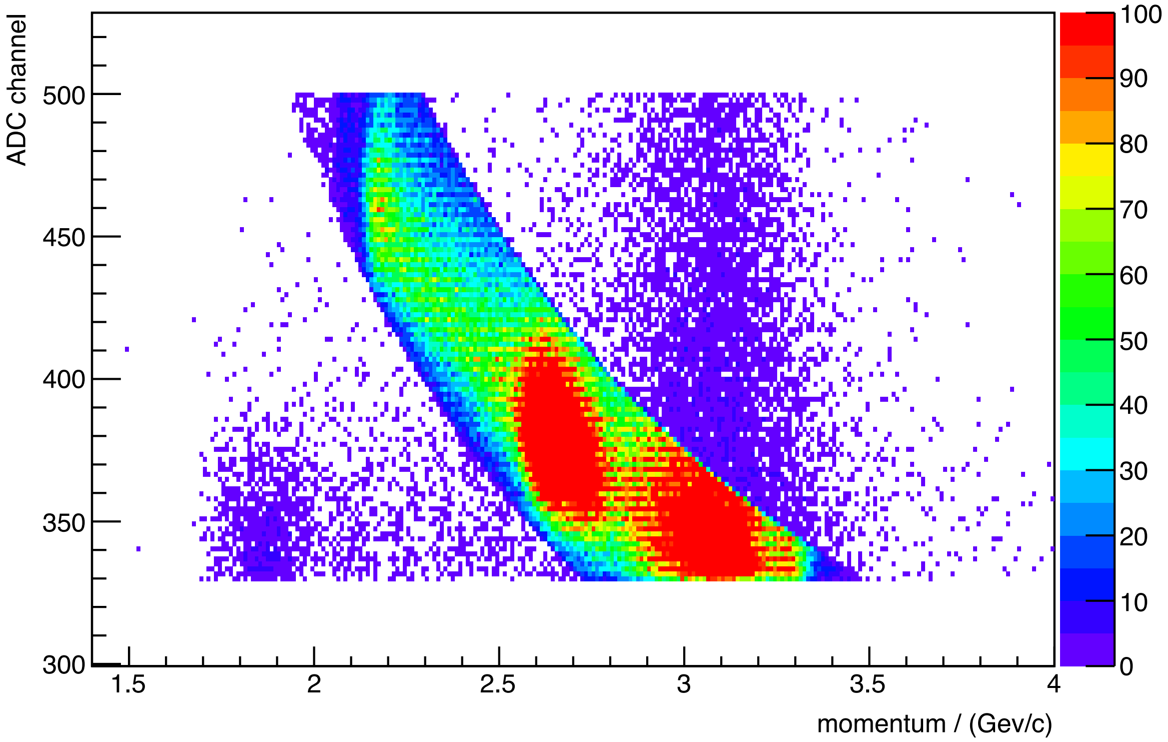

Figure 7.1: Energy loss plotted versus momentum in a single element of one of the forward hodoscopes. Shown are the ADC channels of the hodoscope module, which are proportional to the deposited energy in the scintillator. The selection criteria applied to these events are described in the text.

was implemented for the actual ^{3}He band. If a track would fulfil this selection criterion with at least one hit in either of the hodoscope module, the event would be retained. Therefore, some background outside the ^{3}He band, mainly consisting of stray protons, is still visible. This selection, however, was only applied to the first two layers of the hodoscope. In the third layer, signatures were much more compressed and bands could hardly be separated.

Since the hodoscope modules were performing very differently, although mostly adequately, the values for these criteria were determined for each element individually[3]. The exception was the fourth module in the third hodoscope layer. The plot of the energy loss versus the momentum for this module is shown in fig. 7.2. While the low momentum leg of the ^{3}He band is still visible, it is cut off around $p \approx 2.6\,\mathrm{GeV}/c$ (or rather at an ADC channel of ≈ 170), below the region where events from the $\vec{\mathrm{d}} + \mathrm{p} \to {}^3\mathrm{He} + \eta$ reaction are expected. During the set-up stage of the beam time, when the trigger threshold settings for individual hodoscope modules were set, the amount of statistics to produce the energy loss versus momentum plots was very low given the variance of the ion source and the

---

[3] Due to the fact that each module was treated individually and the energy loss information from the hodoscope was used exclusively for event identification in the analysis, a further calibration of these modules was obsolete.

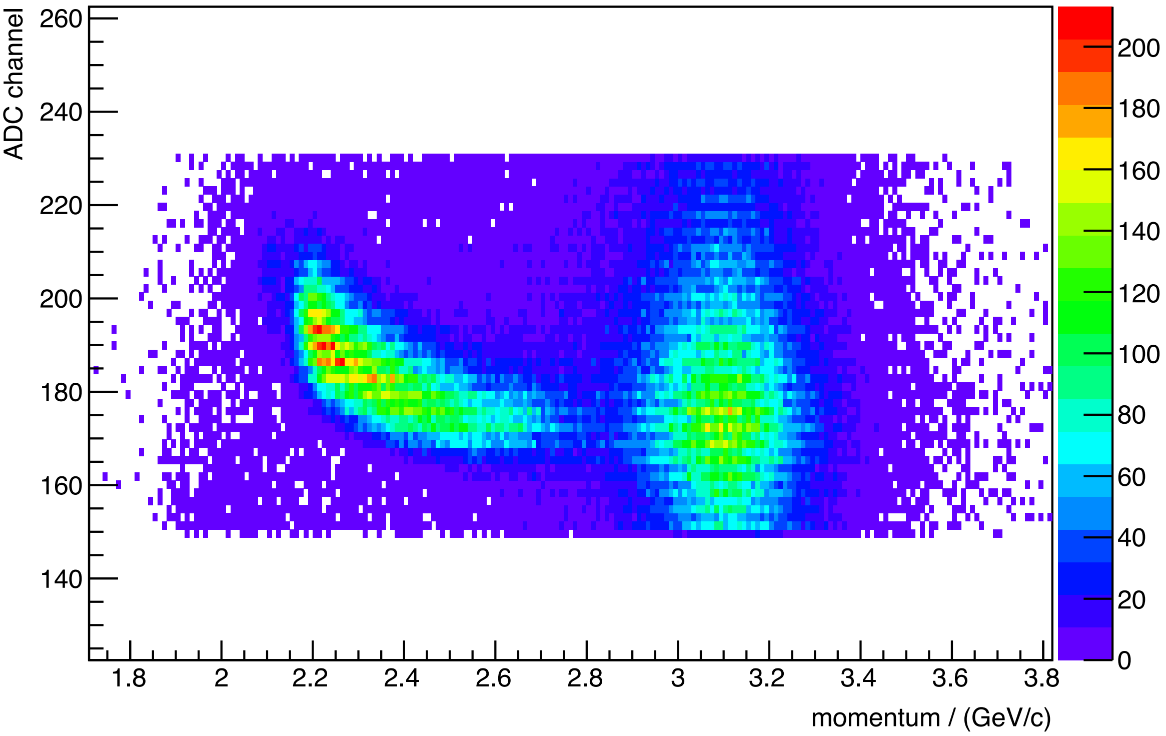

Figure 7.2: Energy loss plotted versus momentum for the defect element, *i.e.* the fourth module in the third layer of the forward hodoscopes. Shown are the ADC channels of the hodoscope module, which are proportional to the deposited energy in the scintillator. The selection criteria applied to these events are described in the text.

short amount of time to collect data[4]. While it is entirely possible that the trigger threshold for was set too high by mistake, it is impossible to reproduce whether this element was affected by a bad threshold value or a later drop of its performance after the settings were fixed. Nevertheless, $\vec{\mathrm{d}} + \mathrm{p} \to {}^3\mathrm{He} + \eta$ events in this region were not retained and the impact on the acceptance as well as the implications for the following analysis have to be studied with great care. This is explained in more detail in section 7.2.

In addition to the selection on the deposited energy, the possibility of further separating ^{3}He and proton ejectiles by the time of flight needed to traverse from the first two hodoscope layers to the third was considered. For this purpose, the of the average timing information in the first two layers and the third layer is used in conjunction with the reconstructed velocity of the track to calculate a virtual path length $s = \beta t_{\mathrm{diff}}$, with t_{diff} being the corresponding timing difference. The velocity of the particle was calculated from its energy and momentum by $\beta = p/E$ under the assumption that it was a ^{3}He nucleus. This method was employed with some success in the analysis of another measurement with nearly identical geometry [49, 64]. However, no clear separation between protons and ^{3}He ejectiles could be made even after a careful timing calibration of the in-

---

[4] The time used to populate the pictures during the beam time was limited to one or few hours, since finding the right settings was iterative process. Furthermore, due to limits imposed by the processing capabilities at the experiment, not all of the incoming events could be processed online.

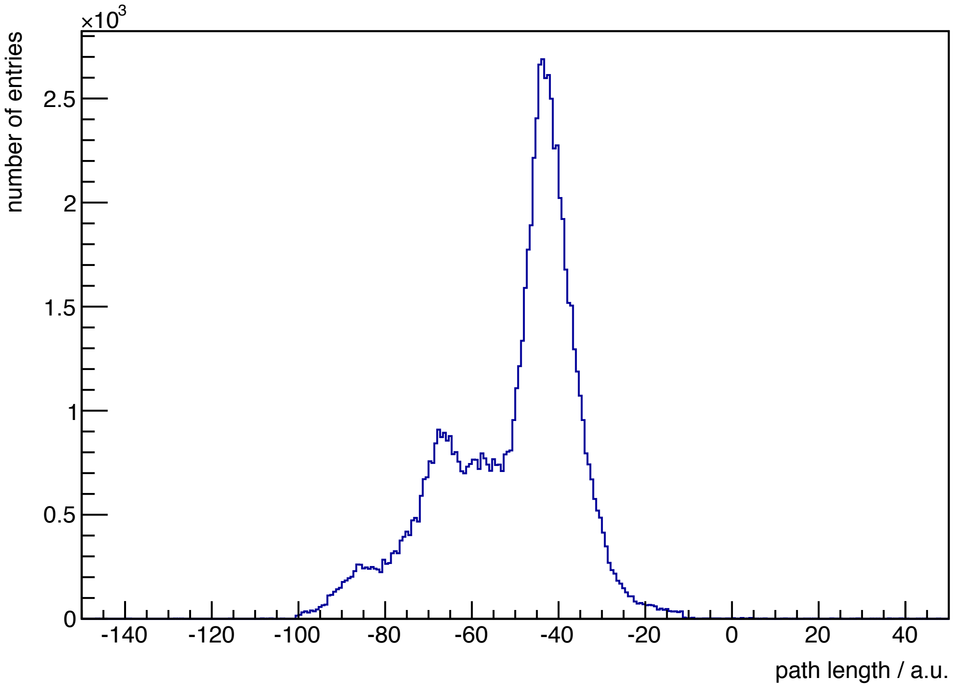

Figure 7.3: The reconstructed path length based on the timing information in the three layers of the hodoscope and the velocity of the ejectile. Details are given in the text.

dividual modules. An example for the fifth counter in the third layer is shown in fig. 7.3. Since only a relative calibration between the modules was performed, the absolute values for the path length are somewhat arbitrary and the unit given in fig. 7.3 reflects that. Similar to the observations in a previous measurement [49] it would be expected to find narrow peak for the ^{3}He ejectiles next to a wider distribution of protons. Something similar can be observed here, but especially with left hand side of the spectrum looking more erratic, it is difficult to make any reliable association with specific particles. A possible explanation for this behaviour could lie in the performance of the forward hodoscope during this beam time, *e.g.* caused by a different operating setup of the high voltages of the photomultiplier tubes. However, it is impossible to recreate the exact circumstances leading to this behaviour. Considering that the background could be well controlled even without a cut on the path length (see section 7.3), it was decided to discard this selection criterion.

7.2 Acceptance investigations

To study the impact of the defective hodoscope module on the acceptance, Monte Carlo simulations on the $\mathrm{d} + \mathrm{p} \rightarrow {}^3\mathrm{He} + \eta$ reaction were performed with the AnkeGeant4 framework. The full range of the continuous ramp was simulated both with a fully functioning ANKE set-up and with the particular module removed from the simulated set-up, respectively. For a first impression, the hit positions in the three wire chambers were projected on the x-y plane[5] and compared for the two settings. In figs. 7.4 to 7.6 this is shown for the excess energies $Q = 2, 6$, and 10 MeV. At $Q = 2$ MeV the impact on the acceptance is barely noticeable, although it can be seen when looking closely. At higher energies, though, the effect becomes more and more pronounced, resulting in a considerable part of the momentum sphere being lost. As mentioned above, this has serious implications for the feasibility of the analysis, given the fact that the unwanted analysing powers iT_{11} and T_{22} would contribute to the determination of T_{20} in an uncontrollable way, since eq. (7.0.4) would have to be used instead of eq. (7.0.5). While the very low energy data with $Q =< 2$ MeV are unaffected, the analysis of the data above that mark has to compensate for this effect. To find a way to mitigate the potential effects of iT_{11} and T_{22}, the angular distributions of the ^{3}He ejectiles have to be studied in more detail.

---

[5] Note that the trajectories of the ejectiles travelling through the wire chambers are nearly perpendicular to the chambers, *i.e.* they travel in the z-direction of the chambers.

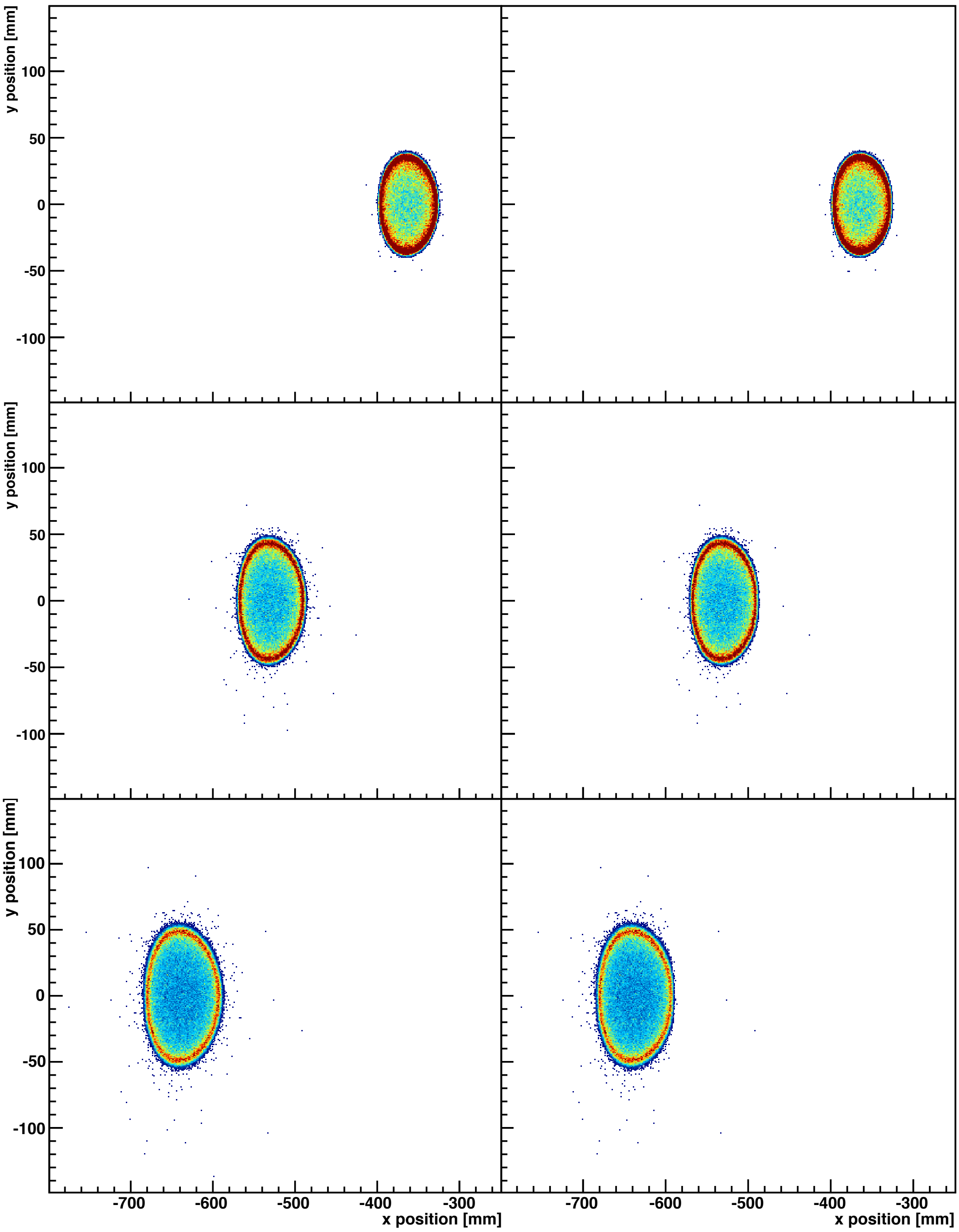

Figure 7.4: The hit positions projected on the x-y plane for the first (top), second (middle), and third (bottom) wire chamber at an excess energy $Q = 2\,\mathrm{MeV}$. On the left hand side, the results of a fully performing ANKE setup are shown. On the right hand side, the defect hodoscope module has been removed from the simulation.

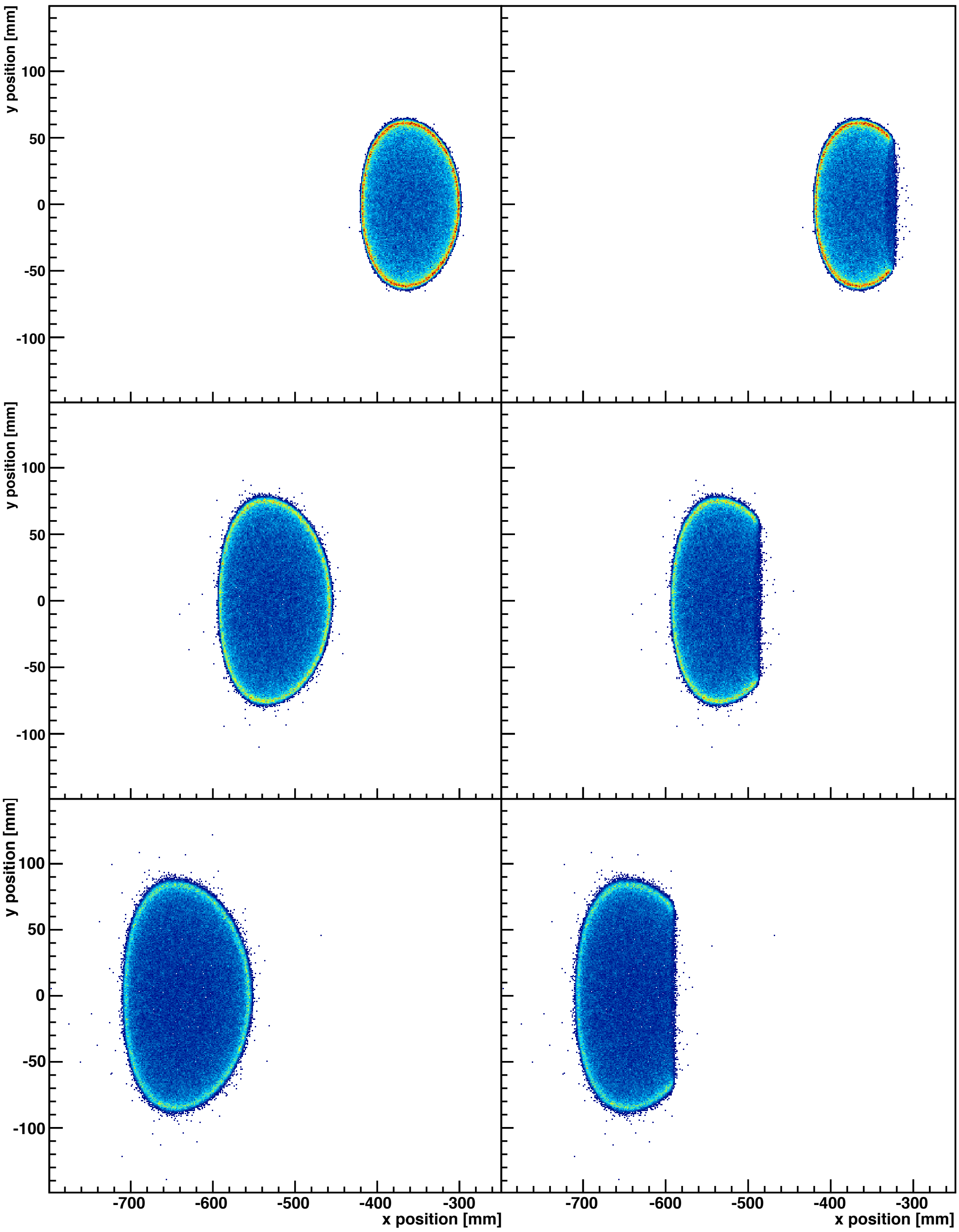

Figure 7.5: The hit positions projected on the x-y plane for the first (top), second (middle), and third (bottom) wire chamber at an excess energy $Q = 6\,\mathrm{MeV}$. On the left hand side, the results of a fully performing ANKE setup are shown. On the right hand side, the defect hodoscope module has been removed from the simulation.

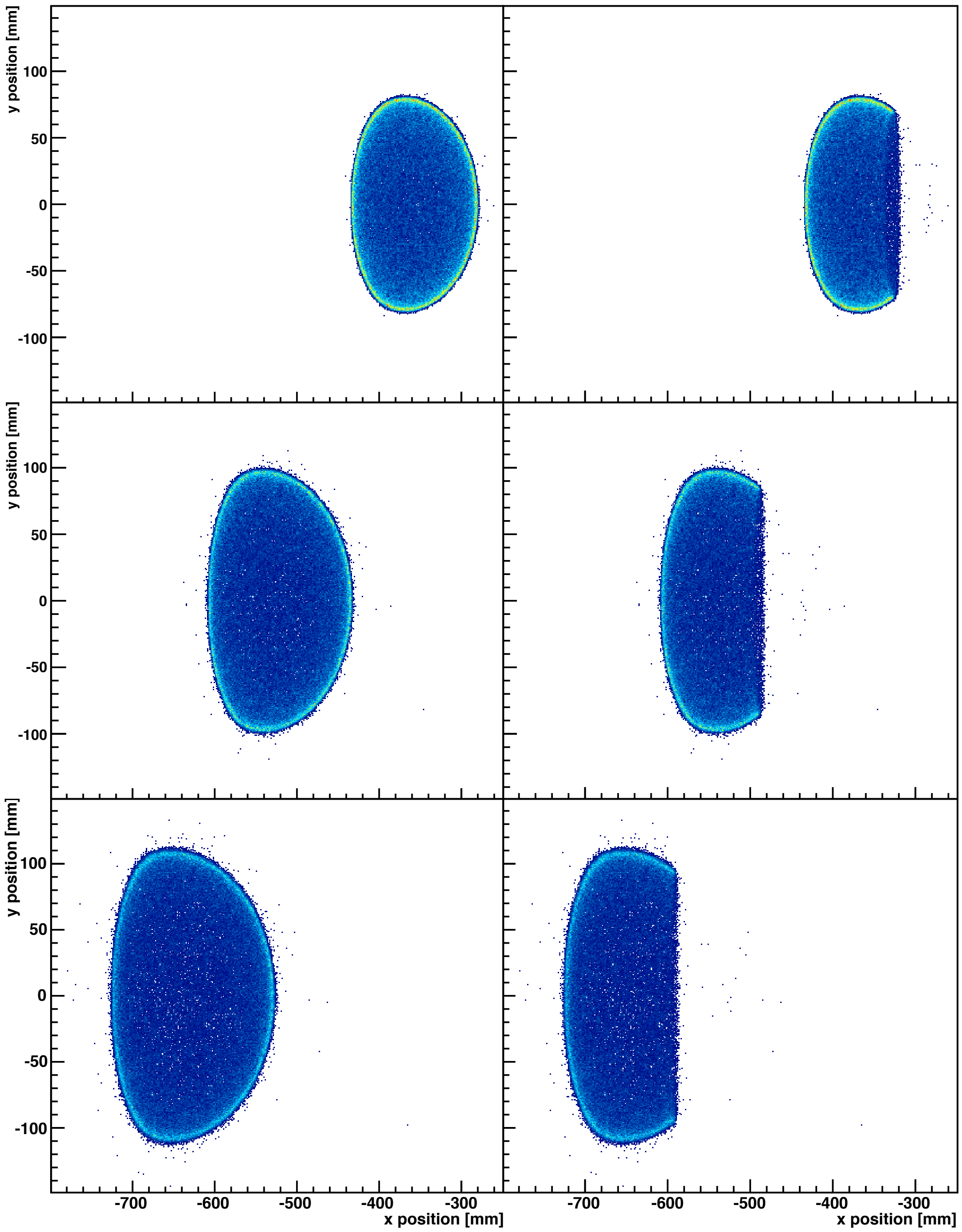

Figure 7.6: The hit positions projected on the x-y plane for the first (top), second (middle), and third (bottom) wire chamber at an excess energy $Q = 10\,\mathrm{MeV}$. On the left hand side, the results of a fully performing ANKE setup are shown. On the right hand side, the defect hodoscope module has been removed from the simulation.

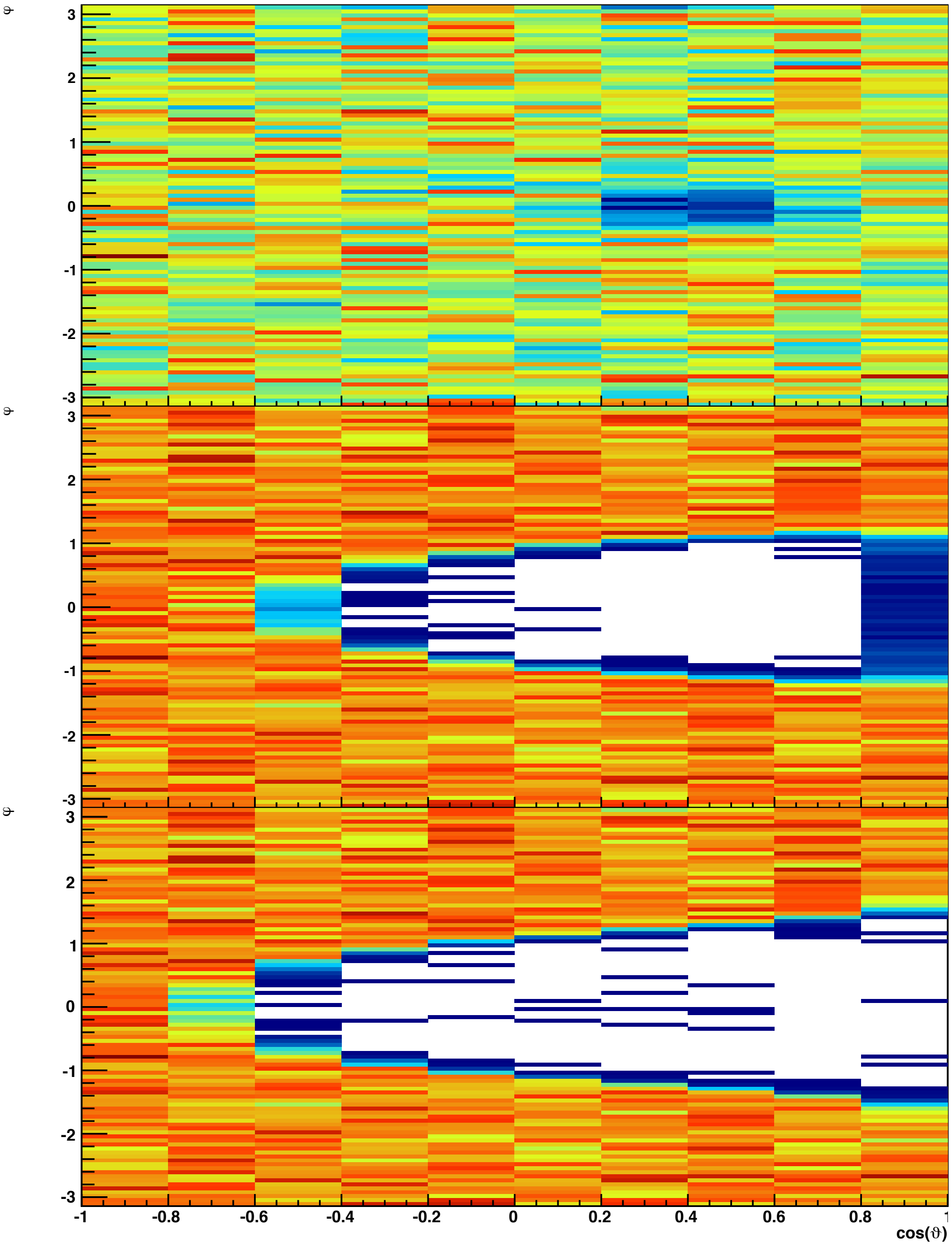

Figure 7.7: The azimuthal angle ϕ against the polar angle θ plotted at the excess energies $Q = 2\,\mathrm{MeV}$ (top), $Q = 6\,\mathrm{MeV}$ (middle), and $Q = 10\,\mathrm{MeV}$ (bottom).

In fig. 7.7 the azimuthal angle ϕ, with $\phi = 0$ pointing the direction of the x-axis away from the beam pipe, is plotted against the polar angle θ of the ${}^{3}\mathrm{He}$ ejectile in the centre of mass frame at the same aforementioned excess energies. The behaviour observed for the hit positions can be found here in a similar way. At the lowest energy, the angular distributions are affected in only a minor way. However, at higher energies a gaping hole is left in the acceptance. Interestingly, the effect is restricted to the angular range $-\pi/2 < \phi < \pi/2$, providing some leverage to mitigate the contributions from the non-T_{20} analysing powers. Furthermore, a drop in acceptance for $\cos\theta < 0.6$ could only be observed for the very highest energy bins, as can also be seen in the bottom picture of fig. 7.7. There, the area with $-0.8 < \cos\theta < -0.6$ and $-0.4 < \phi < 0.4$ shows a slight drop in acceptance as well. Keeping in mind the $\cos(2\phi)$ dependence of the T_{22} term in eq. (7.0.4), the data of all energies above 2 MeV were grouped into ten bins of $\cos\theta$ and four bins of ϕ in such a way that $\int \cos 2\phi \mathrm{d}\phi = 0$ for each $\cos\theta$ bin, *i.e.* $-\pi < \phi \leq -\pi/2$, $-\pi/2 < \phi \leq 0$, $0 < \phi \leq \pi/2$, and $\pi/2 < \phi \leq \pi$. Any possible contributions arising from the T_{22} term are eliminated this way. For the following extraction of T_{20}, all bins unaffected by a loss of acceptance were retained.

Although this is a great step towards the original goal of this measurement, there is still room for contribution from vector polarisation asymmetries arising from a possible non-zero iT_{11}. However, before this can be addressed in section 7.4, a background subtraction on the $\vec{\mathrm{d}} + \mathrm{p} \rightarrow {}^{3}\mathrm{He} + \eta$ reaction has to be performed.

7.3 Background subtraction

In case of the $\mathrm{d} + \mathrm{p} \rightarrow \{\mathrm{pp}\}_s + \mathrm{n}$ reaction, the background could be reduced substantially to negligible level by implementing smart cuts. In section 7.1, steps have been taken to significantly limit contributions from protonic background, even though they cannot be eliminated entirely. Furthermore, contributions from other reactions with ${}^{3}\mathrm{He}$ ejectiles $\mathrm{d} + \mathrm{p} \rightarrow {}^{3}\mathrm{He} + \mathrm{X}$ are not addressed by the selection on the ${}^{3}\mathrm{He}$ band. More specifically, background arises from the reactions involving multiple pions, *i.e.* $\mathrm{d} + \mathrm{p} \rightarrow {}^{3}\mathrm{He} + (\pi + \pi)^0$ and $\mathrm{d} + \mathrm{p} \rightarrow {}^{3}\mathrm{He} + (\pi + \pi + \pi)^0$. Due to the many-body kinematics, the ejectiles of these reactions assume a continuous momentum distribution between the kinematical limits, including the region where $\eta\,{}^{3}\mathrm{He}$ production is expected.

Instead of suppressing the background, which is hardly possible for kinematical reasons, it becomes more suitable here to describe it. A method using data taken below the $\eta\,{}^{3}\mathrm{He}$ production threshold has been successfully employed during an earlier measurement in the very same energy range [65]. Data taken in the excess energy range $-5\,\mathrm{MeV} < Q < -1\,\mathrm{MeV}$ were analysed as if they were taken at the respective energy above threshold. That effectively scales the ejectiles' momenta up to the kinematical limit defined by the center of mass energy. In the earlier analysis [65], this was possible due to the use of a polynomial momentum reconstruction, which related the straight tracks obtained from the wire chambers to corresponding momenta by means of previously generated coefficients, using the deuteron beam momentum as a parameter. The present analysis, however, was based on the more fundamental Runge-Kutta reconstruction method, which traced the trajectories of the charged particles back from wire chambers to the beam target overlap using previously measured maps of the D2's magnetic field. Since the

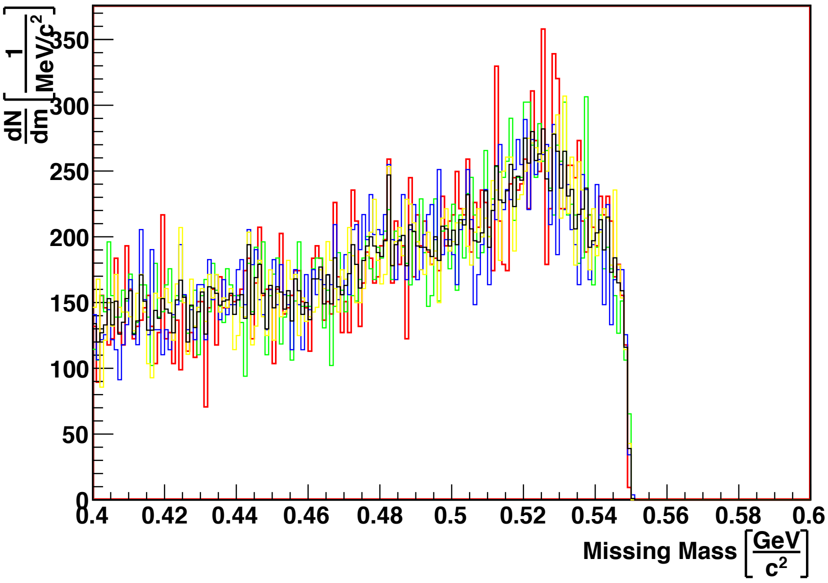

Figure 7.8: Missing mass distribution of the $\vec{d} + p \rightarrow {}^3He + X$ reactions taken below the $\eta\,{}^3$He production threshold and scaled to $Q = 0\,$MeV for $\cos\theta < 0$. Shown are the data for all polarisation modes combined (black) as well as for the individual modes 1 (red), 2 (blue), 3 (green), and the unpolarised mode (yellow).

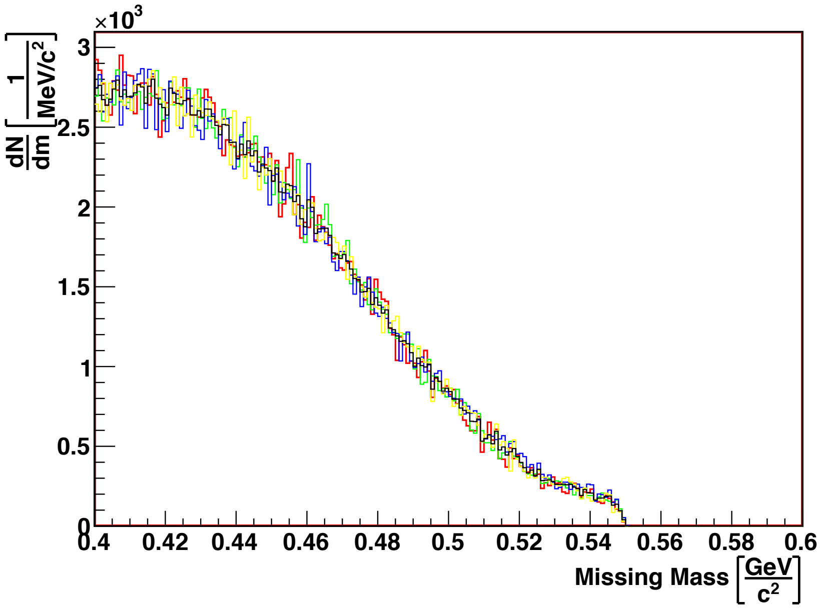

Figure 7.9: Missing mass distribution of the $\vec{d} + p \rightarrow {}^3He + X$ reactions taken below the $\eta\,{}^3$He production threshold and scaled to $Q = 0\,$MeV for $\cos\theta > 0$. Shown are the data for all polarisation modes combined (black) as well as for the individual modes 1 (red), 2 (blue), 3 (green), and the unpolarised mode (yellow).

beam momentum or any related quantities are used as input, the final state momenta have to be scaled to the desired energy after the reconstruction. Using the values for the beam momentum at the investigated energy p_{beam}, the beam momentum of the sub-threshold data $p^{\text{sub}}_{\text{beam}}$ and the reconstructed three-momentum of the sub-threshold ejectile $\vec{p}^{\,\text{sub}}_{\text{beam}}$ in the laboratory system, the desired, scaled momentum $\vec{p}_{\text{LS}}$ can be calculated by

$$\vec{p}_{\text{LS}} = \frac{p_{\text{beam}}}{p^{\text{sub}}_{\text{beam}}} \cdot \vec{p}^{\,\text{sub}}_{\text{beam}}. \tag{7.3.1}$$

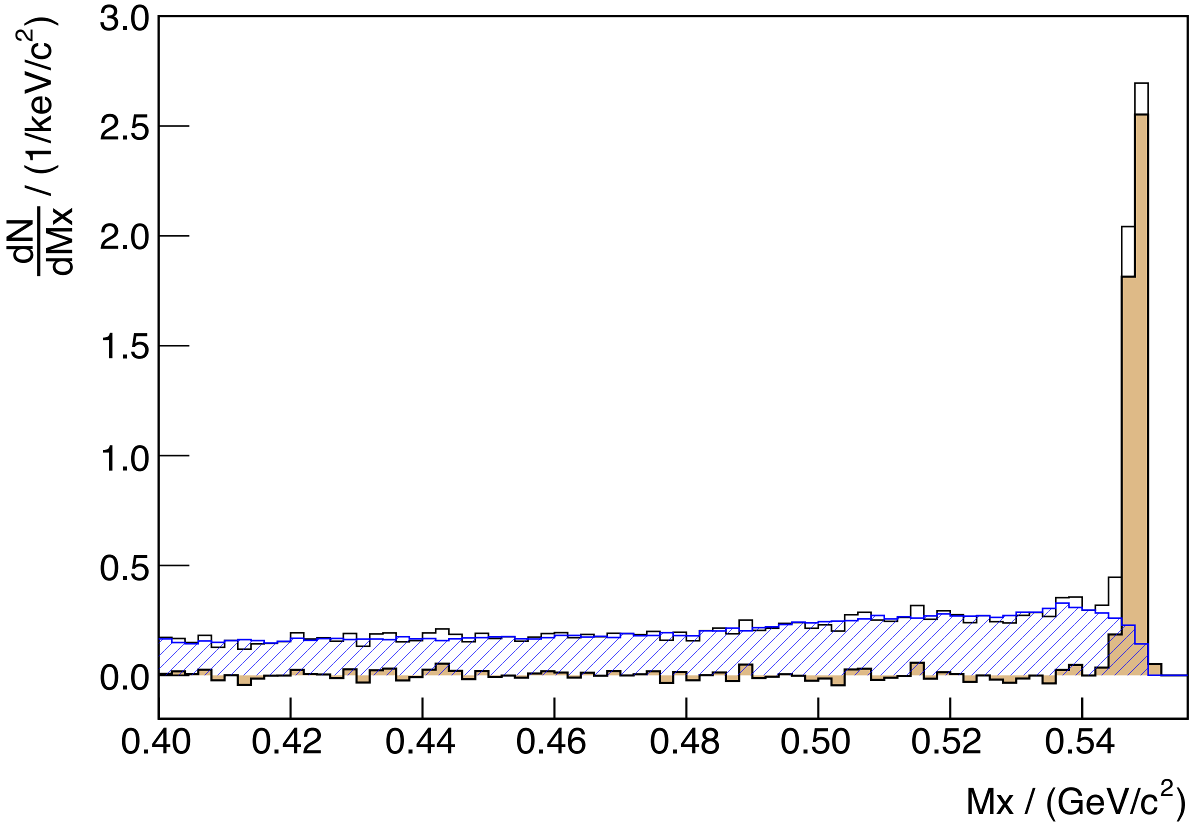

Figure 7.10: Missing mass distribution of the $\vec{\mathrm{d}} + \mathrm{p} \to {}^3\mathrm{He} + \mathrm{X}$ reactions at an excess energy $Q = 3\,\mathrm{MeV}$ with respect to the $\eta\,{}^3\mathrm{He}$ threshold (black). Data taken in the sub-threshold energy range of $-5\,\mathrm{MeV} < Q < -1\,\mathrm{MeV}$ were scaled to this energy and fitted to the data in the missing mass range $0.4\,\mathrm{GeV}/c^2 < \mathrm{Mx} < 0.52\,\mathrm{GeV}/c^2$ (blue). After the subtraction of the background, only a clean signal peak (brown shaded) remains.

Having scaled the sub-threshold momenta to the desired excess energy, the missing mass (Mx) distribution of the background can be fitted to the data. Before that, however, the possibility was investigated to combine the background of the different polarisations for the subtraction. Thus, possible differences in the shape of the background caused by the polarisation had to be studied. Figures 7.8 and 7.9 show the missing mass distributions for all polarisation modes of the ion source, including the one with a low tensor polarisation, together with the distribution of all modes combined. The pictures show data for the backward ($\cos\theta < 0$) and forward ($\cos\theta > 0$) hemisphere of the ^{3}He ejectile, respectively. Momenta were scaled to an excess energy $Q = 0\,\mathrm{MeV}$ and all distributions were normalised by means of their integral. The different shape of the distributions in both hemispheres arises from a different composition of background reactions. While in backward direction the $\mathrm{d} + \mathrm{p} \rightarrow {}^3\mathrm{He} + \mathrm{X}$ reactions are of the most relevance, in forward direction a substantial contribution of protonic background can be observed. This is consistent with the results presented in section 7.1. No significant differences of the background can be observed within its variance and in turn, the combined distribution is indistinguishable from the individual ones in terms of its shape. Henceforth, the combined distributions served as the background to be subtracted from the signal spectra. Thus, the amount of background events was effectively quadrupled, significantly reducing its contribution to the statistical uncertainties. In fig. 7.10, only the missing mass range with $0.4\,\mathrm{GeV}/c^2 < \mathrm{Mx} < 0.52\,\mathrm{GeV}/c^2$ was taken into account for scaling the background spectra, avoiding any possible contributions to the fit from the signal reaction itself. This technique was applied for all energy bins and polarisations.

7.4 Contributions from vector polarisation asymmetries

It has been shown in section 7.2 that, depending on excess energy Q and $\cos\theta$, the azimuthal acceptance is significantly limited. While any contributions from the tensor analysing power T_{22} could be eliminated by choosing a smart binning in terms of ϕ, the measurement of T_{20} is still open to possible contributions from vector polarisation asymmetries. Unfortunately, the iT_{11} term cannot be avoided in the same way as the T_{22} term. However, the term can be directly extracted from the data. As was shown in section 7.2, the angular regions with $\cos\theta < 0.6$ still provide full azimuthal acceptance. These regions can be used to measure the left/right asymmetry, *i.e.* $\phi = \pi$ versus $\phi = 0$, that arises from the vector polarisation. Given that the T_{20} term in eq. (3.1.15) has no dependence of ϕ and T_{22} can be neglected due to the chosen binning, eq. (3.1.15) can be written as

$$\sqrt{3} p_Z iT_{11} = C_n \left(\frac{N_L^{\uparrow}}{N_L^0} - \frac{N_R^{\uparrow}}{N_R^0} \right), \tag{7.4.1}$$

with N_L and N_R being the numbers of events that are scattered into the left ($\phi = \pi$) and right ($\phi = 0$) hemisphere, respectively. As mentioned in section 6.2.2, the efficiency of the detection system was studied and found to be rather flat and above 97% per wire chamber in the detection region of the $\vec{\mathrm{d}} + \mathrm{p} \rightarrow {}^3\mathrm{He} + \eta$ reaction. The fluctuations by themselves should have a negligible impact on the determination of the vector polarisation asymmetries and were also corrected for in the analysis.

The values have been determined for each bin of $\cos\theta$ and Q. As can be seen in eq. (3.3.1), iT_{11} has an inherent dependence on $\sin\theta$. Therefore, the numbers had to be corrected by the mean $\sin\theta$ value for each bin. The angle-averaged results shown in figs. 7.11 and 7.12 for polarisation modes 1 and 2. A fit has been applied to these data in terms of the final state η momentum p_η from $Q = 0\,\mathrm{MeV}$ up to $10\,\mathrm{MeV}$. This in compliance with eq. (3.3.1), which shows the dependence of iT_{11} on p_η. The two last points have been left out since a sufficient azimuthal acceptance cannot be guaranteed here any more, potentially distorting the result of the fit. Overall, the contributions from the vector polarisation asymmetries are small, but should still be corrected for. Therefore, the

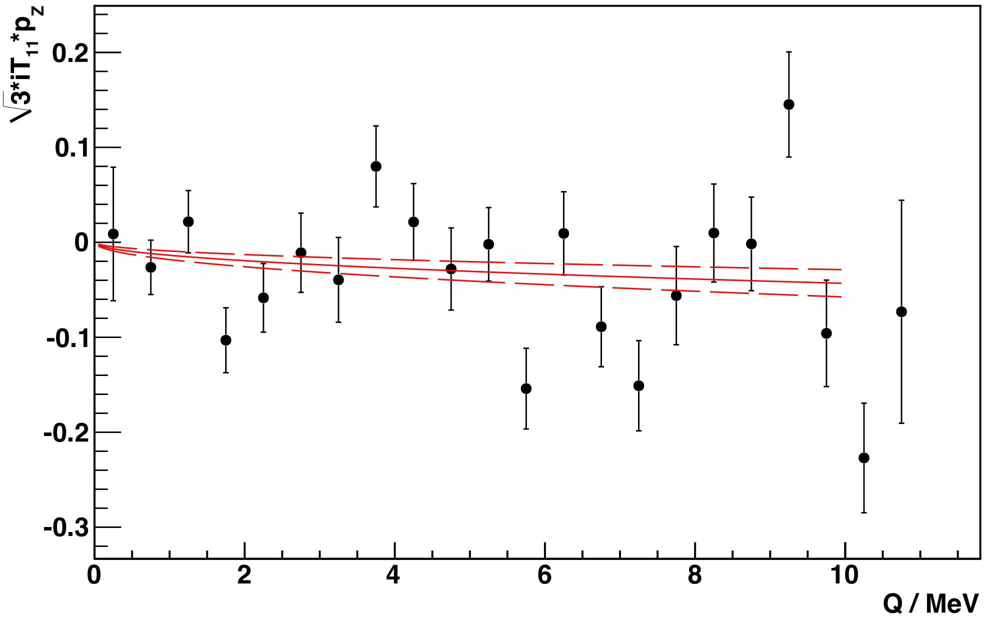

Figure 7.11: The iT_{11} term plotted against the excess energy Q for polarisation mode 1. Also shown is a fit to the data points including a linear dependence on p_η (solid red line) and its uncertainties (dashed red lines).

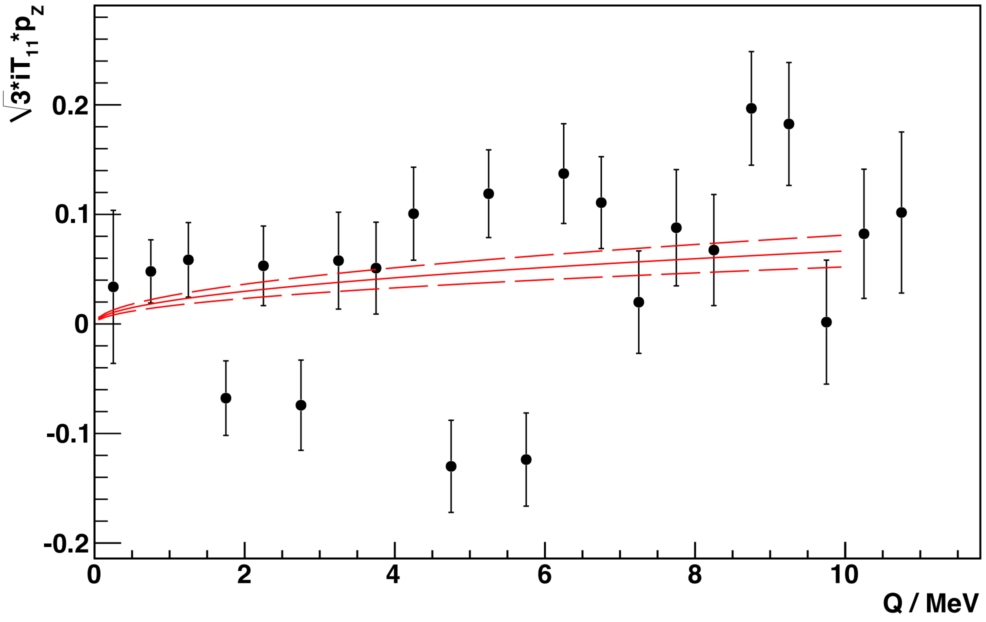

Figure 7.12: The iT_{11} term plotted against the excess energy Q for polarisation mode 2. Also shown is a fit to the data points including a linear dependence on p_η (solid red line) and its uncertainties (dashed red lines).

values of $\sqrt{3} \cdot iT_{11} \cdot p_Z$ obtained through the fit were directly fed into eq. (7.0.4) to finally calculate T_{20}.
Using the information on the vector polarisation provided by the low energy polarimeter given in table 6.1, it is possible to calculate iT_{11} from the data presented in figs. 7.11 and 7.12. It must be noted that these values were obtained in the beginning of the beam time at injection energy and not during the data taking runs. Using these polarisations, however, the fits showed that the vector analysing power remained $|iT_{11}| \lesssim 0.04$ for the excess energy $Q \leq 10\,\text{MeV}$. However, for the analysis described here only the numbers for $\sqrt{3}iT_{11}p_Z$ are of relevance, which can be extracted directly from figs. 7.11 and 7.12 as discussed above.

7.5 Extraction of T_{20}

Considering the binning defined in section 7.2, eq. (7.0.4) can be written in terms of only two analysing powers:

$$\frac{N^{\uparrow}}{N^{0}} = C_n \left(1 + \sqrt{3} p_Z iT_{11}(\theta) \cos\phi - \frac{1}{2\sqrt{2}} p_{ZZ} T_{20}(\theta)\right). \tag{7.5.1}$$

The normalisation factor C_n is derived in the very same way as already described in section 6.2.2 and has typical values of $C_n \approx 0.7$. With the vector polarisation asymmetries extracted in section 7.4, the iT_{11} term can be provided for every bin of the excess energy. After performing the background subtraction described in section 7.3, the numbers of polarised and unpolarised events, $N^{\uparrow}$ and N^0, could be extracted from the missing mass distributions by integrating over the $0.54\,\text{GeV}/c^2 < \text{Mx} < 0.57\,\text{GeV}/c^2$ region. The numbers of events were found to be in the range between $N \approx 2000$ up to $N \approx 5000$ per 250 keV excess energy bin. The data were binned in ten bins of $\cos\theta$ and four bins of ϕ according to the scheme derived in section 7.2. Only bins with a full acceptance were considered. Using eq. (7.5.1), T_{20} was calculated in of these bins and then averaged over $\cos\theta$ and ϕ for each Q bin. The extracted values are shown in figs. 7.13 and 7.14 for polarisation modes 1 and 2, respectively. The values obtained modes 1 and 2 are consistent within 2σ and are plotted against the excess energy Q, since the data were taken with a continuously ramped beam. The binning in Q of 0.5 MeV was chosen to match the amount of statistics obtained in the measurement.
Figure 7.15 shows the values of T_{20} averaged over both polarisation modes (black points) together with the values of an earlier measurement performed at Saclay [19]. Both measurements are well in agreement with each other. Fitting a constant to the data points reveals that

$$T_{20} = -0.21 \pm 0.02 \pm 0.05, \tag{7.5.2}$$

with a reduced χ^2 of 1.34, which shows that the data are consistent with a zero slope. Here, the first error is statistical and the second one is systematic. Since many effects, *e.g.* an absolute normalisation, cancel out when constructing the $N^{\uparrow}/N^{0}$ ratio, the latter is difficult to estimate. During the analysis it was found that using tensor polarisations obtained from the low momentum data at $2.435\,\text{GeV}/c$ instead of the ones obtained in the continuous ramp would affect the value of T_{20} by less than 0.02 while not having any influence on its angular or energy dependence. It was concluded that uncertainties

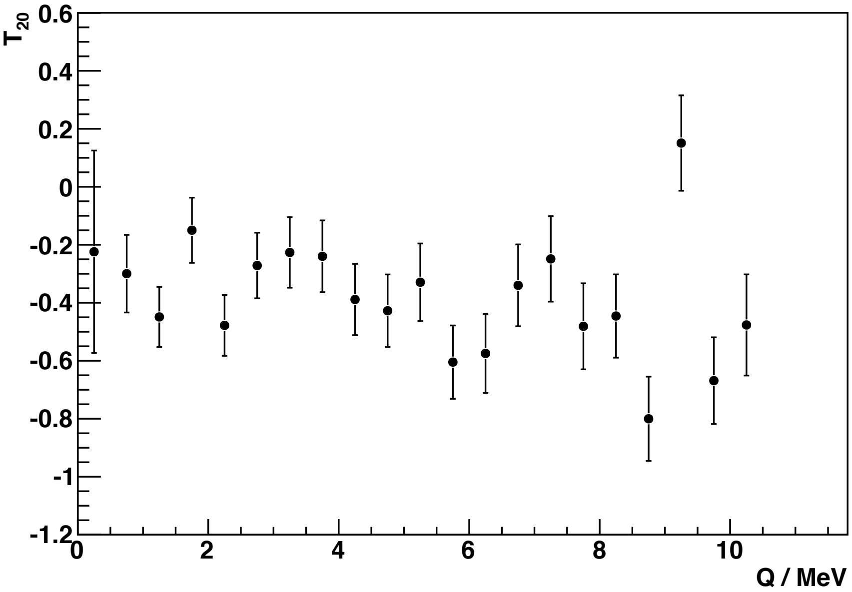

Figure 7.13: T_{20} plotted against the excess energy Q with respect to the $\eta\,^3$He production threshold. The values were determined for polarisation mode 1.

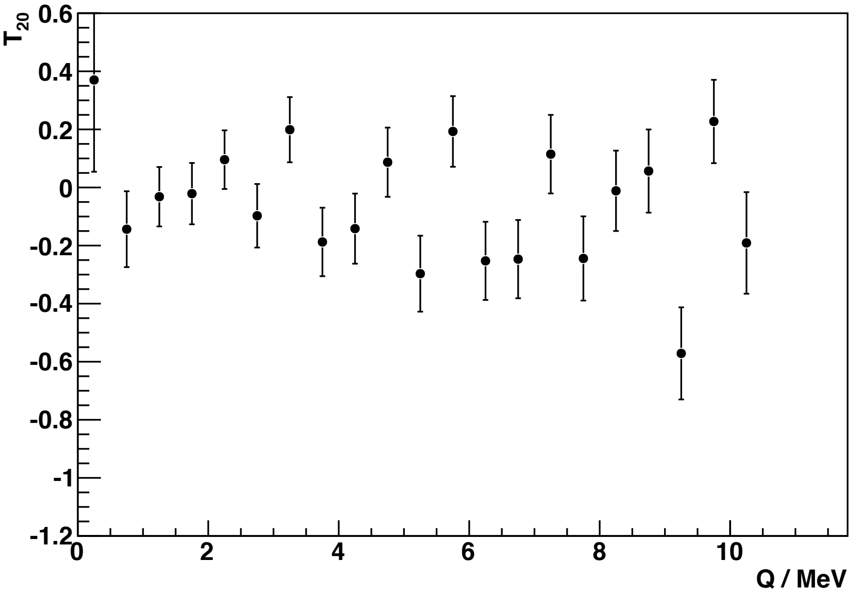

Figure 7.14: T_{20} plotted against the excess energy Q with respect to the $\eta\,^3$He production threshold. The values were determined for polarisation mode 2.

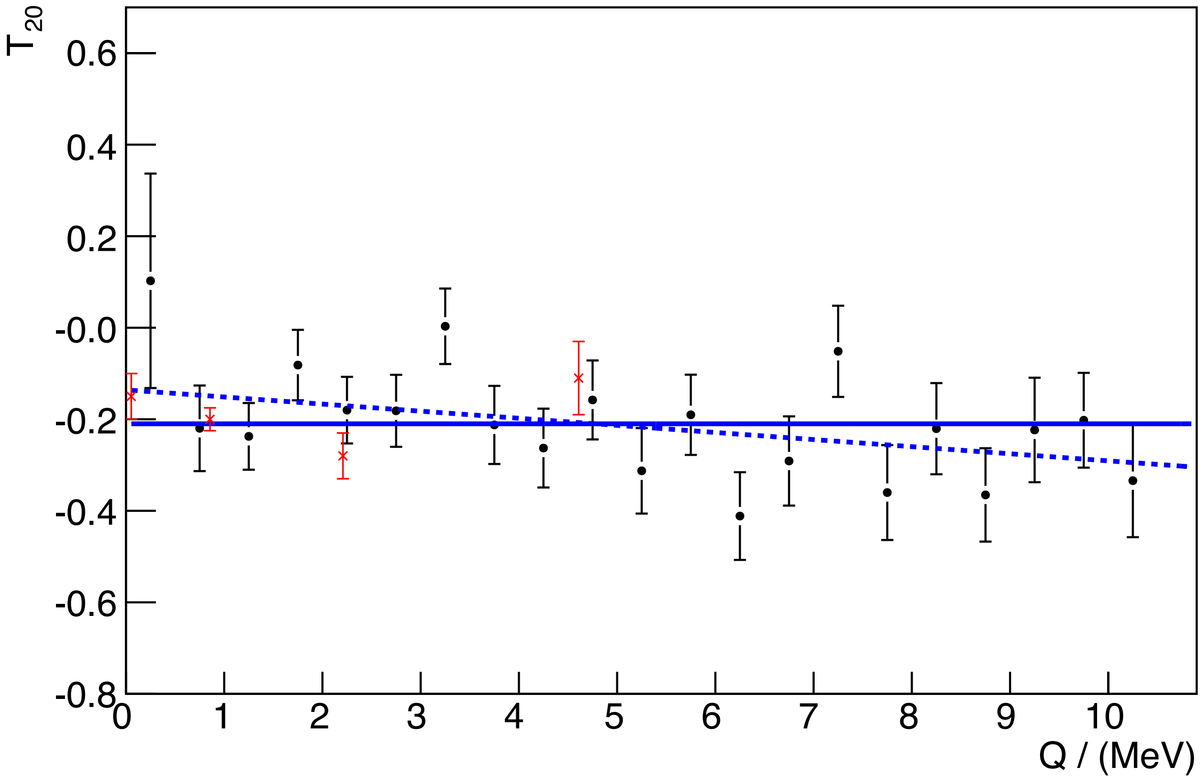

Figure 7.15: T_{20} plotted against the excess energy Q with respect to the $\eta\,^3$He production threshold. Presented here are the data from this measurement combined for both polarisation modes (black dots) together with a previous measurement performed at Saclay [19] (red crosses). Fits to the data were performed with both a constant (solid blue line) and a first order polynomial (dashed blue line). Details are given in the text.

from the beam polarisation, the geometry, the relative normalisation between the polarisation modes, and finally the contribution from iT_{11} would amount to the value given in eq. (7.5.2).

A marginal improvement in the description of the data points can be achieved by allowing a linear dependence on Q. The corresponding fit is shown as well in fig. 7.15 and results in

$$T_{20} = (-0.14 \pm 0.04) + (-0.02 \pm 0.01)Q, \tag{7.5.3}$$

with a reduced χ^2 of 1.17. In all fits, Q is measured in MeV.

The values of T_{20} have also been compiled in table 7.1.

Despite the unforeseeable technical limitations during the data taking process, the measurement has still produced considerably good results which were already published in refereed journal [93]. The precision of the values presented here is comparable with the ones provided by the measurement at Saclay, and both are in good agreement. The data from the measurement presented in this thesis, however, cover a much wider range of excess energies and provide detail about about the relative behaviour of T_{20} within this range. Having already determined T_{20} for many bins of $\cos\theta$ and ϕ, its angular dependence can now be studied. Furthermore, the squared s-wave amplitudes $|A|^2$ and $|B|^2$

(see eqs. (3.2.2) and (3.2.4)) can be extracted to investigate the implications of a possible spin dependence in the final state interaction of the $\vec{\mathrm{d}} + \mathrm{p} \rightarrow {}^3\mathrm{He} + \eta$ reaction, which is one major goal of these studies.

Table 7.1: Values for T_{20} averaged across all angles and the two polarisation modes with their statistical uncertainties. The data are presented in bins of the excess energy Q with a width of 0.5 MeV. The given Q-values refer to the centre of the according bin. The last data point at $Q = 10 - 25\,\mathrm{MeV}$ marks the end of the continuous ramp. Accordingly, not the whole width might be covered in that bin.

Q **[MeV]**	T_{20}	ΔT_{20}
0.25	0.10	0.23
0.75	-0.22	0.09
1.25	-0.24	0.07
1.75	-0.08	0.08
2.25	-0.18	0.07
2.75	-0.12	0.00
3.25	0.00	0.08
3.75	-0.21	0.09
4.25	-0.26	0.09
4.75	-0.16	0.09
5.25	-0.31	0.09
5.75	-0.19	0.09
6.25	-0.41	0.10
6.75	-0.29	0.10
7.25	-0.05	0.10
7.75	-0.36	0.10
8.25	-0.22	0.10
8.75	-0.37	0.10
9.25	-0.22	0.11
9.75	-0.20	0.10
10.25	-0.33	0.12

7.6 T_{20} asymmetries

In a previous, unpolarised measurement it was shown that the differential cross section of the $\mathrm{d} + \mathrm{p} \rightarrow {}^3\mathrm{He} + \eta$ reaction inhibited a linear dependence in $\cos\theta$ [9, 22], with θ being the polar angle in the centre of mass frame, already at unexpectedly low excess energies with $Q > 4\,\mathrm{MeV}$. This was explained by a rapid variation of the relative phase of the $s-$ and $p-$wave, a behaviour consistent with a quasi-bound state of the $\eta\,{}^3\mathrm{He}$ system [23]. Similarly, the asymmetry of T_{20} can be studied. Since T_{20} can be written as a function of the polarised and unpolarised cross sections (see eq. (3.2.3)), an asymmetry of T_{20} in $\cos\theta$ would be expected here as well. Of course, with the present set-up statistics are substantially lower than in the unpolarised case. Not only provides the unpolarised source generally much higher intensities, but here the data were spread across four polarisation modes and the results will be affected by the low value of T_{20} and the tensor polarisation p_{ZZ}. Nonetheless, defining an asymmetry parameter α through

$$\alpha = \left.\frac{\mathrm{d}T_{20}}{\mathrm{d}\cos\theta}\right|_{\cos\theta=0}, \tag{7.6.1}$$

the asymmetry of the tensor analysing power in $\cos\theta$ was determined for each energy bin. As an example, a plot of T_{20} agains $\cos\theta$ is shown in fig. 7.16 for an excess energy of 2.25 MeV. The values of the asymmetries are determined as the slope of the fit (black line), and are plotted against Q in fig. 7.17.

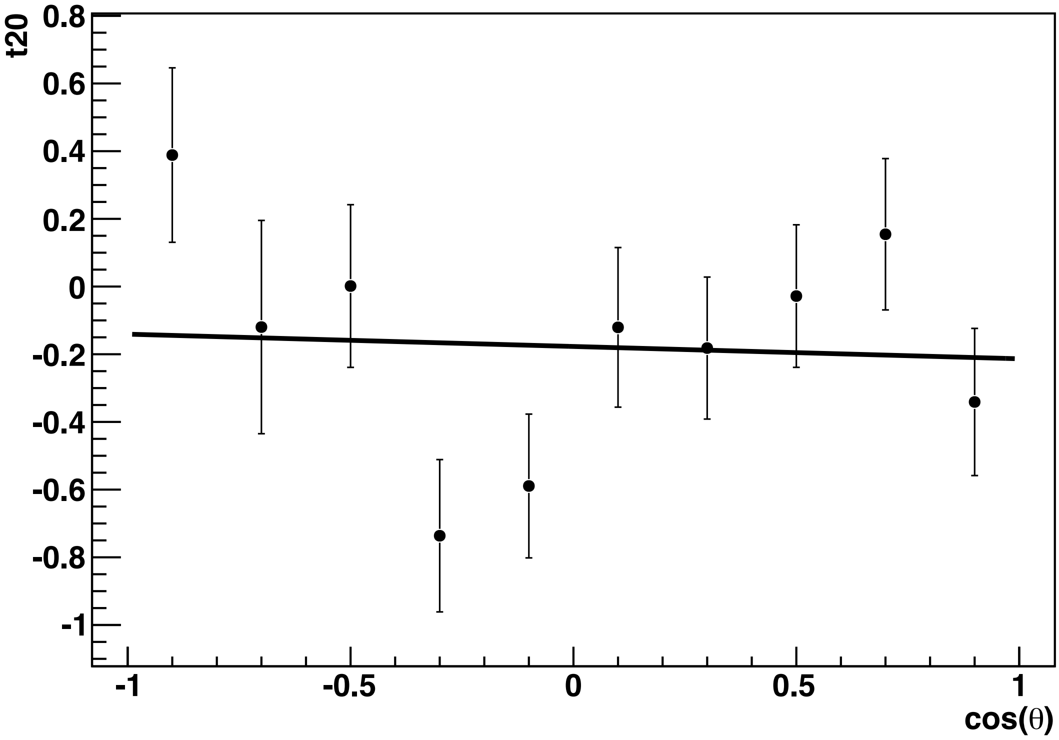

Figure 7.16: T_{20} plotted against $\cos\theta$ at an excess energy of 2.25 MeV. The asymmetry according to eq. (7.6.1) is extracted as the slope of the fit (black line).

It has been shown in section 2.2.1 that the asymmetry in $\cos\theta$ arises from an interference of the s- and the p-wave[6]. The interference term in eq. (2.2.10) is an odd function of the centre of mass momentum p_η, which therefore has to vanish at the production threshold. Figure 7.17 shows that the values found for α are compatible with zero throughout the whole energy range. In compliance with the aforementioned p_η dependence of the asymmetry parameter, the best fit to the data points is linear in p_η and yields

$$\alpha = (0.0002 \pm 0.0005)p_\eta, \tag{7.6.2}$$

---

[6] Note that since T_{20} can be written as a function of the cross section, the origin of the asymmetry is the same for the tensor analysing power and the differential cross section.

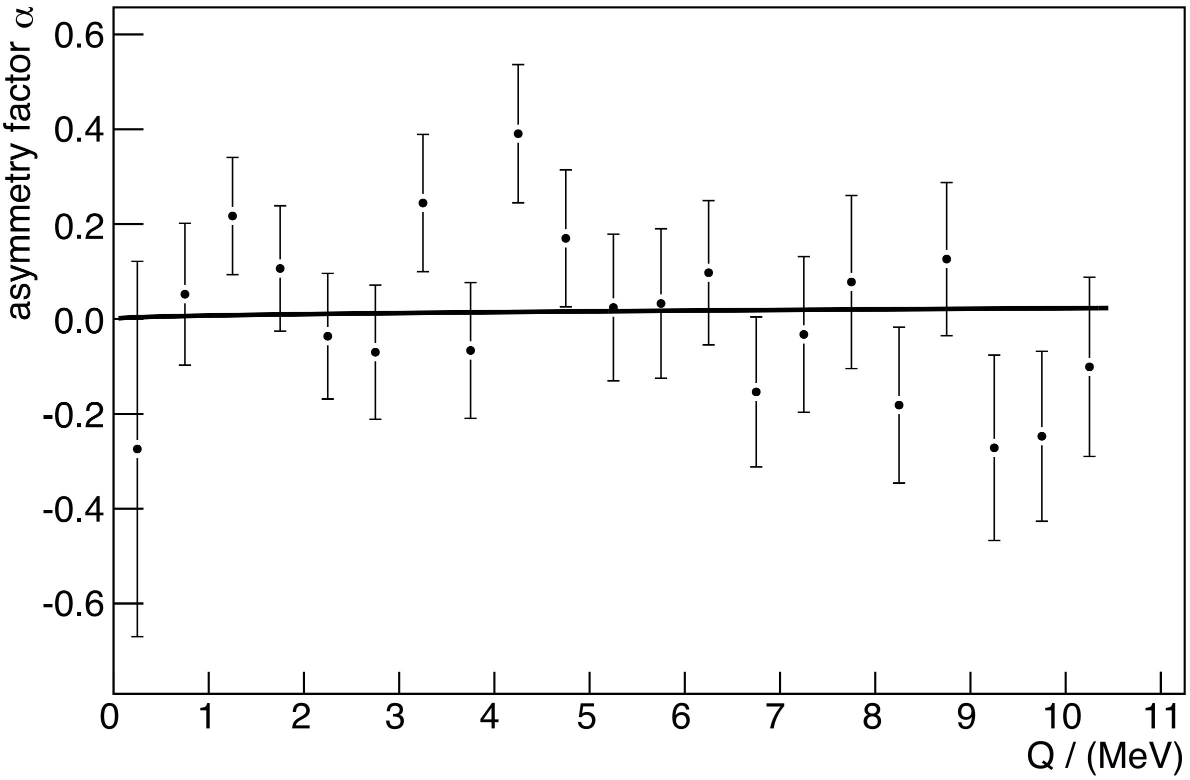

Figure 7.17: The asymmetry parameter α plotted against the excess energy Q. Also shown is a fit to the data points. Details are given in the text.

with a reduced χ^2 of 1.19 and p_η being measured in MeV/c. There is no sign of any interference between the s- and p-wave here, even though the unpolarised data inhibited a significant non-isotropy [93, 23]. This is certainly unexpected and has some implications for the assumptions made for the production amplitude. This will be discussed in more detail in section 7.8.

7.7 Squared amplitudes $|A|^2$ and $|B|^2$

Combining the newfound knowledge of T_{20}'s energy dependence with that of the unpolarised production amplitude determined at the earlier measurement [9, 23], the two squared independent scalar amplitudes $|A|^2$ and $|B|^2$ can be extracted from the data at hand. It has been shown in section 3.2 that at low energies, when the $\eta\,^3$He system can be assumed to be in relative s-wave, T_{20} can be expressed by the squared amplitudes $|A|^2$ and $|B|^2$ by means of eq. (3.2.4).

The previous measurements of the unpolarised differential cross sections [9, 22] showed that at energies with $Q \gtrsim 4\,\mathrm{MeV}$, small contributions from the p-waves are already visible. However, it was shown that this does not significantly impact the extrapolation to the pole in the production amplitude [23], and it is useful to determine the angular averages of $|A|^2$ and $|B|^2$ as functions of the excess energy Q. These can be determined by combining eqs. (3.2.2) and (3.2.4), using the parametrisation of the differential cross section from

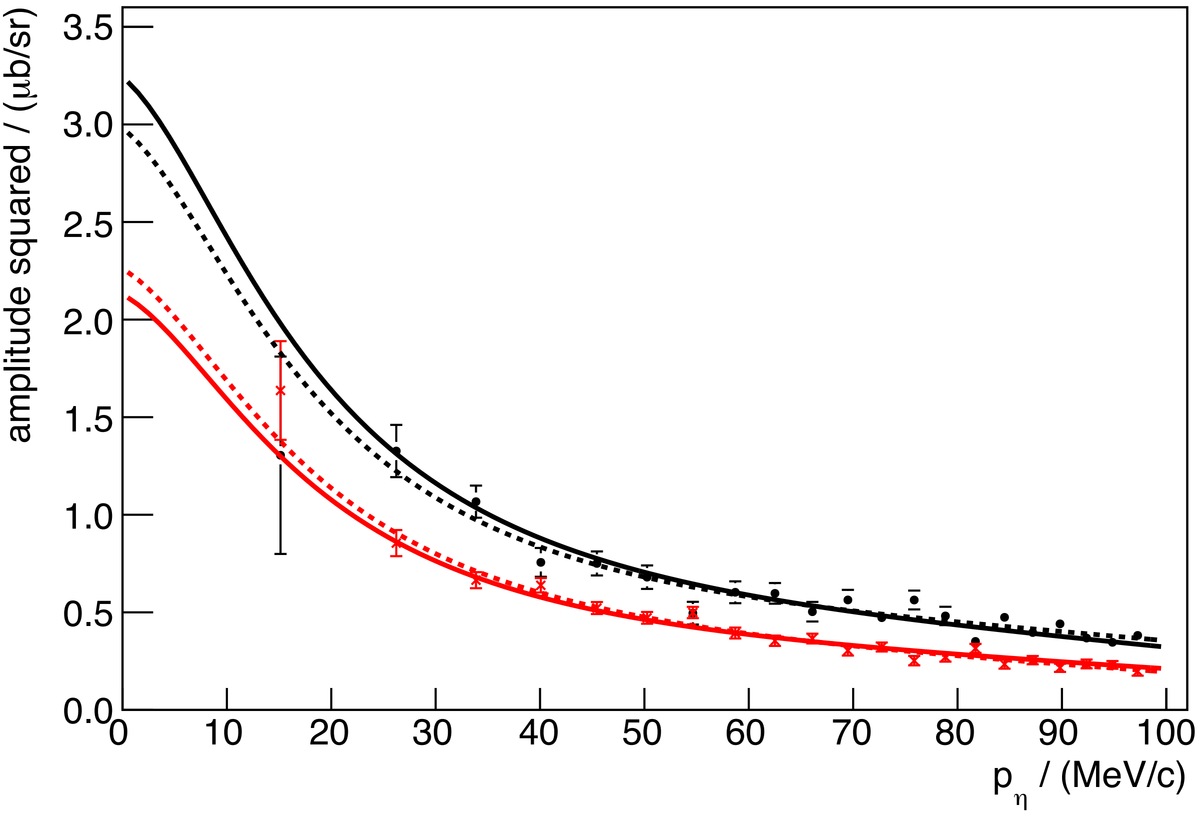

Figure 7.18: The two squared amplitudes $|A|^2$ (black dots) and $|B|^2$ (red crosses) plotted against the final state momentum p_η. The data were binned in 0.5 MeV steps of the excess energy Q, which has been converted here to bins of the final state momentum p_η, and deduced from the present determination of T_{20} and the previous ANKE measurement of the differential cross section [9]. The solid and dashed lines are based on the values given for T_{20} in eqs. (7.5.2) and (7.5.3).

the earlier, unpolarised ANKE measurement [9]. The results for the squared amplitudes are plotted in fig. 7.18 against the final state momentum p_η. In addition to the individual data points, lines are shown representing the values obtained through the constant (solid) and linear (dashed) fits in eqs. (7.5.2) and (7.5.3), respectively.

Figure 7.18 displays the violent behaviour caused by the strong final state interaction already observed in the earlier unpolarised measurements. Still, if T_{20} is independent of the excess energy Q, which is consistent with eq. (7.5.2), the same has to be true for the ratio of the squared amplitudes $|A|^2/|B|^2$. Allowing a linear slope, however, the ratio derived from the fit in eq. (7.5.3) yields:

$$\frac{|B|^2}{|A|^2} = (0.75 \pm 0.06) - (0.014 \pm 0.014)\,\mathrm{MeV}^{-1} \cdot Q. \tag{7.7.1}$$

If a variation like this exists, the energy on which it occurs can be estimated by means of eq. (7.7.1) and would likely be in the order of $0.75/0.014\,\mathrm{MeV}^{-1} \approx 50\,\mathrm{MeV}$ [93]. In contrast, the rapid rise of the unpolarised cross section associated with the $\eta\,{}^3$He final state interaction happens within 1 MeV of the production threshold. Changes on the scale of 50 MeV could be introduced by initial state interaction or the reaction mechanism itself.

However, the energy range and precision of the present data do not warrant any further speculation.

7.8 Interpretation of the results

The present analysis revealed that T_{20} can be well described with no energy dependence (see eq. (7.5.2)). Even though a slightly better result can be achieved by allowing a linear slope in the excess energy Q (see eq. (7.5.3)), the resulting energy dependence remains rather small. This is consistent with a small dependence of the final state interaction on the total spin of the initial state.

In order to relate this closer to the production amplitude, the squared s-wave amplitudes $|A|^2$ and $|B|^2$ were extracted and shown in fig. 7.18. In addition to the individual data points, the cases of eqs. (7.5.2) and (7.5.3) were drawn for comparison. While the former case corresponds to there being no spin dependence in the final state interaction, the latter allows one. However, judging the difference of these two cases in fig. 7.18 against the overall of the squared amplitudes in the presented energy range, any contribution from a spin dependence to the final state interaction must be rather small.

In general the $\mathrm{d} + \mathrm{p} \to {}^3\mathrm{He} + \eta$ reaction has to be described by six invariant amplitudes [94]. A comprehensive and unambiguous analysis of the amplitudes would require the measurement of additional spin observables. In addition to the analysing powers, spin correlation coefficients and also the polarisation transfer coefficients would have to be extracted. This would of course require a much more complex experimental set-up than the one this analysis is based on. A follow-up investigation for the unpolarised data attempted to account for the possible effects from p-waves, retaining only two of the five p-wave amplitudes [23]. However, due the lack of reliable data on the vector analysing power iT_{11}, the decomposition of the data is very ambiguous. In an effort to describe the main features of the data presented here, an ansatz could take the form of [93]:

$$A = A_0 \left[\mathrm{FSI}(p_\eta) + \alpha p_\eta \cos\theta + \beta p_\eta^2 (3\cos^2\theta - 1)/2\right] \tag{7.8.1}$$

and

$$B = B_0 \left[\mathrm{FSI}(p_\eta) + \alpha p_\eta \cos\theta + \beta p_\eta^2 (3\cos^2\theta - 1)/2\right], \tag{7.8.2}$$

in which the final state interaction $\mathrm{FSI}(p_\eta)$ only affects the s-wave term. This ansatz has B being proportional to A in terms of the final state momentum p_η and the polar angle θ. This way, despite the significant anisotropy of the differential cross section seen for unpolarised data at higher p_η [9, 22], T_{20} would remain independent on these observables. The linear slope of the cross section in $\cos\theta$ could then well be caused by a cancelation of the $s-d$-wave interference and the squared p-waves.

The vector analysing power vanishes in the model that depends solely on A and B[7]. The inclusion of the two additional spin amplitudes C and D shown in eq. (3.3.1) [23], though, could give rise to a non-zero contribution from the iT_{11} term. In section 7.4 it was found that these were limited by $|iT_{11}| \lesssim 0.04$, which does not contradict the $A + B$ model employed here.

---

[7] If $C = D = 0$, then vector analysing term (eq. (3.3.1)) also becomes zero (see section 3.3).

As a conclusion, the small energy dependence of the tensor analysing power T_{20} strongly supports the assumption that the rapid variation of the amplitudes close to the $\eta\,^3$He production threshold is in fact caused by an s-wave final state interaction common to both initial spin states. This is also consistent with the fact that the description of the unpolarised data yielded a pole at very low absolute values of the excess energy with $|Q| \approx 0.4\,\mathrm{MeV}$ [21]. In case of A and B having poles at very different values of Q a stronger energy dependence of T_{20} would have been found.
It was found in section 7.6 that there is no significant asymmetry of the values for T_{20} between the forward and backward direction. This is in strong contrast to what was observed for the unpolarised cross sections and provides information on the spin structure of the scattering amplitude. The lack of asymmetry found here is consistent with the assumption that only the amplitudes A and B play an important role in the scattering amplitude and that they have a similar angular dependence. This is reflected in the ansatz presented in eqs. (7.8.1) and (7.8.2) and might help in the further development of models for the $\mathrm{d} + \mathrm{p} \to {}^3\mathrm{He} + \eta$ reaction. A possible explanation for this behaviour could be that the $s - p$ interference is not as strong as expected from the unpolarised data.
The results of this work [93] have been put into a larger context in different overviews of the search for η-mesic nuclei [16, 21].

Chapter 8

Summary and outlook

Previous unpolarised measurements on the $\mathrm{d} + \mathrm{p} \to {}^3\mathrm{He} + \eta$ reaction revealed a surprisingly strong enhancement in the total cross section close to the production threshold, coupled with a quickly rising asymmetry in the differential cross section. The enhancement was associated with a strong final state interaction, whereas the asymmetry was thought to arise from a strong interference between the $s-$ and $p-$wave of the $\eta\,{}^3$He system. This was interpreted as evidence for the presence of an $\eta\,{}^3$He quasi-bound state, which was supported by the findings in other channels. However, in the $\mathrm{d} + \mathrm{p} \to {}^3\mathrm{He} + \eta$ reaction, the $s-$wave final state can be accessed via two different spin states of the dp-system. This could affect the shape of the cross section and consequently the FSI interpretation. Therefore, the goal of this thesis was to study the energy dependence of the deuteron tensor analysing power T_{20} in the $\vec{\mathrm{d}} + \mathrm{p} \to {}^3\mathrm{He} + \eta$ reaction in the excess energy range $0\,\mathrm{MeV} < Q < 11\,\mathrm{MeV}$, and thereby probe for a dependence of the final state interaction on the total spin of the initial deuteron-proton system.

A software framework, the *Reconstruction*, was developed first for the analysis of these data and then extended in its functionality to serve as more of a general purpose tool for analyses with the ANKE experiment. Particular efforts were made to smoothen the learning curve for new students. This positively changed the range of possibilities in terms of what kinds of analyses could be performed within a short time frame. Nowadays, the *Reconstruction* has become a standard for analysis in the ANKE Münster group.

Despite technical challenges arising during the beam time and the analysis, the measurement led to important results, representing another step in the search for a quasi-bound or virtual state of the $\eta\,{}^3$He system.

While the vector polarisation was determined in the beginning of the measurement with the COSY low energy polarimeter at injection energy, the tensor polarisation of the deuteron was extracted from data on the $\vec{\mathrm{d}}+\mathrm{p} \to \{\mathrm{pp}\}_s+\mathrm{n}$ reaction within the continuous ramp in which also the main reaction was studied. This kept systematic effects between the determination of the polarisation and the analysing powers to a minimum and the polarisations were confirmed with data taken at a lower beam momentum. Since the events for this reaction were collected with a different trigger than the main reaction, it was unaffected by the problems with one of the hodoscope modules first mentioned in section 4.3.3.

The original concept for extracting T_{20} in the $\vec{\mathrm{d}} + \mathrm{p} \to {}^3\mathrm{He} + \eta$ reaction required a full geometrical acceptance for this process. However, in the analysis it was found that the acceptance was significantly reduced due to the problems with the aforementioned hodoscope module, and this concept had to be revised. A binning in $\cos\vartheta$ and φ was chosen that eliminated any contribution from the tensor analysing power T_{22}. The remaining $\cos\vartheta$ areas, which still provided full azimuthal acceptance, were then used to determine the asymmetries arising from the vector polarisation. With this revised concept, T_{20} could be successfully extracted from the data.

The near-constancy of T_{20} in the observed energy range leads to the conclusion that $\eta\,^3$He s-wave interaction is not affected by the different spin combinations in the initial state. This strongly supports the assumptions that were made based on the unpolarised data, *i.e.* that the pole in the scattering amplitude amplitude arises in fact from a strong final state interaction. Combining the results for T_{20} with the knowledge on the scattering amplitude from the unpolarised data allowed the determination of the squared s-wave amplitudes $|A|^2$ and $|B|^2$. The slope of the $|A|^2/|B|^2$ suggests that a variation caused by the total initial state spin would likely happen on a much larger energy scale than the one observed in the unpolarised data. Interestingly, the significant asymmetry in $\cos\vartheta$ of the differential cross section was not found in T_{20}. Based on this, the structure of A and B was revised to be in accordance with this result.

Determining the analysing power across the observed energy range revealed that T_{20} is near constant. This leads to the conclusion that the $\mathrm{d} + \mathrm{p} \to {}^3\mathrm{He} + \eta$ reaction inhibits the same energy dependence regards less of the spin combination in the initial state at low energies. As a consequence, the shape of the total cross section determined for the unpolarised data is unaffected by the spin states, leaving the FSI interpretation intact. Combining the results for T_{20} with the knowledge on the scattering amplitude from the unpolarised data allowed the determination of the squared s-wave amplitudes $|A|^2$ and $|B|^2$. These were found to be of similar size. Furthermore, allowing a linear energy dependence in the description of the T_{20} had nearly no impact on the shape or the strength of these amplitudes. The slope of the $|A|^2/|B|^2$ ratio suggests that a variation caused by the total initial state spin would likely happen on a much larger energy scale than the one observed in the unpolarised data. This all supports the evidence for a quasi-bound state. Interestingly though, the significant angular asymmetry in $\cos\vartheta$ of the differential cross section was not found in T_{20}. The energy dependence of the asymmetry in the unpolarised data was associated with an $s-p-$wave interference. In the presence of such an interference T_{20} is expected to inhibit a similar asymmetry as well. Based on this, the structure of A and B was revised to be in accordance with this result. The lack of the angular asymmetry in T_{20} may suggest that the $s-p-$interference is in fact not as strong as previously anticipated. Higher precision data in the unpolarised case could help clarify this situation. Fortunately, such an analysis currently underway [95] based on earlier obtained high statistics and high precision COSY-ANKE data in the $0\,\mathrm{MeV} < Q < 15\,\mathrm{MeV}$ range. These might be complemented by higher energy data from WASA-at-COSY as well [96], providing more data in a range when higher partial waves start to contribute to the shape of the differential cross section.

The data presented here have been published in a refereed journal [93]. Later, two review articles put this work into the larger context of η production experiments [21] and the search for η-mesic nuclei [16].

The results presented here might help with the further development of phenomenological models for the $\mathrm{d} + \mathrm{p} \to {}^3\mathrm{He} + \eta$ reaction. It was suggested that the spin correlation parameter C_{yy} would be sensitive to further interferences between the partial wave amplitudes [23] by

$$IC_{yy} = -2\Re[A^*B + C^*Dp_\eta^2 \pm (A^*D + BC^*)p_\eta]. \tag{8.0.1}$$

Such a measurement requires both a polarised beam and a polarised target. The use of these would, however, result in significantly lower luminosities and require a much longer beam time.

Currently, there are efforts being made to describe the cross sections and asymmetries of the $\mathrm{d} + \mathrm{p} \to {}^3\mathrm{He} + \eta$ reaction with a framework that directly involves the $\eta\,{}^3\mathrm{He}$ optical potential [97]. In addition to the unpolarised cross section data, the findings presented here also serve as input for this attempt. The authors claim that with their method they are able to determine the $\eta\,{}^3\mathrm{He}$ scattering length, including its sign. This was not possible in previous analyses and would resolve the ambiguity between a bound and virtual state. Furthermore, this procedure would also allow to determine the properties of such a state, *i.e.* its binding energy and width. Of course, this could have a substantial impact on this field of research.

There are still more hadronic processes which could be studied in the search for η-mesic nuclei. The $\mathrm{p} + {}^3\mathrm{H} \to {}^4\mathrm{He} + \eta$ might have a larger cross section than the $\mathrm{d} + \mathrm{d} \to {}^4\mathrm{He} + \eta$ process since the larger size of the deuterons have fuse into the much smaller ${}^4\mathrm{He}$. This might allow for a more precise extraction of the pole position.

In the $\mathrm{p} + {}^6\mathrm{Li} \to {}^4\mathrm{He} + {}^3\mathrm{He} + \eta$ reaction the $\eta\,{}^3\mathrm{He}$ and $\eta\,{}^4\mathrm{He}$ systems could be studied and compared within the same final state. Away from threshold, two bands should be visible in the Dalitz plot which correspond the $\eta\,{}^3\mathrm{He}$ and $\eta\,{}^4\mathrm{He}$ final state interaction. This way, the relative strength and positions of the poles could be studied with much fewer systematic effects that arise from having two separate measurements. Of course, the limitations of a measurement based on real η production still apply and the sign of the pole's imaginary part cannot be determined. Moreover, detecting and identifying the two different helium isotopes would certainly an experimental challenge.

The $\eta\,{}^3\mathrm{H}$ final state is very similar to the $\eta\,{}^3\mathrm{He}$ system. Since the number of nucleons is the same, it would be reasonable to assume that the strength of the interaction should be the same in both systems. However, isospin violation in the quasi-free $\mathrm{n} + \mathrm{d} \to {}^3\mathrm{H} + \eta$ reaction is likely to affect the position of the pole. This reaction would require a spectator proton to be detected and the experiment would have to have a sufficient resolution to still be sensitive to the isospin violation.

There have been measurements on pion-induced η production with the $\pi^- + {}^3\mathrm{He} \to {}^3\mathrm{H} + \eta$ reaction in the past [98, 99], although these did not go all the way down to the production threshold. More detailed data may reveal a pole in this process as well.

There are more hadronic processes beyond the ones presented here that might help with the further development of phenomenological models. On the other hand, nowadays there are more electromagnetic facilities in the world than hadronic ones. These would likely benefit from continued efforts with hadronic reactions [100].

One more measurement with the COSY-ANKE experiment has been performed on the $\mathrm{p} + \mathrm{n} \to \mathrm{d} + \eta$ reaction with goal to provide total cross sections in the production threshold region and, for the first time, measure the differential cross sections [40]. The extraction of the pole position in this reaction would allow to further study the dependence of the η-nucleus final state interaction on the mass number of the nucleus. It stands to reason that, if the $\eta\,{}^4\mathrm{He}$ system is bound, the $\eta\,\mathrm{d}$ system is likely to be unbound. The results of this measurement will test this hypothesis and may provide further evidence to help with the understanding of η-nucleus quasi-bound states.

Bibliography

[1] H Fritzsch, M Gell-Mann, and H Leutwyler. "Advantages of the color octet gluon picture". English. In: *Physics Letters B* 47.4 (Nov. 1973), pp. 365–368. DOI: `10.1016/0370-2693(73)90625-4`. URL: `http://linkinghub.elsevier.com/retrieve/pii/0370269373906254`.

[2] H D Politzer. "Reliable Perturbative Results for Strong Interactions?" In: *Physical Review Letters* 30 (1973), pp. 1346–1349. DOI: `10.1103/PhysRevLett.30.1346`.

[3] D J Gross and F Wilczek. "Ultraviolet Behavior of Non-Abelian Gauge Theories". English. In: *Physical Review Letters* 30.26 (June 1973), pp. 1343–1346. DOI: `10.1103/PhysRevLett.30.1343`. URL: `http://link.aps.org/doi/10.1103/PhysRevLett.30.1343`.

[4] S Weinberg. "Non-Abelian Gauge Theories of the Strong Interactions". In: *Physical Review Letters* 31.7 (Aug. 1973), p. 494. DOI: `10.1103/PhysRevLett.31.494`. URL: `http://journals.aps.org/prl/abstract/10.1103/PhysRevLett.31.494`.

[5] K A Olive and Particle Data Group. "Review of Particle Physics". English. In: *Chinese Physics C* 38.9 (Aug. 2014), p. 090001. DOI: `10.1088/1674-1137/38/9/090001`. URL: `http://iopscience.iop.org/article/10.1088/1674-1137/38/9/090001`.

[6] R K Ellis, W J Stirling, and B R Webber. *QCD and Collider Physics*. English. Cambridge University Press, Dec. 2003. ISBN: 9780521545891. URL: `http://books.google.se/books?id=TqrPVoS6s0UC&printsec=frontcover&dq=qcd+and+collider+physics&hl=&cd=1&source=gbs_api`.

[7] R S Bhalerao and L C Liu. "Off-Shell Model for Threshold Pionic η Production on a Nucleon and for ηN Scattering". English. In: *Physical Review Letters* 54.9 (1985), pp. 865–868. DOI: `10.1103/PhysRevLett.54.865`. URL: `http://link.aps.org/doi/10.1103/PhysRevLett.54.865`.

[8] Q Haider and L C Liu. "Formation of an eta-mesic nucleus". English. In: *Physics Letters B* 172.2 (May 1986), pp. 257–260. DOI: `10.1016/0370-2693(86)90846-4`. URL: `http://linkinghub.elsevier.com/retrieve/pii/0370269386908464`.

[9] T Mersmann et al. "Precision Study of the η^3He System Using the $dp \to {}^3$Heη Reaction". Englisch. In: *Physical Review Letters* 98.24 (June 2007), p. 242301. DOI: `10.1103/PhysRevLett.98.242301`. URL: `http://link.aps.org/doi/10.1103/PhysRevLett.98.242301`.

[10] Murray Gell-Mann. “A Schematic Model of Baryons and Mesons”. English. In: *Physics Letters* 8.3 (1964), pp. 214–215. DOI: `10.1016/S0031-9163(64)92001-3`. URL: `http://linkinghub.elsevier.com/retrieve/pii/S0031916364920013`.

[11] Z G Wang. “Tetraquark state candidates: $Y(4260)$, $Y(4360)$, $Y(4660)$ and $Z_c(4020/4025)$”. In: *arXiv.org* (2016). scholar: `92B46409-B067-4E9C-950C-B455826214FD`. URL: `http://arxiv.org/abs/1601.05541`.

[12] R Aaij et al. “Observation of J/ψp Resonances Consistent with Pentaquark States in $\Lambda_b^0 \to$ J/ψK$^-$p Decays”. English. In: *Physical Review Letters* 115.7 (July 2015), p. 072001. DOI: `10.1103/PhysRevLett.115.072001`. URL: `http://link.aps.org/doi/10.1103/PhysRevLett.115.072001`.

[13] P Adlarson et al. “Abashian-Booth-Crowe Effect in Basic Double-Pionic Fusion: A New Resonance?” English. In: *Physical Review Letters* 106.24 (June 2011), p. 242302. DOI: `10.1103/PhysRevLett.106.242302`. URL: `http://link.aps.org/doi/10.1103/PhysRevLett.106.242302`.

[14] H Fei et al. “Is d* a candidate for a hexaquark-dominated exotic state?” English. In: *Chinese Physics C* 39.7 (July 2015), p. 071001. DOI: `10.1088/1674-1137/39/7/071001`. URL: `http://iopscience.iop.org/article/10.1088/1674-1137/39/7/071001`.

[15] K S Krane. *Introductory Nuclear Physics*. English. John Wiley & Sons, Jan. 2008. ISBN: 9788126517855. URL: `http://books.google.se/books?id=mkZjC1TLXh8C&dq=inauthor:krane+intitle:introductory+nuclear+physics&hl=&cd=1&source=gbs_api`.

[16] H Machner. “Search for quasi bound η mesons”. English. In: *Journal of Physics G: Nuclear and Particle Physics* 42.4 (Apr. 2015), p. 043001. DOI: `10.1088/0954-3899/42/4/043001`. URL: `http://iopscience.iop.org/article/10.1088/0954-3899/42/4/043001`.

[17] Q Haider and L C Liu. “Dependence of calculated binding energies and widths of η-mesic nuclei on treatment of subthreshold η-nucleon interaction”. English. In: *Physical Review C* 66.4 (Oct. 2002), p. 045208. DOI: `10.1103/PhysRevC.66.045208`. URL: `http://link.aps.org/doi/10.1103/PhysRevC.66.045208`.

[18] H A Bethe. “Theory of the Effective Range in Nuclear Scattering”. English. In: *Physical Review* 76.1 (1949), pp. 38–50. DOI: `10.1103/PhysRev.76.38`. URL: `http://link.aps.org/doi/10.1103/PhysRev.76.38`.

[19] J Berger et al. “Identification of the $d+p \to {}^3$He$+\eta$ Reaction Very Near Threshold: Cross-section and Deuteron Tensor Analyzing Power”. English. In: *Physical Review Letters* 61.8 (1988), pp. 919–922. DOI: `10.1103/PhysRevLett.61.919`. URL: `http://link.aps.org/doi/10.1103/PhysRevLett.61.919`.

[20] B Mayer et al. “Reactions $pd \to {}^3$He η and $pd \to {}^3$He$\pi^+\pi^-$ near the η threshold”. English. In: *Physical Review C* 53.5 (May 1996), pp. 2068–2074. DOI: `10.1103/PhysRevC.53.2068`. URL: `http://link.aps.org/doi/10.1103/PhysRevC.53.2068`.

[21] B Krusche and C Wilkin. “Production of η and η'mesons on nucleons and nuclei ”. English. In: *Progress in Particle and Nuclear Physics* 80 (Jan. 2015), pp. 43–95. DOI: `10.1016/j.ppnp.2014.10.001`. URL: `http://linkinghub.elsevier.com/retrieve/pii/S0146641014000702`.

[22] J Smyrski et al. “Measurement of the $dp \to {}^3\mathrm{He}\eta$ reaction near threshold”. English. In: *Physics Letters B* 649.4 (June 2007), pp. 258–262. DOI: `10.1016/j.physletb.2007.04.021`. URL: `http://linkinghub.elsevier.com/retrieve/pii/S0370269307004790`.

[23] C Wilkin et al. “Is there an ηHe3 quasi-bound state?” Englisch. In: *Physics Letters B* 654.3-4 (Oct. 2007), pp. 92–96. DOI: `10.1016/j.physletb.2007.08.041`. URL: `http://linkinghub.elsevier.com/retrieve/pii/S0370269307010180`.

[24] J F Germond and C Wilkin. “The dp$\to$ ${}^3\mathrm{He}\pi^0$ reaction at threshold”. In: *Journal of Physics G: Nuclear Physics* 14.2 (Feb. 1988), pp. 181–190. DOI: `10.1088/0305-4616/14/2/010`. URL: `http://stacks.iop.org/0305-4616/14/i=2/a=010?key=crossref.c139c849fa61ad705ed4e7ebcf74b8dc`.

[25] C Kerboul et al. “Deuteron Tensor Analyzing Power for the Collinear $\vec{dp} \to {}^3\mathrm{He}\pi^0$ Reaction at Intermediate-energies”. English. In: *Physics Letters* B181.1-2 (1986), pp. 28–32. DOI: `10.1016/0370-2693(86)91248-7`. URL: `http://linkinghub.elsevier.com/retrieve/pii/0370269386912487`.

[26] D Drechsel and L Tiator. “Threshold pion photoproduction on nucleons”. English. In: *J. Phys.* G18.3 (1992), pp. 449–497. DOI: `10.1088/0954-3899/18/3/004`. URL: `http://iopscience.iop.org/article/10.1088/0954-3899/18/3/004`.

[27] M Pfeiffer et al. “Photoproduction of η-Mesic ^{3}He”. English. In: *Physical Review Letters* 92.25 (June 2004), p. 252001. DOI: `10.1103/PhysRevLett.92.252001`. URL: `http://link.aps.org/doi/10.1103/PhysRevLett.92.252001`.

[28] F Pheron et al. “Coherent photoproduction of η-mesons off ^{3}He – search for η-mesic nuclei”. English. In: *Physics Letters B* 709.1-2 (Mar. 2012), pp. 21–27. DOI: `10.1016/j.physletb.2012.01.075`. URL: `http://linkinghub.elsevier.com/retrieve/pii/S0370269312001165`.

[29] R Frascaria et al. “Total $d + d \to \alpha + \eta$ cross-sections near threshold”. In: *Physical Review C* 50.2 (1994), pp. 537–540. DOI: `10.1103/PhysRevC.50.R537`. URL: `http://journals.aps.org/prc/abstract/10.1103/PhysRevC.50.R537`.

[30] N Willis. “η-helium quasi-bound states”. In: *Physics Letters B* 406.1-2 (July 1997), pp. 14–19. DOI: `10.1016/S0370-2693(97)00650-3`. URL: `http://www.sciencedirect.com/science/article/pii/S0370269397006503`.

[31] A Wronska et al. “Near threshold eta meson production in the $dd \to {}^4\mathrm{He}\alpha$ reaction”. In: *The European Physical Journal A* 26.3 (Dec. 2005), pp. 421–428. URL: `http://cds.cern.ch/record/898402`.

[32] A Budzanowski et al. “Cross section and tensor analysing power of the $dd \to \eta\alpha$ reaction near threshold”. English. In: *Nuclear Physics A* 821.1-4 (Apr. 2009), pp. 193–209. DOI: `10.1016/j.nuclphysa.2009.02.004`. URL: `http://linkinghub.elsevier.com/retrieve/pii/S0375947409001122`.

[33] E Friedman, A Gal, and J Mareš. “η-nuclear bound states revisited”. English. In: *Physics Letters B* 725.4-5 (Oct. 2013), pp. 334–338. DOI: `10.1016/j.physletb.2013.07.035`. URL: `http://arxiv.org/abs/1304.6558`.

[34] M Skurzok et al. “Upper Limits for the Production of the η-mesic Helium in the $dd \to {}^3\mathrm{He}n\pi^0$ and $dd \to {}^3\mathrm{He}p\pi^-$ Reactions”. English. In: *Physical Review* B47.2 (2016), pp. 503–508. DOI: `10.5506/APhysPolB.47.503`. URL: `http://cds.cern.ch/record/2127264`.

[35] F Hibou et al. “Near-threshold η production in the $pd \to pd\eta$ reaction”. In: *The European Physical Journal A* 7.4 (Apr. 2000), pp. 537–541. URL: `http://cds.cern.ch/record/424314`.

[36] R Bilger et al. “Measurement of the $pd \to pd\eta$ cross-section in complete kinematics”. In: *Physical Review C* 69.1 (2004), p. 014003. DOI: `10.1103/PhysRevC.69.014003`. URL: `http://journals.aps.org/prc/abstract/10.1103/PhysRevC.69.014003`.

[37] H Calén et al. “Measurement of the Quasifree $p + n \to d + \eta$ Reaction near Threshold”. English. In: *Physical Review Letters* 79.14 (Oct. 1997), pp. 2642–2645. DOI: `10.1103/PhysRevLett.79.2642`. URL: `http://link.aps.org/doi/10.1103/PhysRevLett.79.2642`.

[38] H Calén et al. “Threshold Structure of the Quasifree $p + d \to d + \eta$ Reaction”. English. In: *Physical Review Letters* 80.10 (Mar. 1998), pp. 2069–2072. DOI: `10.1103/PhysRevLett.80.2069`. URL: `http://link.aps.org/doi/10.1103/PhysRevLett.80.2069`.

[39] N V Shevchenko et al. “Faddeev-type calculation of ηd threshold scattering”. English. In: *Physical Review C* 58.6 (Dec. 1998), R3055–R3059. DOI: `10.1103/PhysRevC.58.R3055`. URL: `http://link.aps.org/doi/10.1103/PhysRevC.58.R3055`.

[40] D Schröer. *Strahlzeitvorbereitungen zur Untersuchung der schwellennahen Produktion von η-Mesonen in der quasifreien Reaktion $pd \to d\eta p_{spec}$ bei ANKE.* Diploma Thesis, Aug. 2012.

[41] Y Maghrbi et al. “Coherent photoproduction of π^0- and η-mesons off ${}^7\mathrm{Li}$”. English. In: *The European Physical Journal A - Hadrons and Nuclei* 49.3 (2013), pp. 1–14. DOI: `10.1140/epja/i2013-13038-3`. URL: `http://link.springer.com/10.1140/epja/i2013-13038-3`.

[42] E Scomparin. PhD thesis. 1993.

[43] A Budzanowski et al. “Experimental study of the $p + {}^6\mathrm{Li} \to \eta + {}^7\mathrm{Be}$ reaction 11.3 MeV above threshold”. English. In: *Physical Review C* 82.4 (Oct. 2010), p. 041001. DOI: `10.1103/PhysRevC.82.041001`. URL: `http://link.aps.org/doi/10.1103/PhysRevC.82.041001`.

[44] G A Sokol et al. “Discovery of η mesic nuclei”. In: *Physics of Particles and Nuclei Letters* 102 (2000), pp. 71–95.

[45] A Budzanowski et al. “Search for η-mesic nuclei in a recoil-free transfer reaction”. English. In: *Physical Review C* 79.1 (Jan. 2009), p. 012201. DOI: `10.1103/PhysRevC.79.012201`. URL: `http://link.aps.org/doi/10.1103/PhysRevC.79.012201`.

[46] Gerald G Ohlsen. “Polarization transfer and spin correlation experiments in nuclear physics”. English. In: *Reports on Progress in Physics* 35.2 (May 1972), pp. 717–801. DOI: `10.1088/0034-4885/35/2/305`. URL: `http://stacks.iop.org/0034-4885/35/i=2/a=305?key=crossref.86cfa156ba29993f8b916c10dae29798`.

[47] A Khoukaz et al. “Investigation of the $^3\mathrm{He}\eta$ final state in the $\vec{d}p \to {}^3\mathrm{He}\eta$ reaction at ANKE”. In: *COSY Proposal and Beam Time Request* (Apr. 2006). URL: `http://collaborations.fz-juelich.de/ikp/anke/proposal/New_proposal_eta.ps`.

[48] R Maier. “Cooler synchrotron COSY—Performance and perspectives”. In: *Nuclear Instruments and Methods in Physics Research A* 390.1-2 (May 1997), pp. 1–8. DOI: `10.1016/S0168-9002(97)00324-0`. URL: `http://www.sciencedirect.com/science/article/pii/S0168900297003240`.

[49] P Goslawski. “High precision measurement of the η meson mass at COSY - ANKE”. PhD thesis. Apr. 2013.

[50] P Goslawski et al. “High precision beam momentum determination in a synchrotron using a spin-resonance method”. English. In: *Physical Review Special Topics-Accelerators and Beams* 13.2 (Feb. 2010), p. 022803. DOI: `10.1103/PhysRevSTAB.13.022803`. URL: `http://link.aps.org/doi/10.1103/PhysRevSTAB.13.022803`.

[51] P Goslawski. *Hochpräzise Impulsbestimmung des COSY-Beschleunigerstrahls im Rahmen der Messung zur Bestimmung der η-Masse am Experimentaufbau ANKE.* Diploma Thesis, Dec. 2008.

[52] D Chiladze. “Polarised Charge-Exchange Reaction $dp \to (pp)n$ Studies at the ANKE-COSY Spectrometer”. PhD thesis. Dec. 2008.

[53] R Weidmann et al. “The polarized ion source for COSY”. In: *Review of Scientific Instruments* 67 (1996), pp. 1357–1358. DOI: `10.1063/1.1146665`. URL: `http://scitation.aip.org/content/aip/journal/rsi/67/3/10.1063/1.1146665`.

[54] W Haeberli. “Sources of Polarized Ions”. English. In: *Annual Review of Nuclear Science* 17.1 (1967), pp. 373–426. DOI: `10.1146/annurev.ns.17.120167.002105`. URL: `http://dx.doi.org/10.1146/annurev.ns.17.120167.002105`.

[55] S Barsov et al. “ANKE, a new facility for medium energy hadron physics at COSY-Juelich”. English. In: *Nuclear Instruments and Methods in Physics Research Section A: Accelerators, Spectrometers, Detectors and Associated Equipment* A462.3 (2001), pp. 364–381. DOI: `10.1016/S0168-9002(00)01147-5`. URL: `http://linkinghub.elsevier.com/retrieve/pii/S0168900200011475`.

[56] H Dombrowski et al. “The Münster cluster target for internal storage ring experiments”. English. In: *Nuclear Instruments and Methods in Physics Research Section A: Accelerators, Spectrometers, Detectors and Associated Equipment* 386.2–3 (1997), pp. 228–234. DOI: `10.1016/S0168-9002(96)01177-1`. URL: `http://www.sciencedirect.com/science/article/pii/S0168900296011771`.

[57] A Khoukaz et al. “Systematic studies on hydrogen cluster beam production”. English. In: *The European Physical Journal D - Atomic, Molecular, Optical and Plasma Physics* 5.2 (1999), pp. 275–281. DOI: `10.1007/PL00021595`. URL: `http://link.springer.com/10.1007/PL00021595`.

[58] N Lang. *Pionenproduktion am Magnetspektrometer ANKE mit dem Wasserstoff-Clustertarget.* Diploma Thesis, 2000.

[59] C Quentmeier. “Untersuchungen der Reaktion p+p $\rightarrow$ppK$^+$K$^-$ nahe der Produktionsschwelle”. PhD thesis. Dissertation, 2001.

[60] O Hagena and W Obert. “Cluster Formation in Expanding Supersonic Jets: Effect of Pressure, Temperature, Nozzle Size, and Test Gas”. In: *The Journal of Chemical Physics* 56.5 (1972), p. 1793. URL: `http://link.aip.org/link/?JCPSA6/56/1793/1`.

[61] E Köhler. “Mass spectroscopy of hydrogen cluster-jets and beam density optimisation studies”. PhD thesis. 2015.

[62] A Täschner et al. “High density cluster jet target for storage ring experiments”. English. In: *Nuclear Instruments and Methods in Physics Research Section A: Accelerators, Spectrometers, Detectors and Associated Equipment* 660.1 (Dec. 2011), pp. 22–30. DOI: `10.1016/j.nima.2011.09.024`. URL: `http://www.sciencedirect.com/science/article/pii/S0168900211017761`.

[63] A-K Hergemöller. *Präparation von Clusterstrahlen und der Aufbau der finalen Clusterquelle für das PANDA-Experiment.* Master Thesis, Mar. 2013.

[64] M Mielke. “Multi-Pion Production in Deuteron-Proton Collisions at COSY-ANKE”. PhD thesis. 2014. URL: `https://mail.google.com/mail/u/0/`.

[65] T Mersmann. “Untersuchung der Wechselwirkung zwischen η-Mesonen und ^{3}He-Kernen am Experimentaufbau ANKE”. PhD thesis. 2007.

[66] D Chiladze et al. “Determination of deuteron beam polarizations at COSY”. English. In: *Physical Review Special Topics-Accelerators and Beams* 9.5 (May 2006), p. 050101. DOI: `10.1103/PhysRevSTAB.9.050101`. URL: `http://link.aps.org/doi/10.1103/PhysRevSTAB.9.050101`.

[67] Rene Brun and Fons Rademakers. “ROOT — An object oriented data analysis framework”. In: *Nuclear Instruments and Methods in Physics Research Section A: Accelerators, Spectrometers, Detectors and Associated Equipment* 389.1–2 (Apr. 1997), pp. 81–86. DOI: `10.1016/S0168-9002(97)00048-X`. URL: `http://www.sciencedirect.com/science/article/pii/S016890029700048X`.

[68] B Stroustrup. *The C++ programming language; 4th ed.* Reading, MA: Addison-Wesley, 2013. ISBN: 0321563840. URL: `http://cds.cern.ch/record/1530507`.

[69] V Hejny, M Hartmann, and A Mussgiller. “RootSorter: A New Analysis Framework for ANKE”. In: *ANKE Annual Report* (2003).

[70] S Dymov. “Private Communication”. 2007.

[71] S N Dymov et al. "Constrained minimization in the C++ environment". English. In: *Nuclear Instruments and Methods in Physics Research Section A: Accelerators, Spectrometers, Detectors and Associated Equipment* 440.2 (2000), pp. 431–437. DOI: 10.1016/S0168-9002(99)00758-5. URL: http://www.sciencedirect.com/science/article/pii/S0168900299007585.

[72] I Froehlich et al. "Pluto: A Monte Carlo Simulation Tool for Hadronic Physics". In: *arXiv.org* (Aug. 2007). arXiv: 0708.2382v2 [nucl-ex]. URL: http://arxiv.org/abs/0708.2382v2.

[73] M G Pia. "The GEANT4 Object Oriented Simulation Tookit". In: INFN-AE-99-22 (1999). URL: http://cds.cern.ch/record/423672.

[74] A Mussgiller. "A New Geant4 based Simulation Framework for ANKE". In: *ANKE Annual Report* (2004). URL: http://collaborations.fz-juelich.de/ikp/anke/annual/annual_reports/04/IKP2_AR_mussgill_Anke_Simulation_V0.pdf.

[75] M Ghumalia and P Ghumalia. *C/C++ Software Development With Eclipse: The easisest guide on using Eclipse for C/C++ Software Development.* English. CreateSpace Independent Publishing Platform, 2011. ISBN: 9781453662113. URL: https://books.google.se/books?id=p4aTHarK8bQC.

[76] B O'Sullivan. *Mercurial: The Definitive Guide.* English. O'Reilly Media, 2009. ISBN: 9780596555474. URL: https://books.google.se/books?id=upW0sR6BC_wC.

[77] F P Miller, A F Vandome, and M B John. *Mantis Bug Tracker.* English. VDM Publishing, 2010. ISBN: 9786131809811. URL: https://books.google.se/books?id=5iZcXwAACAAJ.

[78] K Martin and B Hoffman. *Mastering CMake: a cross-platform build system : version 3.1.* New York, NY: Kitware, 2015. URL: http://cds.cern.ch/record/2027837.

[79] Google. *Google C++ Style Guide.* URL: https://google.github.io/styleguide/cppguide.html.

[80] I Burmeister. *Luminositätsbetrachtung und Analyse des $^3He\eta$-Reaktionskanals in dp-Kollisionen am ANKE-Magnetspektrometer.* Diploma Thesis, Feb. 2011. URL: http://www.uni-muenster.de/imperia/md/content/physik_kp/agkhoukaz/bamadipdok/dipl_ib.pdf.

[81] C Fritzsch. *Untersuchung verschiedener Normierungsreaktionen für dp-Kollisionen am ANKE-Experiment.* Master Thesis, May 2014. URL: http://www.uni-muenster.de/imperia/md/content/physik_kp/agkhoukaz/bamadipdok/ma_cf.pdf.

[82] C Fritzsch. *Energiekalibrierung für das ANKE-Experiment.* Bachelor Thesis, Aug. 2011. URL: http://www.uni-muenster.de/imperia/md/content/physik_kp/agkhoukaz/bamadipdok/ba_cf.pdf.

[83] M Evelt. *Identifikation des $^3He\pi^0$-Endzustandes in Deuteron-Proton-Kollisionen am ANKE-Experiment.* Bachelor Thesis, July 2012. URL: http://www.uni-muenster.de/imperia/md/content/physik_kp/agkhoukaz/bamadipdok/ba_me.pdf.

[84] D Guderian. *Simulationen zur Mehrpionenproduktion in der quasifreien Reaktion $pd \rightarrow d\pi^+\pi^- p_{spec}$ an ANKE*. Bachelor Thesis, Apr. 2015. URL: `http://www.uni-muenster.de/imperia/md/content/physik_kp/agkhoukaz/bamadipdok/ba_dg.pdf`.

[85] D Mchedlishvili et al. “The neutron-proton charge-exchange amplitudes measured in the dp → ppn reaction”. English. In: *The European Physical Journal A* 49.4 (2013), pp. 1–13. DOI: `10.1140/epja/i2013-13049-0`. URL: `http://link.springer.com/10.1140/epja/i2013-13049-0`.

[86] D V Bugg and C Wilkin. “Polarisation in the (d, 2p) reaction at intermediate energies”. English. In: *Nuclear Physics A* 467.4 (June 1987), pp. 575–620. DOI: `10.1016/0375-9474(87)90387-3`. URL: `http://linkinghub.elsevier.com/retrieve/pii/0375947487903873`.

[87] C Wilkin. “Private Communication”. June 2013.

[88] M Eggert. “Entwicklung eines gepulsten Caesium-Ionenstrahls fuer die Quelle polarisierter Ionen an COSY/Juelich”. PhD thesis. 1999.

[89] D Chiladze et al. “The dp → ppn reaction as a method to study neutron-proton charge-exchange amplitudes”. English. In: *The European Physical Journal A - Hadrons and Nuclei* 40.1 (Mar. 2009), pp. 23–33. DOI: `10.1140/epja/i2008-10731-2`. URL: `http://www.springerlink.com/index/10.1140/epja/i2008-10731-2`.

[90] S Dymov. “Private Communication”. 2012.

[91] D Mchedlishvili. “Studies of the neutron-proton charge-exchangeamplitudes at COSY using the ANKE spectrometer”. PhD thesis. Sept. 2013. URL: `http://collaborations.fz-juelich.de/ikp/anke/theses/DM-thesis_13.09.2013.pdf`.

[92] D Mchedlishvili and D Chiladze. “Recent results from the deuteron charge-exchange on hydrogen programme at ANKE/COSY”. English. In: *J. Phys. Conf. Ser.* 295.1 (2011), p. 012099. DOI: `10.1088/1742-6596/295/1/012099`. URL: `http://iopscience.iop.org/article/10.1088/1742-6596/295/1/012099`.

[93] M Papenbrock et al. “Absence of spin dependence in the final state interaction of the reaction”. English. In: *Physics Letters B* 734 (June 2014), pp. 333–337. DOI: `10.1016/j.physletb.2014.05.079`. URL: `http://www.sciencedirect.com/science/article/pii/S037026931400389X`.

[94] Yu N Uzikov. “Spin observables of the $pd \rightarrow {}^3\mathrm{He}\eta$ reaction and quasi-bound ${}^3\mathrm{He}-\eta$ pole”. English. In: *Nuclear Physics A* 801.3–4 (2008), pp. 114–128. DOI: `10.1016/j.nuclphysa.2007.12.010`. URL: `http://www.sciencedirect.com/science/article/pii/S037594740800002X`.

[95] C Fritzsch. “PhD Thesis in preparation”. PhD thesis.

[96] N Hüsken. “PhD Thesis in preparation”. PhD thesis.

[97] Ju-Jun Xie et al. “Determination of the η^3He threshold structure from the low energy $pd \rightarrow \eta^3$He reaction”. In: *Physical Review* nucl-th (2016). URL: `http://arxiv.org/abs/1609.03399`.

[98] J Peng et al. “Coherent η-meson production in the reaction $\pi^-+^3\text{He}\to \eta+\text{t}$”. English. In: *Physical Review Letters* 63.21 (Nov. 1989), pp. 2353–2356. DOI: `10.1103/PhysRevLett.63.2353`. URL: `http://link.aps.org/doi/10.1103/PhysRevLett.63.2353`.

[99] J C Peng et al. “Observation of η-Meson Production in the Reaction $\pi^- + {}^3\text{He}\to \eta + t$”. English. In: *Physical Review Letters* 58.20 (May 1987), pp. 2027–2030. DOI: `10.1103/PhysRevLett.58.2027`. URL: `http://link.aps.org/doi/10.1103/PhysRevLett.58.2027`.

[100] W J Briscoe et al. “Physics opportunities with meson beams”. English. In: *The European Physical Journal A - Hadrons and Nuclei* 51.10 (Oct. 2015), pp. 1–28. DOI: `10.1140/epja/i2015-15129-5`. URL: `http://link.springer.com/10.1140/epja/i2015-15129-5`.

Acknowledgements

A work of science is rarely the work of any one person. I would like to take this opportunity to humbly extend my gratitude and appreciation to the people who contributed to this work in a variety of different ways.

First of all, I want to thank Prof. Dr. Alfons Khoukaz for giving me the opportunity to work on this thesis in his group and creating the familiar atmosphere that allowed many students to emerge as scientists. The freedom to pursue creative projects and acknowledging their importance as well as the fruitful discussions have no doubt had a substantial and long lasting impact on my future.

I am grateful to Prof. Dr. Johannes P. Wessels for taking on the role as my second supervisor and to PD Dr. Jochen Heitger for agreeing to be the third examiner.

A heartfelt "Thank you!" goes to Prof. Dr. Colin Wilkin, who helped push this analysis across the finish line. During your time in Münster you taught me how theory and experiment come together to move our research forward. Your help and insight was invaluable in completing this daunting task.

Many members of the ANKE collaboration have contributed to this work in a variety of ways, be it through participating in the beam time, iterating on the publication, or helping with the analysis and tools. My gratitude goes out to all of them. In particular, I want to mention Prof. Dr. Hans Ströher for his support, Dr. Andro Kacharava for leading the way, and Dr. Sergey Dymov for the FdModule and the help with the calibration.

The COSY crew a lot of credit for making the most out of this measurement in the face of substantial technical difficulties. The results of this thesis were only possible with their hard work. A special mention goes Dr. Ralf Gebel who was always just around the corner when COSY or the polarised source needed some extra motivation.

I want to make a very special mention of my development team on our software project, Malte Mielke and Paul Goslawski. The *Reconstruction* was the beating heart of this work and you both contributed a big piece to it. You helped me realise a vision that was never a guaranteed success. I honestly believe that, together, we changed things for the better. Thank you! A lot!

Malte, of all the people I met during my studies, you and I shared the same path the longest. This partnership left me with a lot of good memories and made my life richer. Thank you for that and thank you for your friendship!

Paul, your incredible enthusiasm has been very contagious and always gave our efforts purpose. Thank you for all your support and great times in- and outside of work! !!!

I would also like to thank Timo Mersmann who never quite stopped being a supervisor to me. Thank you for your help with the thesis, your guidance, and your friendship.

A very special mention goes out to Michael Evelt, who served probably as the first real guinea pig for our software, for all the help related to the thesis, for all the Injustice

sessions, and for being the best Nightwing a Batman could wish for.

My gratitude also goes to the many members of the workgroup, Kay for the late night discussions, Florian for taking over the administrator responsibilities from me and the Warhammer sessions, Silke and Ann-Katrin for making the final year a lot of fun, Ingo, Natalie, Jennyfer, Winne, Christopher, Nils, Daniel, and and and. Thank you to everyone who at some point was a part of this little family.

I also want to thank my new department for their support and for making me feel right at home. Thank you to Tord and Karin for this new opportunity and for expanding my horizon. A great thank you goes to all the colleagues, Walter, Bo, Magnus, Andrzej, Cui, Lena, Li, Aila, and everyone else I forgot to mention here for all the discussions and especially all the fun.

With a little bit of a twist, I thank Scott Snyder and Greg Capullo as well as the rest of the team for an exceptional run on Batman. Whenever I thought times were tough, you were just putting Bruce through something worse. He often served as an inspiration for what it means to always push forward. And this was probably captured best towards the end of Zero Year: “I’ll never quit.”

I am incredibly grateful to my wonderful girlfriend Karin and to Ivar. Any words I could write here would pale in comparison to what your love and support mean to me.

Zum Abschluss danke ich meiner Familie, die mich nicht nur durch diese Zeit begleitet und mich immer unterstützt hat. Danke an meinen Vater Wilhelm, meinen Bruder Markus, meine Schwester Claudia, sowie meinen Neffen Julius und Johann. Und ein ganz besonderer Dank geht an meine Mutter Maria, die das Ende dieser Arbeit leider nicht mehr miterlebt hat.